The Dissertation Committee for Huijie Xu

certifies that this is the approved version of the following dissertation:

# Predictive Modeling of Piston Assembly Lubrication in Reciprocating Internal Combustion Engines

Committee:

Michael D. Bryant, Supervisor

Ronald D. Matthews, Supervisor

Thomas M. Kiehne

Oscar Gonzalez

H. Grady Rylander, Jr

# Predictive Modeling of Piston Assembly Lubrication in Reciprocating Internal Combustion Engines

by

**Huijie Xu, B.Eng; M.Sc**

**Dissertation**

Presented to the Faculty of the Graduate School of

The University of Texas at Austin

in Partial Fulfillment

of the Requirements

for the Degree of

**Doctor of Philosophy**

**The University of Texas at Austin**

December 2005

To My Family

# Acknowledgments

I would like to express my deep gratitude to Professor Michael D. Bryant, my dissertation supervisor, for his advice, support and encouragement during the entire period of my graduate study in the Department of Mechanical Engineering at the University of Texas. Also, my appreciation goes to Professor Ronald D. Matthews, my dissertation co-supervisor, his constructive suggestion and project leadership has enabled me to reach this point.

Also, I would like to thank Dr. Thomas M. Kiehne, our project manager, for spending his time weekly with the team and offered his opinions. Furthermore, I would like to thank Professor Oscar Gonzalez, his excellent courses on Computational Modeling and Numerical Treatment of Partial Differential Equations are very helpful in the study. Meanwhile, Professor Emeritus H.Grady Rylander, Jr's willingness to serve as my committee is greatly appreciated.

Special thanks go to Dr. Dimitris Dardalis and Myoungjin Kim for their helpful discussions and cooperations. The friendship from my officemate - Ji-Hoon Choi, Daejong Kim, Sanghoon Lee, and Rolando Quintanilla makes my graduate study more enjoyable and memorable.

Additionally, the financial support from the U.S. Department of Energy under grant DE-FG26-01NT41337 and the Texas Advanced Technologies Program is highly acknowledged. Without those support, my dissertation work is impossible to be accomplished.

Finally, I would like to thank my wife Huihui Wang for her endless love and various support during the entire course of my graduate study. The continuous moral support from my family is highly cherished.

Huijie Xu

*The University of Texas at Austin*
*December 2005*

**Predictive Modeling of Piston Assembly Lubrication in Reciprocating Internal Combustion Engines**

Publication No. ____________________

Huijie Xu, Ph.D.
The University of Texas at Austin, 2005

Supervisors: Michael D. Bryant and Ronald D. Matthews

The influence of piston assembly lubrication on the reciprocating internal combustion engine performance has received considerable attention for over half-century. An in-depth understanding of piston assembly friction and cylinder wear is crucial for achieving a better fuel economy and higher durability engine design. Early studies show hydrodynamic lubrication theory is applicable to the interface of piston assembly and cylinder liner throughout most of the piston middle stroke. However, when the piston motion ceases near top dead center (TDC) or bottom dead center (BDC) of the stroke, the piston velocity is not adequate to establish a hydrodynamic lubrication action. Lubricating films become very thin and contact

between the surface asperities on the ring and the liner will support part of the piston ring restoring force. Therefore, wear on the cylinder liner surface may occur in the vicinity of TDC and BDC. Severe surface wear could affect the liner-ring sealing performance and result in excessive gas blow-by and fuel consumption.

The objective of this dissertation is to develop a complete mathematical and computational model to predict the piston assembly friction loss in terms of the piston assembly design parameters and cylinder liner surface topography. Piston assembly experiences all three lubrication regimes including hydrodynamic, mixed and boundary lubrication. In order to simplify modeling, early studies usually considered either a full film hydrodynamic lubrication described by Reynolds equation, or a mixed film lubrication described by average Reynolds equation. While our model is based on the real surface interactive between piston assembly and cylinder liner, the latest tribology theory and effective numerical approach have been applied to model piston assembly friction problem. An integrated friction model over three lubrication regimes was developed based on both quasi-static and dynamic equilibrium conditions of the piston assembly. The new model was verified by experimental data with specified pressure and velocity boundaries. Finally, the friction characteristics of a rotating liner engine (RLE) design was investigated as an extension of the conventional piston assembly friction model.

# Contents

# List of Tables

# List of Figures

# Chapter 1

# Introduction

## 1.1 Overview

Tribological interactions between the piston assembly and the liner surface exert a significant influence on the mechanical friction losses of internal combustion engines. Typically, 5 % of total engine fuel energy is dissipated through the piston assembly friction loss, mainly due to piston skirt and piston ring pack loss [1] [2]. Hydrodynamic action dominates engine mid-stroke. Here sufficient lubricant film separates piston rings from cylinder liner. In the vicinity of dead centers, satisfactory lubricant behavior will depend upon both squeeze film and boundary lubrication actions.

It is necessary to quantitatively assess the piston assembly friction in order to optimize the piston ring pack and the piston skirt geometries. Improving fuel economy and promoting environmental protection have become a priority for engine designers. This could be achieved by reducing engine mechanical loss, such as piston assembly friction. The breakdown of friction losses measured in a gasoline engine is shown in Figures 1.1 and 1.2. The piston assembly accounts for 20 - 30 % of mechanical loss for a typical gasoline engine [3].

Interaction between piston assembly and cylinder liner is the most compli-

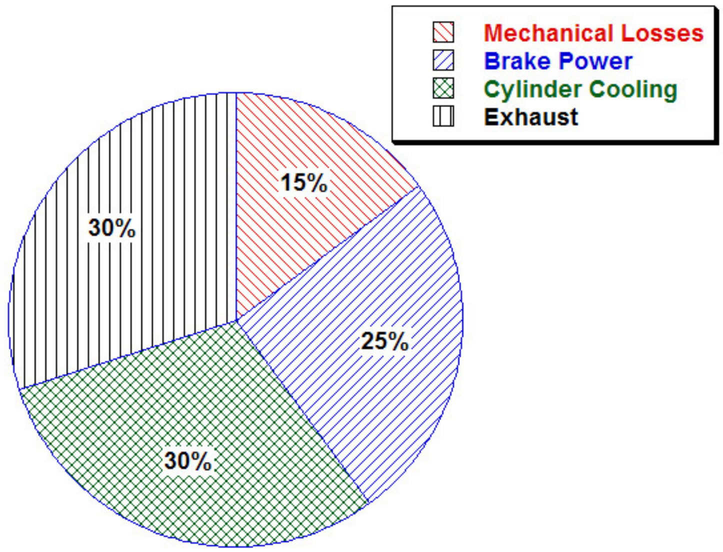


Figure 1.1: Typical dissipation of the fuel energy in an internal combustion engine

cated tribological behavior in reciprocating internal combustion engines [4]. Piston assembly is subjected to large, rapid cyclic variations of pressure, speed and temperature. Both experimental and theoretical studies of piston assembly lubrication have demonstrated that piston-ring pack operates in the hydrodynamic lubrication regime during middle of the stroke where the piston travels most quickly. Here the friction loss between piston assembly and cylinder liner is due entirely to viscous shear in the lubricant. Along portions of the stroke where the piston velocity slows, in the vicinity of TDC or BDC, the lubricant film is much thinner, and surface asperities on the piston assembly and cylinder liner may make contact. These asperity interactions give rise to large friction loss. The piston assembly and cylinder wall contact undergoes multiple lubrication regimes during an engine operating cycle.

Considerable past modeling work assumed that hydrodynamic lubrication of

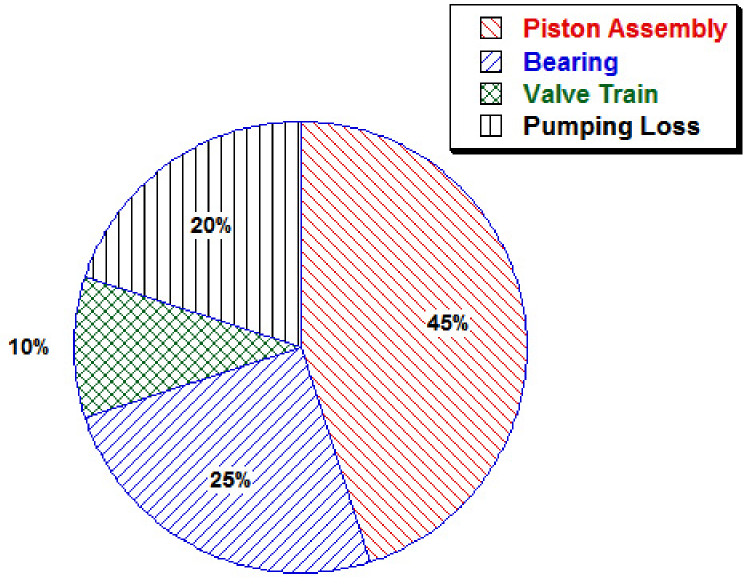


Figure 1.2: Typical distribution of mechanical losses in an internal combustion engine

the piston assembly dominates most of the piston stroke. The relationships between the piston assembly friction loss and the following factors were evaluated through various lubrication models.

- Piston ring and skirt geometries
- Piston ring initial tension load
- Lubricant film starvation effect
- Surface topography of cylinder liner
- Engine load condition - speed, motoring, firing

Most existing models covered only one tribological aspect of piston rings, skirt or cylinder liner. Either hydrodynamic or elasto-hydrodynamic lubrication theory was applied to the piston rings and piston skirt through the entire engine cycle. These approaches are inadequate for real engine operating conditions. Some models did include boundary lubrication in the ring-liner near contact region, however, the approach of adopting a constant friction coefficient, while the effective lubricant film thickness is below the composite surface roughness [5], remains questionable.

Understanding tribological performance of reciprocating internal combustion engines require both piston assembly lubrication and cylinder liner wear be considered together [6]. The interaction between piston rings, skirt lubrication and piston dynamics should be established. The relationship between lubrication action and cylinder wall wear should be addressed in the model.

This dissertation includes a brief survey of past piston assembly lubrication studies, especially the mathematical and computational aspects of modeling. Starting from fundamentals of lubrication theory, a mathematical formulation will be applied to the piston assembly lubrication problem. The focus is to model the piston assembly frictional behavior. Both hydrodynamic and mixed regimes are treated according to surface topography of interactive surfaces, to achieve good accuracy and high numerical efficiency. This model was validated with bench tests before employed to solve the piston assembly friction problem under engine motoring or firing conditions. Finally, the rotating liner engine (RLE) low friction mechanism was explored as the extension of this friction model.

## 1.2 Literature Survey

### 1.2.1 Hydrodynamic Lubrication Models of Piston Assembly

#### Piston Rings

The first hydrodynamic lubrication model of piston ring and cylinder liner was established by Castleman [7] in 1936. In his model, the oil film thickness was predicted to be of the order of 10 $\mu$m. A convex and symmetrical ring face profile was considered.

Eilon at. al [8] observed that hydrodynamic lubrication prevailed throughout most of engine cycle in their experiment. The piston ring friction force increased with piston speed, oil viscosity and chamber gas pressure. They adopted a parabolic ring face profile in the friction model and obtained an analytical solution of the oil film thickness by balancing the forces acting radially on the ring running surface.

Furuhama investigated arch-shaped piston ring lubrication [9]. These rings consist of two circular arcs connected by a flat middle segment. The squeeze film effect was first included in this model. Theoretical predictions of oil film thickness agreed well with the corresponding experimental results at the mid-stroke portion, where hydrodynamic lubrication dominates [10] [11].

By collecting the actual in-service worn piston ring profiles, Lloyd treated the ring running face as an unsymmetrical off-centered parabolic profile and solved a one-dimensional Reynolds equation numerically [12].

A more sophisticated analytical model developed by Ting and Mayer predicted cylinder bore wear pattern, including hydrodynamic lubrication of piston ring and cylinder wall, ring elasticity, blow-by of piston ring pack, and piston side thrust load [13] [14]. An inter-ring gas flow model introduced in this work made study of the piston ring pack lubrication possible.

Hamilton et al. used electric capacitance gauges to measure oil film thickness in a working diesel engine. They observed 0.4 - 2.5 $\mu$m oil film thickness between piston ring and cylinder liner [15] [16] [17], and concluded a well established hydrodynamic lubrication condition. Their theory employing a half-Sommerfeld type boundary condition showed large discrepancy between measured and calculated oil film thickness. Miniature pressure and film thickness transducers, recording hydrodynamic pressure and film thickness simultaneously, showed that piston rings usually operate in the starved lubrication condition over the majority of the stroke. An oil starvation condition in the inlet region of the piston ring was later incorporated in their analytical model. The theoretical film thickness based on the starvation model agreed well with experiment.

Dowson at al. reviewed early modeling work and conducted a comprehensive investigation on piston ring lubrication, to provide design guidelines for optimizing tribological behavior of piston ring and cylinder liner [1] [2] . The Reynolds or Swift-Stieber cavitation boundary condition was first employed to check the divergent area between a piston ring running surface and liner wall. A numerical procedure was developed to predict the film thickness, lubricant transport, and viscous friction for both a single ring and a complete ring pack. They also considered the influence of ring dynamics and ring twist in their lubrication model [18].

After Dowson, hydrodynamic lubrication models focus on either numerical methods such as [19] and [20], or derivation of film thickness functions and boundary conditions such as [5], [21] and [22].

### Piston Skirt

In a reciprocating internal combustion engine, lubricating the piston skirt is less difficult than lubricating the rings. However, undesirable piston dynamics may induce piston slap with audible noise. Early studies showed piston dynamics sensitive to piston-cylinder bore clearance and lubricant viscosity. The lubricant film at the piston-liner interface could serve as a cushion against piston dynamic impact. The relationship between the piston design parameters and the vibration/noise characteristics of engine remains an active research topic.

Li [23] developed a hydrodynamic lubrication model of the piston skirt to predict the entire trajectory of the piston and the friction force under engine working conditions. His analysis implied that piston tilt could influence the piston skirt friction characteristics and showed that piston skirt friction could significantly increase if the piston wrist pin was located in an undesirable position.

### 1.2.2 Elastohydrodynamic Lubrication Models of Piston Assembly

#### Piston Rings

Although hydrodynamic theory has successfully predicted the dynamic behavior of piston rings, and has guided optimization of tribological performance of piston seals, hydrodynamic theory still predicts some unreasonable results, near the dead centers and especially at the beginning of the combustion cycle. For instance, the calculated minimum oil film thickness can be smaller than the surface roughness [2].

Elastohydrodynamic lubrication analysis of piston rings was first conducted by Dowson and his coworker [24]. An important feature is the elastic deformation of the surface bounding the lubricated conjunction, attributed to the hydrodynamic pressure developed in the film of lubricant separating the surfaces. Normally, the face shape of the compression ring is finished with a slightly convex curvature. This assures line contact between the ring and the liner when first installed, allows the ring to assume its normal seating gradually and overcomes any tendency toward top edge bearing and scuffing [25]. Therefore, a classical elastohydrodynamic line contact is analogous to the ring-liner lubrication.

Elastohydrodynamic lubrication theory requires more complicated numerical algorithms and computing time than hydrodynamic lubrication theory. After

Dowson, more effective numerical algorithms were attempted to solve Elastohydrodynamic lubrication models of piston rings , such as Hwu's [26] and Wu's [20] models.

#### Piston Skirt

An elastohydrodynamic lubrication model of the piston skirt developed by Oh [27] investigated the influence of the axial profiles of automotive piston skirt on friction loss using the Newton-Raphson numerical method. Unlike the inverse iteration method, which converges only in case of small surface elastic deformations compared to total film thickness, the Newton-Raphson method converges over a wide range. This model included both thermal and elastic deformation, and concluded that the friction and lubrication characteristics of a piston skirt are sensitive to geometry.

### 1.2.3 Mixed Lubrication Models of Piston Assembly

#### Piston Rings

Inspired by Patir and Cheng's approach to partial contact/rough surface lubrication [28], Rohde introduced a mixed friction model by considering the surface topography on the piston rings and cylinder liners [29]. An average Reynolds equation was used to study the friction performance of dynamically loaded lubrication under different engine operating conditions. Rohde concluded that piston ring friction depended strongly on the surface topography under mixed film lubrication.

A non-axially-symmetric mixed lubrication model was proposed by Hu [30]. Here a nonuniform film thickness distribution was introduced between the ring and the cylinder wall to predict friction and ring lubrication behavior. Surface roughness was incorporated via the average Reynolds equation, and asperity contact pressure was calculated by Greenwood-Tripp's model [31]. Elasticity of ring, static distortion of bore, and variation of gas pressure inside the inter-ring space were integrated into the mixed lubrication model.

Michail's model, based on Ting and Mayer's solution to the piston ring lubrication problem, treated effects of surface roughness via a mathematical representation of a honed surface [32] [33]. The relationship between oil film thickness and surface roughness orientation was examined.

Knopf [34] studied the influence of the liner surface structure on the tribological ring-liner interface. By varying the honing angle, it is possible to find a good compromise between oil transport and hydrodynamic pressure build-up. His model demonstrated that surfaces with asymmetrical amplitude density distribution and transversely oriented topography had a positive impact on hydrodynamic-bearing performance.

#### Piston Skirt

In the early 1990s, Zhu et al. developed a mathematical model for piston skirt friction operating in a mixed lubrication regime. Effects of surface waviness, roughness, piston skirt surface profile were included in an average Reynolds Equation. The entire piston trajectory and viscous friction force were computed under engine running conditions [35].

A comprehensive lubrication model for the piston skirt considered the elastic and thermal distortion of both piston skirt and cylinder bore. Simulations suggested that a parabolic piston skirt profile has advantage over a linear shape, since a parabolic profile can generate hydrodynamic action consistently during either engine-up or engine-down stokes [36] .

### 1.2.4 Wear Models of a Piston Ring-Cylinder Liner System

The principal mechanisms of cylinder liner wear are abrasion, plastic deformation and fatigue. Abrasion dominates liner wear during the engine break-in period. Hard particles, contained in the oil film from the combustion zone or a by-product of wear, can further result in abrasive wear.

Ting's analytical solution to determine cylinder bore wear pattern caused by the reciprocating motion of the piston ring was confirmed by subsequent experiment [14] [14].

Gangapadhyay developed a two-body abrasive wear model for steady-state wear of cylinder bore and piston rings based on Archard's wear equation [37]. Here the predicted bore wear depth correlated well with the measurement in vehicles.

Tung and Huang's model based on a laboratory simulator, was developed for the progression of the wear of piston ring/cylinder bore system [38]. Their three-body wear models addresses effects of temperature, load, oil degradation, surface roughness, and material properties.

## 1.3 Contribution of the Dissertation

Appropriate modelling of the piston assembly lubrication mechanism is paramount to successful piston assembly friction and cylinder liner wear prediction. To include effects of the surface asperity contact in the ring-liner interface, a mixed lubrication model which unifies the lubricant flow under different ring-liner gaps is needed. This dissertation formulates an overall model of mixed film lubrication of piston ring wherein hydrodynamic action is described by an Average Reynolds equation and dry contact action is described by the Greenwood-Tripp rough surface asperity contact model.

In the numerical solution, Reynolds equation is approximated by the central finite-differences, and the Gaussian-Seidel iterative method is applied to the difference equation. An algorithm based on convergent error balances convergence rate and numerical accuracy.

Peeken's flow factor, which includes surface contact effects, is implemented in the average Reynolds equation. The ring-liner friction predicted by the model agrees well with a corresponding bench test. The model also shows a significantly reduced coefficient of dry friction. This value gives a more physically meaningful explanation [29] [39].

A soft elastohydrodynamic lubrication model for a piston ring is proposed. A global ring elastic surface deformation is included in the film thickness function, and an inverse iterative numerical solution is applied to solve the EHL problem.

A quasi-Rayleigh gas flow model is incorporated in a piston ring pack lubrication analysis. A numerical algorithm is developed to solve ring dynamics, crevice gas flow, and ring lubrication simultaneously. A complete ring pack friction prediction is attained. The axial-motions of two compression ring are also estimated and agree with experiment.

A new mixed lubrication model, which couples parallel sliding, journal bearing, and side-slip mechanisms, describes the low friction phenomenon of Rotating Liner Engine (RLE) design. Numerical results show that surface contact can be possibly eliminated by the introduction of liner rotation, under normal engine working conditions.

Finally, the liner wear depth and progression is predicted by a simplified three-body cylinder liner wear model after a complete lubrication analysis of conventional and rotating liner engine designs.

## 1.4 Organization of the Dissertation

This dissertation is organized as follows.

Chapter 2 describes a generalized Reynolds equation in tensor form, including numerical solution scheme. In subsequent chapters, different forms of Reynolds equation are introduced. Numerical solutions are validated by comparing results to known solutions.

Chapter 3 presents three piston ring lubrication models - hydrodynamic, elastohydrodynamic and mixed film models. A new mixed film lubrication model estimates the piston ring friction loss under test-ring condition. Cylinder honing pattern is stochastically related to corrective flow factors.

Chapter 4 incorporates a new gas flow model into the piston ring friction analysis. Piston ring axial-motion is also presented.

Chapter 5 develops a dynamic piston skirt lubrication model to calculate the oscillatory secondary motion of piston and friction loss.

Chapter 6 assesses the merit of Sleeve-Valve Engine(SVE) mechanism. Both parallel sliding and side-slip will be incorporated with the piston assembly friction analysis. The low mechanical friction loss of Rotating Liner Engine (RLE) will be explained by this corresponding model.

Chapter 7 estimates cylinder liner wear based on the piston ring lubrication model results.

Chapter 8 summarizes and presents overall conclusions.

# Chapter 2

# Reynolds Equation and Numerical Solution

## 2.1 Reynolds Equation

To minimize friction and eliminate wear, hydrodynamic lubrication of a piston ring and cylinder liner brings a thin film of engine oil between ring and liner surfaces in relative motion. The thin film of oil that separates the surfaces prevents physical contact between these surfaces. Here:

- resistance to motion arises from "internal friction" of the fluid, i.e., the shear resistance or "viscosity" of the fluid film.
- wear diminishes if the surface geometry and motion encourages load-carrying pressure which in the lubricant film separates the surfaces.

In 1886, Osborne Reynolds successfully proved that hydrodynamic pressure generated in a viscous liquid can physically separate two sliding surfaces. The brief derivation of Reynolds equation is introduced as follows. Einstein summation notation is used as the indicial notation.

Reynolds started with the mass conservation law or continuity equation,

$$\frac{\partial \rho}{\partial t} + \frac{\partial}{\partial x_i}(\rho u_i) = 0, \tag{2.1}$$

where $\rho$ is the fluid density and $u_i$ is the fluid velocity along the direction of $x_i$ axis.

Followed by conservation of linear momentum,

$$\rho \left( \frac{\partial u_i}{\partial t} + u_j \frac{\partial u_i}{\partial x_j} \right) = \rho f_i + \frac{\partial \sigma_{ij}}{\partial x_j}. \tag{2.2}$$

Here $f_i$ is the external mass force density and $\sigma_{ij}$ is the stress tensor. Equation (2.2) establishes three relationships along space variable components $x_i$.

For common Newtonian fluids, the fluid rheological behavior can be written as

$$\sigma_{ij} = (-p - \frac{2}{3}\eta \frac{\partial u_k}{\partial x_k})\delta_{ij} + \eta \left( \frac{\partial u_i}{\partial x_j} + \frac{\partial u_j}{\partial x_i} \right), \tag{2.3}$$

where $\eta$ is the absolute viscosity, p is the hydrostatic pressure, and $\delta_{ij}$ is the Kroenecker delta defined as

$$\delta_{ij} \equiv \begin{cases} 1 & \text{for } i = j \\ 0 & \text{for } i \neq j \end{cases} \tag{2.4}$$

By substituting Equation (2.3) into (2.2) and assuming the constant fluid viscosity, the Navier-Stokes equation can be obtained

$$\rho \left( \frac{\partial u_i}{\partial t} + u_j \frac{\partial u_i}{\partial x_j} \right) = \rho f_i - \frac{\partial p}{\partial x_i} + \eta \left( \frac{\partial^2 u_i}{\partial x_k \partial x_k} + \frac{1}{3} \frac{\partial^2 u_k}{\partial x_k \partial x_i} \right). \tag{2.5}$$

The above Navier-Stokes equation can be further simplified by assuming constant density or incompressible flow

$$\rho\left(\frac{\partial u_i}{\partial t}+u_j\frac{\partial u_i}{\partial x_j}\right)=\rho f_i-\frac{\partial p}{\partial x_i}+\eta\left(\frac{\partial^2 u_i}{\partial x_k \partial x_k}\right). \quad (2.6)$$

The corresponding continuity equation is

$$\frac{\partial u_i}{\partial x_i}=0. \quad (2.7)$$

Three equations of motion (Eq. (2.5) or (2.6)) combined with the continuity equation (Eq. (2.1) or (2.7)), provide a complete mathematical description of the flow. Exact solutions are difficult because of nonlinear convective acceleration terms (i.e. $u_i \frac{\partial u_i}{\partial x_i}$). Only special cases, such as laminar flow between parallel flat plates, or circular pipes can be solved in closed-form.

Reynolds equation describes thin film behavior between narrow channels. Here the following assumptions often apply (Table 2.1).

| Assumption | Comments |
|---|---|
| a. Body force are neglected | Always valid except for magnetohydrodynamic fluid |
| b. Pressure constant across the film thickness | Always valid, since hydrodynamic film is micrometer thickness |
| c. No slip at the boundaries | Valid, except for rarefied gas films |
| d. Newtonian fluid | Usually valid, except for polymeric oils |
| e. Flow is laminar | Usually valid, except for large bearing, e.g.turbines |
| f. Fluid density constant | Usually valid for small thermal expansion. Not valid for gas |
| g. Fluid inertia neglected | Valid for low bearing speed or high load |
| h. Fluid viscosity constant | Crude, usually use effective viscosity |

Table 2.1: Summary of assumptions on Reynolds equation derivation

Application of assumptions a,d-h from table 2.1 permits Navier-Stokes equation (2.6) to be written as

$$-\frac{\partial p}{\partial x_i} + \eta \left( \frac{\partial^2 u_i}{\partial x_k \partial x_k} \right) = 0. \tag{2.8}$$

For most of bearing geometries, dimensional analysis indicates that terms of order h/W or h/B are second-order and less than $\frac{1}{1000}$. Here h is the film thickness, and W and B are the width and length of bearing area. Application of assumption b to Equation (2.8) applied to the coordinate system in Figure 2.1 yields the simplified momentum equations.

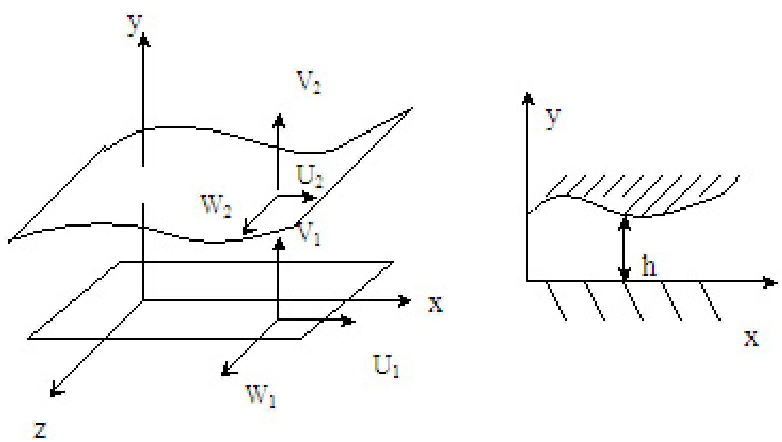


Figure 2.1: Coordinate system and notations

$$\frac{\partial^2 u}{\partial y^2} = \frac{1}{\eta}\frac{\partial p}{\partial x} \tag{2.9}$$

$$\frac{\partial^2 v}{\partial y^2} = 0 \tag{2.10}$$

$$\frac{\partial^2 w}{\partial y^2} = \frac{1}{\eta}\frac{\partial p}{\partial z} \tag{2.11}$$

Integration of the above equations with no-slip boundary velocities renders three flow velocity components

$$u = \frac{1}{2\eta}\frac{\partial p}{\partial x}y(y-h) + U_1 + \frac{y}{h}(U_2 - U_1) \tag{2.12}$$

$$v = (V_2 - V_1)\frac{y}{h} + V_1 \tag{2.13}$$

$$w = \frac{1}{2\eta}\frac{\partial p}{\partial z}y(y-h) + W_1 + \frac{y}{h}(W_2 - W_1) \tag{2.14}$$

In equation (2.12) to (2.14), $U_1$, $U_2$, $V_1$, $V_2$, $W_1$ and $W_2$ are boundary velocities defined in Figure 2.1. By substituting Equation (2.12 )-(2.14) into the continuity equation (2.7), and integrating across the film thickness with the aid of Leibnitz's rule, the generalized Reynolds equation for an incompressible fluid is

$$\begin{aligned}\frac{\partial}{\partial x}\left(\frac{h^3}{\eta}\frac{\partial p}{\partial x}\right) + \frac{\partial}{\partial z}\left(\frac{h^3}{\eta}\frac{\partial p}{\partial z}\right) = 6(-U_1 + U_2)\frac{\partial h}{\partial x} + 6(-W_1 + W_2)\frac{\partial h}{\partial z} \\ +6h\frac{\partial(U_1 + U_2)}{\partial x} + 6h\frac{\partial(W_1 + W_2)}{\partial z} \\ +12(V_2 - V_1)\end{aligned} \tag{2.15}$$

The two terms on the left-side are Poiseuille terms that describe net flow rates due to pressure gradients. The first two terms on the right-side are physical "wedge" terms, the third and fourth terms are "stretch" terms. Those four terms consist of the Couette terms describing the net entraining flow rates due to surface velocities. The last term is the net flow rate due to a squeezing motion.

For most steady-state practical engineering applications, the generalized Reynolds equation can be simplified as

$$\frac{\partial}{\partial x}\left(\frac{h^3}{\eta}\frac{\partial p}{\partial x}\right)+\frac{\partial}{\partial z}\left(\frac{h^3}{\eta}\frac{\partial p}{\partial z}\right)=6U\frac{\partial h}{\partial x}+6W\frac{\partial h}{\partial z}+12\frac{\partial h}{\partial t}, \tag{2.16}$$

Here $U = U_2 - U_1, W = W_2 - W_1$ are boundary velocities and t is time. The "squeeze" term is equivalent to $\frac{\partial h}{\partial t} = V_2 - V_1$.

## 2.2 Numerical Methodology

The numerical solution method for Reynolds equation (2.16), employed central finite difference approximations

$$\frac{\partial}{\partial x}(\frac{h^3}{\eta}\frac{\partial p}{\partial x}) \doteq \frac{h^3_{i+1/2,j}\frac{p_{i+1,j}-p_{i,j}}{\Delta x} - h^3_{i-1/2,j}\frac{p_{i,j}-p_{i-1,j}}{\Delta x}}{\eta\Delta x}, \tag{2.17}$$

$$\frac{\partial}{\partial z}(\frac{h^3}{\eta}\frac{\partial p}{\partial z}) \doteq \frac{h^3_{i,j+1/2}\frac{p_{i,j+1}-p_{i,j}}{\Delta z} - h^3_{i,j-1/2}\frac{p_{i,j}-p_{i,j-1}}{\Delta z}}{\eta\Delta z}, \tag{2.18}$$

$$\frac{\partial h}{\partial x} \doteq \frac{h_{i+1/2,j} - h_{i-1/2,j}}{\Delta x}, \tag{2.19}$$

$$\frac{\partial h}{\partial z} \doteq \frac{h_{i,j+1/2} - h_{i,j-1/2}}{\Delta z}, \tag{2.20}$$

for spatial derivatives, and forward differences

$$\frac{\partial h}{\partial t} \doteq \frac{h^{n+1}_{i,j} - h^n_{i,j}}{\Delta t}. \tag{2.21}$$

for time derivative. Here $\Delta x$, $\Delta z$, and $\Delta t$ are increments in space and time. Subscripts denote the value of a quantity at a position $x$ and $z$. Superscripts indicate time.

In explicit form, Reynolds equation with above the difference approximations of equations (2.17) to (2.21) leads to

$$p_{i,j} = a^0_{i,j} + a^1_{i,j} p_{i+1,j} + a^2_{i,j} p_{i-1,j} + a^3_{i,j} p_{i,j+1} + a^4_{i,j} p_{i,j-1}, \tag{2.22}$$

where coefficients

$$\begin{aligned}
a^0_{i,j} &= \frac{-6U\frac{h_{i+1/2,j}-h_{i-1/2,j}}{\Delta x} - 6W\frac{h_{i,j+1/2}-h_{i,j-1/2}}{\Delta z} - 12\frac{h^{n+1}_{i,j}-h^n_{i,j}}{\Delta t}}{\Pi}, \\
a^1_{i,j} &= \frac{\frac{h^3_{i+1/2,j}}{\Delta x^2}}{\Pi}, \\
a^2_{i,j} &= \frac{\frac{h^3_{i-1/2,j}}{\Delta x^2}}{\Pi}, \\
a^3_{i,j} &= \frac{\frac{h^3_{i,j+1/2}}{\Delta z^2}}{\Pi}, \\
a^4_{i,j} &= \frac{\frac{h^3_{i,j-1/2}}{\Delta z^2}}{\Pi}, \\
\Pi &= \eta\frac{h^3_{i+1/2,j} + h^3_{i-1/2,j}}{\Delta x^2} + \eta\frac{h^3_{i,j+1/2} + h^3_{i,j-1/2}}{\Delta z^2}.
\end{aligned}$$

For M x N mesh points, there will be M x N simultaneous equations governing pressure $p_{i,j}$. The resulting liner system can be written in matrix form and solved by standard matrix solvers or by an iterative methods. The Gaussian-Seidel iteration method was adopted in this study.

## 2.3 Results and Discussions

A computational fluid dynamics (CFD) code was developed to solve the multi-dimensional Reynolds equation numerically. Accuracy and convergence of the numerical method and algorithm were validated by problems with closed-form solution, such as inclined-pad thrust bearing and journal bearing. The code is listed in Appendix A. The inclined pad thrust bearing and the journal bearing were chosen as test cases for the numerical solution codes, because these have geometries and flows similar to piston rings in reciprocating and rotating liner engines.

### 2.3.1 Inclined-Pad Thrust Bearing

Figure 2.2 depicts an inclined-pad thrust bearing having two nonparallel plane surfaces separated by an oil film. The lower inclined surface is stationary while the upper moves with uniform velocities U and V. The direction of motion and the inclination of planes create flow into a converging channel between the surfaces. A physical wedge pressure-generating mechanism is developed in the oil film.

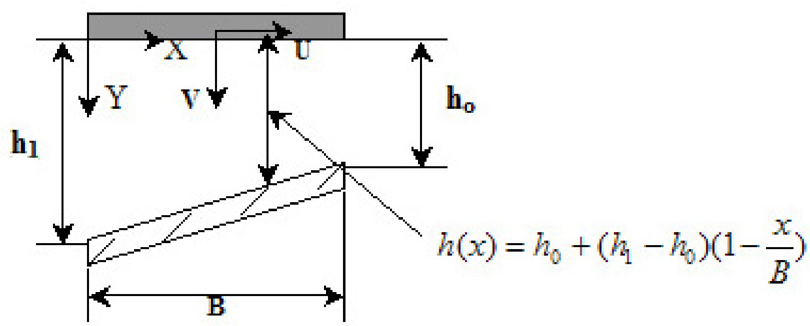


Figure 2.2: Incline-pad Slider Bearing Interface

The lubricant pressure is governed by the Reynolds equation:

$$\frac{\partial}{\partial x}(\frac{h^3}{\eta}\frac{\partial p}{\partial x}) + \frac{\partial}{\partial z}(\frac{h^3}{\eta}\frac{\partial p}{\partial z}) = 6U\frac{\partial h}{\partial x} + 12V. \tag{2.23}$$

A particular solution of Equation (2.23) solves

$$\frac{\partial}{\partial x}(\frac{h^3}{\eta}\frac{\partial p_p}{\partial x}) = 6U\frac{\partial h}{\partial x} + 12V. \tag{2.24}$$

Here the pressure

$$p_p = p_p(x) = \frac{6\eta nUx(1-\frac{x}{B})}{h^2(2h_0+n)} - \frac{12\eta BVx(1-\frac{x}{B})}{h^2(2h_0+n)}, \tag{2.25}$$

where

$$n = h_1 - h_0. \tag{2.26}$$

A homogenous solution for Equation (2.23) solves the homogenous equation

$$\frac{\partial}{\partial x}(\frac{h^3}{\eta}\frac{\partial p_h}{\partial x}) + \frac{\partial}{\partial z}(\frac{h^3}{\eta}\frac{\partial p_h}{\partial z}) = 0. \tag{2.27}$$

Let $p_h(x,z) = X(x)Z(z)$. Substituting into Equation (2.27) gives

$$\frac{d}{dx}(h^3\frac{dX}{dx}) + \Lambda^2 h^3 X = 0, \tag{2.28}$$

$$\frac{d^2 Z}{d^2 z} - \Lambda^2 Z = 0. \tag{2.29}$$

Where $\Lambda$ is the eigenvalue of the Sturm Louville problem.

Four pressure boundary conditions are imposed at the edges of bearing area

$$\begin{aligned}
0 = p(0,z) &= p_p(0) + p_h(0,z), \\
0 = p(B,z) &= p_p(B) + p_h(B,z), \\
0 = p(x,-L/2) &= p_p(x) + p_h(x,-L/2), \\
0 = p(x,L/2) &= p_p(x) + p_h(x,L/2).
\end{aligned}$$

The particular solution (2.25) indicates $p_p(0) = 0$ and $p_p(B) = 0$ are automatically satisfied. With $p_h$ having an implied symmetry along z, boundary conditions for functions $X(x)$ and $Z(z)$ can be derived from the above conditions:

$$X(0) = X(B) = 0, \tag{2.30}$$

$$\frac{dZ}{dz}(z=0) = 0. \tag{2.31}$$

While equation (2.28) and boundary (2.30) forms a Sturm Liouville problem, equation (2.29) and boundary (2.31) indicate another boundary value problem. The following homogenous solution can be obtained by solving the two boundary value problems

$$p_h(x,z) = X(x)Z(z) = \sum_{n=1}^{n=\infty} c_n \phi_n(x) cosh(\Lambda_n z). \tag{2.32}$$

Here $\phi_n$ and $\Lambda_n$ are the eigenfunction and eigenvalue of Sturm Liouville problem, respectively. The coefficient $c_n$ is obtained via boundary conditions,

$$p_h(x, \pm\frac{L}{2}) + p_p(x) = 0, \tag{2.33}$$

can be expressed as

$$c_n = \frac{(-p_p(x), \phi_n(x))}{(\phi_n(x), \phi_n(x))} \frac{1}{cosh(\Lambda \frac{L}{2})}. \tag{2.34}$$

Finally, the exact solution $p(x,z) = p_p(x) + p_h(x,z)$. Here $p_p$ and $p_h$ are obtained by equation (2.25) and (2.32), respectively.

Table 2.2 contains incline-pad bearing parameters for both numerical and closed-form solutions. In the numerical practice, a set of uniform grid size is used. Here the number of grid point is 80 x 80 and $\Delta x = \Delta z = 0.0125$ m.

Figure 2.3 shows the numerically solved lubrication pressure distribution, and Figure 2.4 shows the exact closed-form counterpart. Figure 2.5 compares exact solution (solid line) and numerical solution (dash line) - pressure versus bearing

| Bearing Parameter | Selected Value (SI Unit) |
|---|---|
| Bearing Length B | 1 |
| Bearing Width L | 1 |
| Minimum Gap $h_0$ | 0.001 |
| Maximum Gap $h_1$ | 0.0012 |
| Sliding Speed | 1 |
| Squeeze Speed | 0.005 |
| Absolute Viscosity | 1 |

Table 2.2: Inclined slider bearing parameters

width direction z. Figure 2.6 compares exact solution (solid line) and numerical solution (dash line) - pressure versus bearing width direction x. The maximum relative errors in these figures are less than 3 % percent for pressure.

### 2.3.2 Journal Bearing

Figure 2.7 depicts a journal bearing which support shafts and carries radial loads with minimum power loss and wear. The journal bearing can be represented by a plain cylindrical sleeve (bushing) wrapped around the journal (shaft). Shaft motions generate load-supporting pressures in the lubricant film.

Eccentricity e is the distance between centers of shaft and bearing. Assume the nominal clearance between shaft and bearing is c. The film thickness h in the arbitrary position $\theta$ (see Figure 2.7) is

$$h = c + ecos\theta. \tag{2.35}$$

A short-journal bearing theory will be applied, since the thickness of a piston ring is much smaller than its total length. The circumferential pressure gradient can be neglected in comparison with the axial pressure gradient. With these simplification, the Reynolds equation becomes

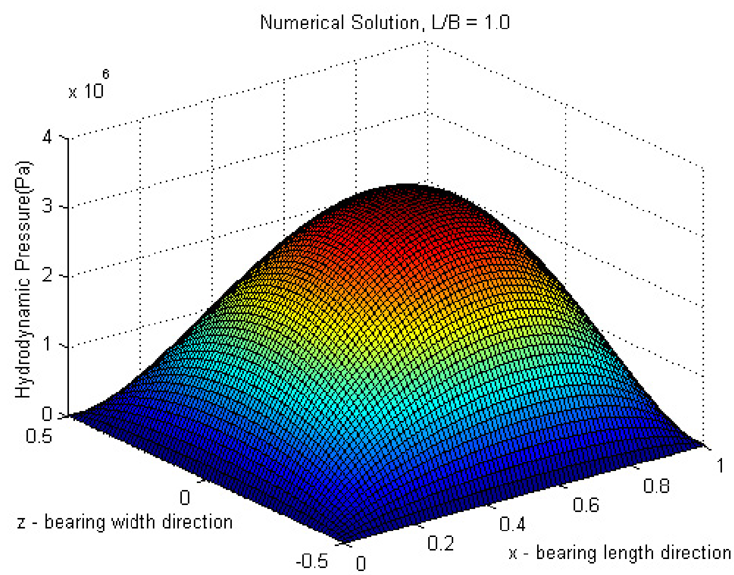


Figure 2.3: Hydrodynamic Lubrication Pressure by Numerical Method

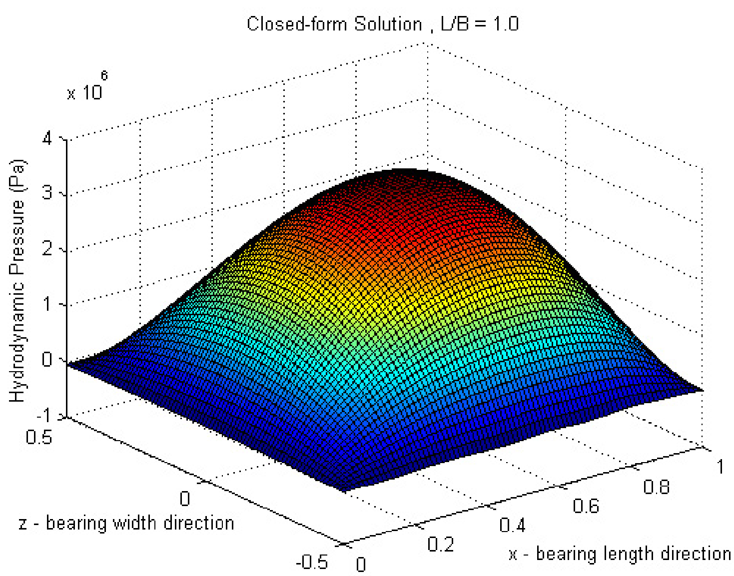


Figure 2.4: Hydrodynamic Lubrication Pressure by Close-form Solution

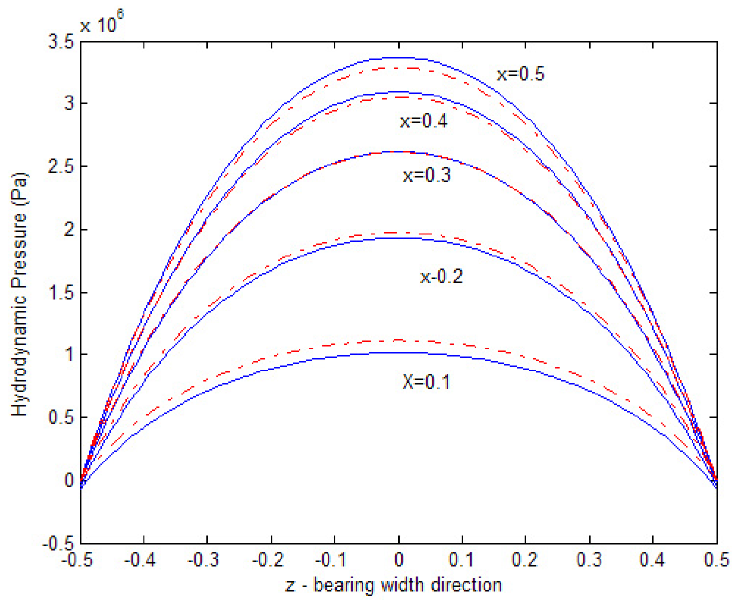


Figure 2.5: Hydrodynamic Lubrication Pressure

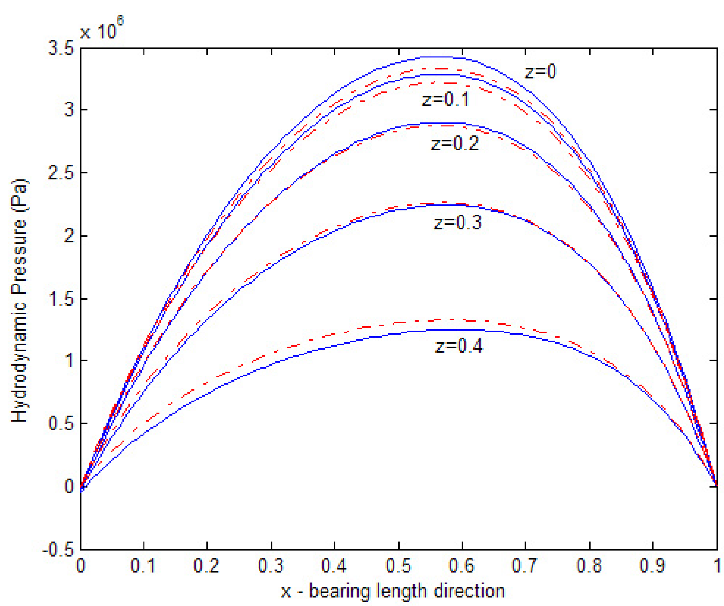


Figure 2.6: Hydrodynamic Lubrication Pressure

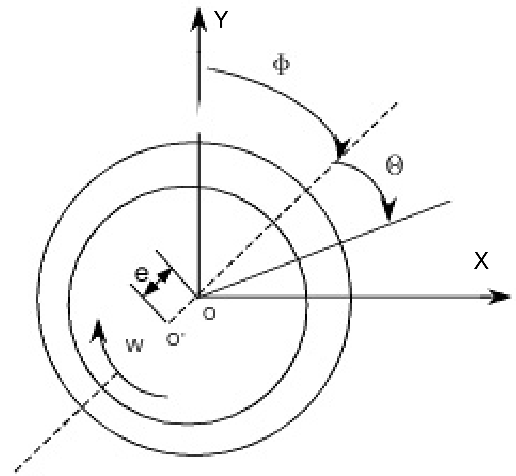


Figure 2.7: Journal bearing geometry

$$\frac{\partial}{\partial z}(\frac{h^3}{\eta}\frac{\partial p}{\partial z}) = 6\omega\frac{\partial h}{\partial \theta}. \tag{2.36}$$

with the boundary conditions

$$p(\theta, z = \pm\frac{L}{2}) = 0. \tag{2.37}$$

From [40], closed-form solution for the pressure distribution

$$p(z,\theta) = -\frac{3\eta\omega}{c^2}(x^2 - \frac{L^2}{4})\frac{\epsilon sin(\theta)}{(1+\epsilon cos(\theta))^3}. \tag{2.38}$$

The supporting load on the shaft

$$F = \eta LR\omega(\frac{L}{D})^2(\frac{R}{c})^2\frac{\epsilon}{(1-\epsilon^2)^2}\left[16\epsilon^2 + \pi^2(1-\epsilon^2)\right]^{0.5}. \tag{2.39}$$

Here L is journal axial length, D is bearing diameter, R is radius of bearing, $\omega$ is shaft rotating speed, and $\epsilon$ is ratio of eccentricity and is equal to e/c.

Table 2.3 contains the journal bearing parameters for both numerical and closed-form solutions.

| Bearing Parameter | Selected Value(SI Unit) |
|---|---|
| Shaft Diameter | 0.0889 |
| Bearing Width L | 0.001475 |
| Nominal Clearance c | 0.000002 |
| Shaft Rotating Speed | 50 |

Table 2.3: Journal bearing parameters

In the numerical practice, a set of grid size 40 x 80 is used, and $\Delta z = 0.0022$ m, $\Delta\theta = 4.5$ degree.

Figure 2.8 compares exact solution (solid line) and numerical solution (dash line) of journal bearing pressure distribution with different eccentricity, the maximum error is 2 %. Figure 2.9 compares exact solution (solid line) and numerical solution (dash line) of journal bearing generated load acting on shaft with different eccentricity, the maximum error is 7 %. From Figure 2.8 and Figure 2.9, both pressure and its corresponding load monotonically increase with eccentricity ratio.

Although Reynolds' theory remains the fundamental approach to hydrodynamic lubrication, later work has shown that Reynolds equation is rarely applicable in its original form. The following effects should be considered in practical applications [41] [42] [40].

- Surface roughness. When the film thickness is the same order of surface asperity height, equation (2.14) is no longer valid.
- Pressure on oil viscosity. Extremely high pressure can change the physical properties of oil
- Temperature on oil viscosity. Even with the best lubricant, a temperature increment of 10 % may reduce viscosity to half its original value

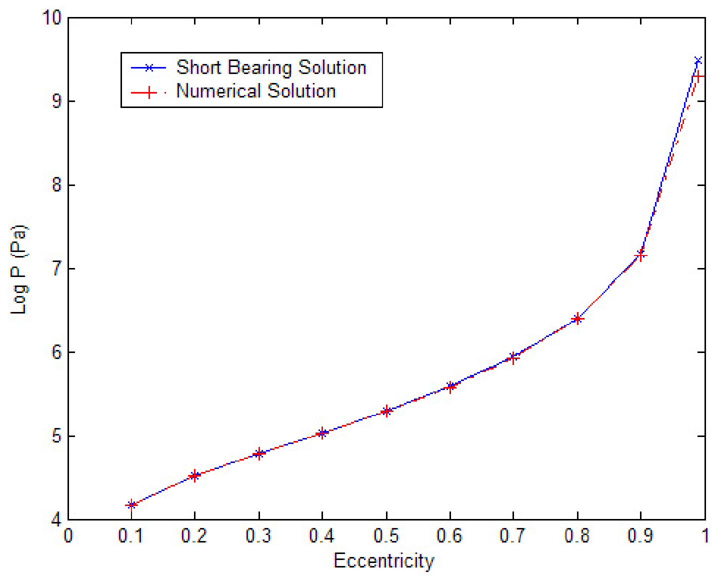


Figure 2.8: Hydrodynamic Lubrication Pressure under Different Eccentricity

- High rates of shear on the viscosity of oil. This often decreases viscosity.

These effects are difficult to deal with theoretically. Theory-experiment comparisons indicate temperature to be the most important factor.

## 2.4 Summary

A generalized Reynolds equation was derived, followed by a numerical solution method. Solution of inclined-pad thrust bearing and journal bearing by a finite difference method with Gaussian-Seidel iterative scheme is effective and reliable.

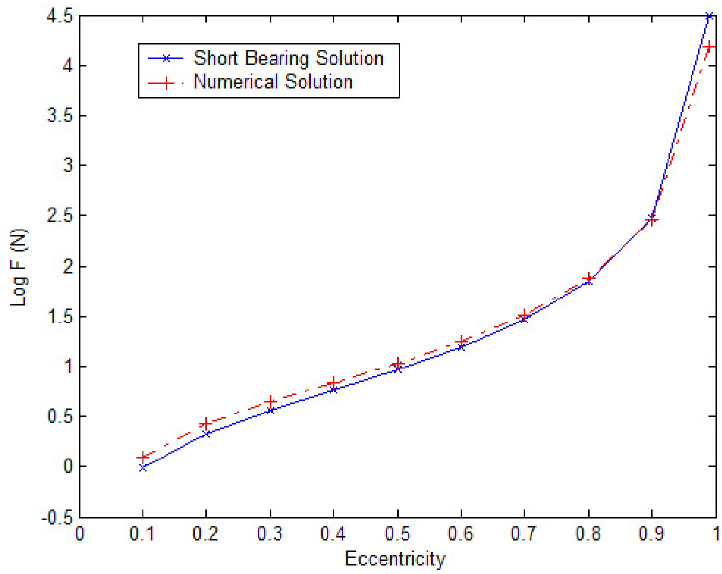


Figure 2.9: Acting Load on Shaft Under Different Eccentricity

# Chapter 3

# Lubrication Analysis of Piston Ring

## 3.1 Piston Ring Lubrication Models

### 3.1.1 Hydrodynamic Lubrication Model

Lubricant behavior between piston ring and cylinder wall is analogous to a dynamically-loaded slider bearing moving over a plane surface. Figure 3.1 depicts a piston ring and a liner wall interface. Coordinates x and z are oriented in the axial and circumferential direction. The piston reciprocates along the x direction.

Both sliding and squeeze motions of the piston ring against the liner surface are included in the lubrication model. The lubricant is assumed incompressible and isothermal. From the generalized Reynolds equation (2.16), the only non-zero sliding boundary velocities are the reciprocating speed of the piston $U_1$; the liner rotating speed $W_2$ for the rotating liner engine (RLE); and for the two surfaces approaching each other, the squeeze velocity $V_2 - V_1$ in the y-direction is given by

$$V_2 - V_1 = \frac{\partial h}{\partial t}.$$

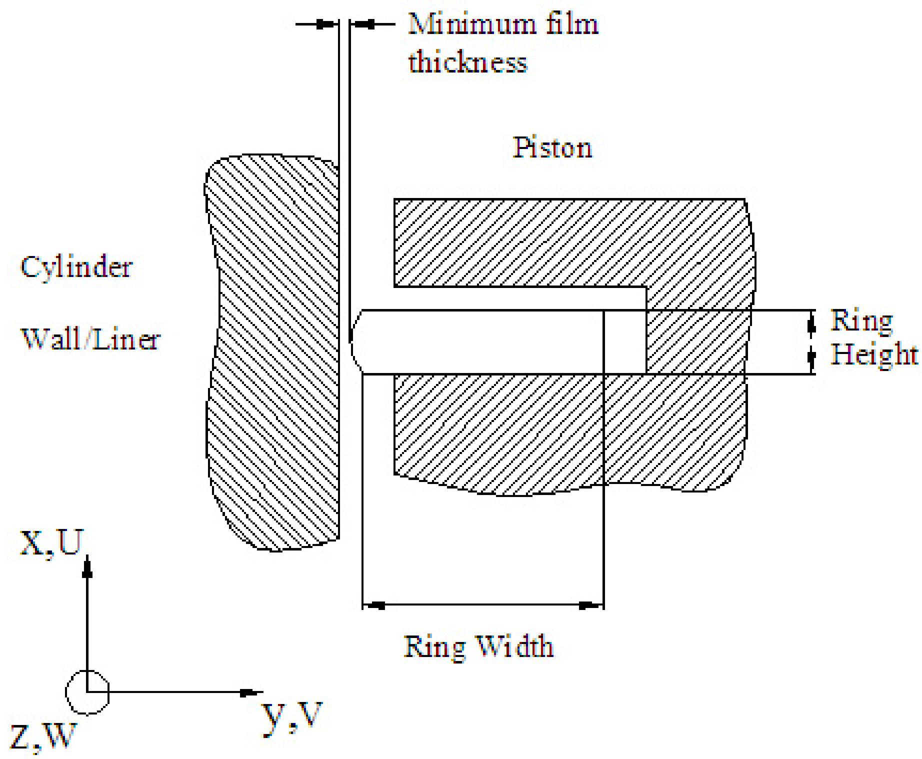


Figure 3.1: Piston Ring and Cylinder Liner Interface

The full Reynolds equation for 1D and 2D piston ring and liner lubrication can be written as

$$\frac{\partial}{\partial x}(\frac{h^3}{\eta}\frac{\partial p}{\partial x}) = 6U_1\frac{\partial h}{\partial x} + 12\frac{\partial h}{\partial t}. \tag{3.1}$$

$$\frac{\partial}{\partial x}(\frac{h^3}{\eta}\frac{\partial p}{\partial x}) + \frac{\partial}{\partial z}(\frac{h^3}{\eta}\frac{\partial p}{\partial z}) = 6U_1\frac{\partial h}{\partial x} - 6W_2\frac{\partial h}{\partial z} + 12\frac{\partial h}{\partial t}. \tag{3.2}$$

In equations (3.1) and (3.2), the film thickness h and the hydrodynamic pressure p are unknown variables. For a given h, hydrodynamic pressure p must satisfy boundary and equilibrium conditions. The film thickness function depends on the ring and liner geometry

$$h(x, z, t) = h_x(x) + h_z(z) + h_{min}(t). \tag{3.3}$$

Here $h_x(x)$ describes the oil film thickness due to ring running over the surface profile in the piston motion direction x, $h_z(z)$ is the oil film thickness due to variations in gap between ring and liner in the circumferential direction z, and $h_{min}(t)$ is the minimum oil film thickness at a certain crank angle.

The film thickness function is crucial to modeling of hydrodynamic lubrication. Main contributions to the film thickness function are

- Ring and liner geometries [22]
- Ring and liner surface waviness and roughness
- Ring rigid-body displacement due to eccentricity and piston secondary motion
- Ring deformation
- Bore Distortion

With appropriate velocity and pressure boundary conditions, for a given computational domain, hydrodynamic pressures solved from Reynolds equation (3.1) or (3.2) are generally positive for most bearing designs, however, nothing prevents the theoretical solution from having negative pressures. In particular, since the piston ring running surface has both a convergent and a divergent profile, the Sommerfeld solution predicts positive pressure over the convergent area and negative pressure over the divergent area. Such negative pressure is physically unacceptable, since a fluid can not sustain tension (negative pressure). In such cases, fluid films rupture and evaporate, and the pressure is limited by the vapor pressure of the fluid. This fluid cavitation process in piston-ring lubrication affects the outlet pressure boundary condition. To incorporate this cavitation effect into the 1D model, a modified Reynolds pressure condition is applied

$$p_{out} = p_(x_c, z, t) = p_T, \frac{\partial p}{\partial x}(x_c) = 0. \tag{3.4}$$

Here $p_T$ is the trailing edge pressure, $p_{out}$ is the downstream pressure, and $x_c$ is the position where the cavitation occurs. If a half-Sommerfeld pressure condition is applied to the 2D model, the negative pressures are simply dropped after obtaining the entire hydrodynamic pressure distribution.

The inlet pressure boundary condition usually assumes a full-flooded inlet boundary condition. The inlet pressure $p_{in}$ at the leading edge of the ring

$$p_{in} = p_L. \tag{3.5}$$

where the leading edge pressure $p_L$ depends on the ring and the direction of piston motion. For instance, $p_L$ represents the gas pressure of the combustion chamber for the first compression ring during the piston up-stroke. A complete ring pack analysis requires a gas flow model to obtain the inter-ring gas pressures, which serve as pressure boundaries.

An additional equilibrium condition is required to obtain a unique solution to equation (3.1) or (3.2). For the quasi-steady-state 1D lubrication problem, hydrodynamic pressure load should balance the distributed radial forces from gas pressure force behind the ring, and ring elastic deformation.

Finally, an initial condition is needed to solve a dynamically-loaded bearing. For simplicity, the initial and boundary value will start at the crank angle 90 degrees, where experiment observes a minimum squeeze film effect, and the piston absolute velocity is maximum. A good initial condition meets cyclic repeatability of solution.

Usually the minimum film thickness and hydrodynamic pressure can be solved from Reynolds equation (3.1) or (3.2), and the local film thickness function (3.3). The friction force between piston ring and cylinder liner is generated by a combination of viscous shear and oil film pressure gradient, and computed by:

$$f = \int_A \left(\frac{h}{2}\frac{dp}{dx} - \frac{\eta u}{h}\right) dA. \tag{3.6}$$

Conventional hydrodynamic theory dominated analysis of piston ring lubrication until the 1980s [3]. Piston rings experience full-film lubrication over most of the engine cycle; however, like many dynamically loaded reciprocating components, rings also experience mixed and boundary lubrication during the severe operation conditions near both TDC and BDC. A more realistic piston ring lubrication model will be presented in the later section.

### 3.1.2 Elastohydrodynamic Lubrication Model

Elastohydrodynamic lubrication (EHL) is hydrodynamic lubrication wherein elastic deformation of the lubricated surfaces becomes significant. Elastohydrodynamic lubrication is normally associated with nonconformal surfaces, such as gear teeth, cams, and rolling-element bearings. There are two distinct forms of EHL: hard EHL and soft EHL.

In hard EHL, the elastic deformation and the pressure-viscosity effects are equally important. The maximum pressure (typically between 0.5 and 3 GPa) and the minimum film thickness (normally exceeding 0.1 $\mu m$) are dramatically different from those found in a hydrodynamically lubricated conjunction. At loads normally experienced in nonconformal machine elements, the elastic deformations are several orders of magnitude larger than the minimum film thickness. Furthermore, the lubricant viscosity can vary as much as 10 orders of magnitude within the lubricated conjunction.

In soft EHL, the elastic distortions are large, even with light loads. The maximum pressure for soft EHL, typically 1 MPa, has negligible effect on the viscosity variation throughout the conjunction. The minimum film thickness for soft EHL is typically 1 $\mu m$.

A complete EHL model involves solving 6 simultaneous equations for the film shape and pressure distribution throughout the lubricated contact. Those equations are

- Reynolds equation
- Film thickness equation
- Elastic deformation equation
- Viscosity-pressure equation
- Density-pressure equation
- Force equilibrium equation

Barus' relationship between viscosity and pressure [43].

$$\eta(p) = \eta_0 exp(\alpha p) \tag{3.7}$$

has atmospheric viscosity $\eta_0$ and pressure viscosity coefficient $\alpha$. For mineral oils, coefficient $\alpha$ varies between $1 \cdot 10^{-8}$ and $2 \cdot 10^{-8} Pa^{-1}$.

A more realistic viscosity pressure relations proposed by Roelands,

$$\eta(p) = \eta_0 exp\left[(ln(\eta_0) + 9.67)(-1 + (1 + \frac{p}{p_0})^z)\right] \tag{3.8}$$

has pressure viscosity index $z_p$, (typically $z_p$ =0.6) and constant $p_0 = 1.96 \cdot 10^8$ [Pa].

If hydrodynamic pressure is 1 GPa, a predicted new viscosity is about $e^{10} = 22026$ times of an original value from equation (3.7). If hydrodynamic pressure is

1 MPa, a predicted new viscosity is about 10 times of an original value and the viscosity-pressure dependence can be neglected.

A simple density pressure relation by the Dowson and Higginson formulation [44],

$$\rho(p) = \rho_0 \frac{5.9 \cdot 10^8 + 1.34p}{5.9 \cdot 10^8 + p} \tag{3.9}$$

where $\rho_0$ is the atmospheric density and $p$ is given pressure value in [Pa]. For pressure of 1 GPa, a predicted new density is about 1.2 times of an original value. For a pressure of less than 10 MPa, the variation of density can be neglected.

Piston ring elastohydrodynamic lubrication analysis was first conducted by Dowson et al. in the early 1980s [24]. Although hydrodynamic lubrication (HL) theory has been widely adopted to predict dynamic behavior of piston rings, results are poor near top dead center and especially at the beginning of the combustion cycle. For example, the calculated minimum film thickness can be smaller than the surface roughness [2]. A more elaborate lubrication theory must be developed. In general, the minimum film thickness predicted from EHL theory is thicker than that predicted by HL theory [24].

In analyzing lubrication, EHL requires much more computing time than HL. The coupling between Reynolds equation and elastic deformations is highly non-linear. Numerical methods for EHL include the inverse iterative method, Newton-Raphson method, the forward iterative method, and the multigrid method. Many researchers strive to develop more effective numerical algorithms to solve EHL. A non-linear finite element scheme, based on the Newton-Raphson-Murty algorithm, was developed by Hwu and Weng [26] to solve piston ring EHL. Wu and Chen [20] introduced the Multigrid method to solve piston ring EHL. The Multigrid method to solve EHL problem has been well documented by Venner and Lubrecht [43]. Yang and Keith [45] [46] incorporated a better cavitation algorithm into piston ring EHL model.

Hydrodynamic pressures from EHL piston ring models are less than 10 MPa under normal engine operating condition [24] [26]. Viscosity-pressure and density-pressure relationships, weakly-coupled to Reynolds equation permit the lubricant to be considered iso-viscous and incompressible. Although the local elastic deformation under hydrodynamic pressure is insignificant for a hard EHL [47], the global elastic deformation of the piston ring can be significant. Under these conditions, it is appropriate to treat the piston ring as a soft EHL. The numerical efficiency will be improved dramatically.

For a soft EHL applied to a piston ring,

$$\frac{\partial}{\partial x}\left(\frac{h^3}{\eta}\frac{\partial p}{\partial x}\right) = 6U_1\frac{\partial h}{\partial x} + 12\frac{\partial h}{\partial t} \tag{3.10}$$

$$h(x,t) = h_x(x) + \delta(t) \tag{3.11}$$

$$\delta(t) = \frac{p_m - p_{gas}}{Et_r}r^2 \tag{3.12}$$

Here the piston ring is treated as a thin-wall cylinder, $p_m$ is the mean value of hydrodynamic pressure, $p_{gas}$ is the gas pressure acting on the back of the ring, E is the Young's modulus of the ring, $t_r$ is the ring thickness, and r is the radius of the cylinder bore.

The numerical approach for the present EHL problem differs from classical hard EHL solutions. Employed is an inverse iterative algorithm - guessing a mean hydrodynamic pressure $p_m$ and substituting the corresponding film thickness derived from equations (3.11) and (3.12) into Reynolds equation yields a new mean hydrodynamic pressure. An error control routine controls convergence of the mean pressure and the final film thickness.

### 3.1.3 Mixed Lubrication Model

When hydrodynamic lubricant pressure is insufficient to separate surfaces, surface asperities contact. Such a lubricated contact is commonly known as mixed lubrication. The majority of machines operate in mixed lubrication regime. Usually a statistical macro-scale method or a deterministic micro-scale method describes mixed lubrication.

Tzeng and Saible studied stochastic surface roughness effects in lubrication [48]. Christensen and Tonder's stochastic Reynolds equation analyzed hydrodynamic lubrication of slider and journal bearings with transverse and longitudinal roughness [49] [50]. Majumdar and Hamrock applied Patir/Cheng's average Reynolds on hydrodynamic bearing study [51] [52]. In the past two decades, the employment of average Reynolds equation to solve conformal lubricated contacts, such as hydrodynamic bearings, piston skirt, and mechanical face seals has received considerable attention.

A deterministic micro-scale approach is suitable for concentrated small-area contact, such as rolling element bearings, gears and cams lubrication. Direct deterministic simulations usually require more computer power.

A stochastic technique is employed in the present study. Various flow factors have been estimated both analytically and numerically for different surface roughness orientations and contacts [53] [54] [55]. Patir/Cheng's average Reynolds equation coupled with Greenwood rough surface contact model can predict the piston ring mixed lubrication [29] [39] [56]. However, these models lack recent developments and most have not been validated experimentally.

The ring-liner lubrication characteristics were investigated by a test apparatus at Purdue University [57] [58] to validate the present piston ring mixed lubrication model. Both model and experiment show that piston rings experience hydrodynamic, mixed, and boundary lubrication during the course of a piston stroke.

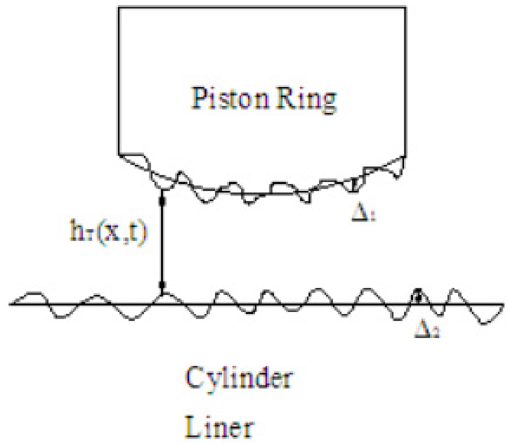


Figure 3.2: Rough piston ring and cylinder liner conjunction

**Average Reynolds Equation**

Figure 3.2 depicts a conjunction between piston ring and cylinder liner with surface roughness. Here the function $h_T(x,t)$ describes the local film thickness, including surface roughnesses.

In a mixed lubrication regime, Patir/Cheng's average Reynolds equation describes the isothermal, incompressible lubricant behavior between the ring and liner rough surfaces

$$\frac{\partial}{\partial x}(\phi_x \frac{h^3}{\eta}\frac{\partial \overline{p}}{\partial x}) + \frac{\partial}{\partial z}(\phi_z \frac{h^3}{\eta}\frac{\partial \overline{p}}{\partial z}) = 6U\frac{\partial \overline{h_T}}{\partial x} + 6U\sigma\frac{\partial \phi_s}{\partial x} + 12\frac{\partial \overline{h_T}}{\partial t}, \tag{3.13}$$

where $\phi_x$, $\phi_z$, $\phi_s$ are flow factors that depend upon surface roughness conditions. $\overline{p}$ is the mean pressure, and $\sigma$ is the composite rms roughness of ring and liner. The local film thickness $h_T$ is given by

$$h_T = h + \Delta_1 + \Delta_2 \tag{3.14}$$

Where h is the nominal film thickness, $\Delta_1$ is the ring surface roughness amplitude, and $\Delta_2$ is the liner surface roughness amplitude. The nominal film thickness $h = h_{min}(t) + h_x(x)$, giving

$$h_T = h_{min}(t) + h_x(x) + \Delta_1 + \Delta_2 \tag{3.15}$$

for one dimensional lubrication. The average gap $\overline{h_T}$ is defined as

$$\overline{h_T} = \int_{-h}^{\infty} (h + \Delta) f(\Delta) d\Delta \tag{3.16}$$

where $\Delta = \Delta_1 + \Delta_2$ is the combined roughness of ring and liner, and f is the probability density function that describes the statistics of surface roughness $\Delta$.

By omitting the lubricant ring circumferential flow leakage (generally small), the second term in equation (3.13), Reynolds equation applied to the ring-liner hydrodynamic lubrication analysis becomes

$$\frac{\partial}{\partial x}(\phi_x \frac{h^3}{\eta} \frac{\partial \overline{p}}{\partial x}) = 6U\phi_c \frac{\partial h}{\partial x} + 6U\sigma \frac{\partial \phi_s}{\partial x} + 12\phi_c \frac{\partial h}{\partial t}. \tag{3.17}$$

A contact factor $\phi_c$ is introduced

$$\phi_c = \frac{\partial \overline{h_T}}{\partial h} \tag{3.18}$$

to simplify the numerical implementation [59]. The first and third terms of the right side of equation (3.13) is written as $\frac{\partial h}{\partial x}$ and $\frac{\partial h}{\partial t}$ function in equation (3.17). Surface roughness has a profound effect on fluid flows. Surface roughness can affect flows near the surface, altering boundary layer flows. Flow factors capture the statistical properties of surface topography. However, it is difficult to describe engineering surfaces by a few statistical parameters. Some assumptions - such as no flow cavitation and no surface deformation, are too strong during the derivation of Patir/Cheng's average Reynolds equation. Studies show that Patir and Cheng's statistical model may over-estimate hydrodynamic action in the mixed regime [52] [55]. The present model will use flow factors derived by Peeken et al [55]. Details of flow factor selection are attached in Appendix B. Numerical procedures to solve the average Reynolds equation are similar to those for Reynolds equation, and will not be discussed further.

### Surface Asperity Contact

Surface asperities contact only when the hydrodynamic action is not sufficient to separate two interacting lubricated surfaces. Greenwood-Tripp's rough surface contact model estimated the asperity contact load based on the surface mean separation and other statistical parameters. The average contact pressure $P_a$ was related to density of asperities $\eta$, curvature of asperity of radius $\beta$, composite surface roughness $\sigma$, and composite material modulus $E$ [31].

$$P_a(h) = \frac{16\sqrt{2}}{15}\pi(\sigma\beta\eta)^2 E\sqrt{\frac{\sigma}{\beta}}F_{2.5}(\frac{h}{\sigma}) \tag{3.19}$$

where:

$$F_{2.5}(x) = \frac{1}{\sqrt{2\pi}}\int_x^\infty (s-x)^{2.5}e^{-\frac{s^2}{2}}\,ds \tag{3.20}$$

and

$$\frac{1}{E} = \frac{1-\nu_1^2}{E_1} + \frac{1-\nu_2^2}{E_2} \tag{3.21}$$

In equations (3.19) to (3.21), $E_1$ and $E_2$ are ring and liner Young's modulus, and $\nu_1$ and $\nu_2$ are ring and liner poisson's ratio.

### Friction Force

The shearing of asperities, surface films, and viscous lubricant film creates the friction force in the mixed lubrication regime. The hydrodynamic component of friction force $F_h$ is given by the integration of viscous shear stress

$$F_h = \int_A \left[ \phi_{fp} \frac{h}{2} \frac{dp}{dx} - (\frac{h}{\overline{\overline{h_T}}} + \phi_{fs}) \frac{\eta u}{h} \right] dA \tag{3.22}$$

Where $\phi_{fp}$ and $\phi_{fs}$ are shear flow factors. The asperity component of friction force is given by Amontons' law

$$F_a = \mu_f W_a. \tag{3.23}$$

Here $W_a = P_a A_a$ is the total asperity contact load, $A_a$ is the apparent contact area, and $\mu_f$ is friction coefficient under lubricated contact (boundary lubrication). In numerical practice, $W_a$ is calculated by [39], [56]

$$W_a = \int_{-B/2}^{B/2} P_a dx, \tag{3.24}$$

where B is the ring axial thickness.

Total friction force between the piston ring and the cylinder liner is

$$F_f = F_h + F_a \tag{3.25}$$

## 3.2 Results and Discussions

In the present study, main objective is to solve a second order non-liner elliptic equation (3.1) or (3.17). Hydrodynamic pressure $p$ and film thickness $h$ are unknowns. $h$ is mainly determined by the geometry of ring running surfaces. Here a simple parabolic profile is assumed to represent a typical worn piston ring. Figure 3.3 depicts a conjunction between piston ring and cylinder liner.

Piston ring lubrication prediction is based on the following relevant engine parameters in Table 3.1. These parameters represent a typical small bore internal combustion engine.

Both pressure and velocity boundary conditions should be specified to construct this well-defined lubrication boundary value problem. Pressure boundary

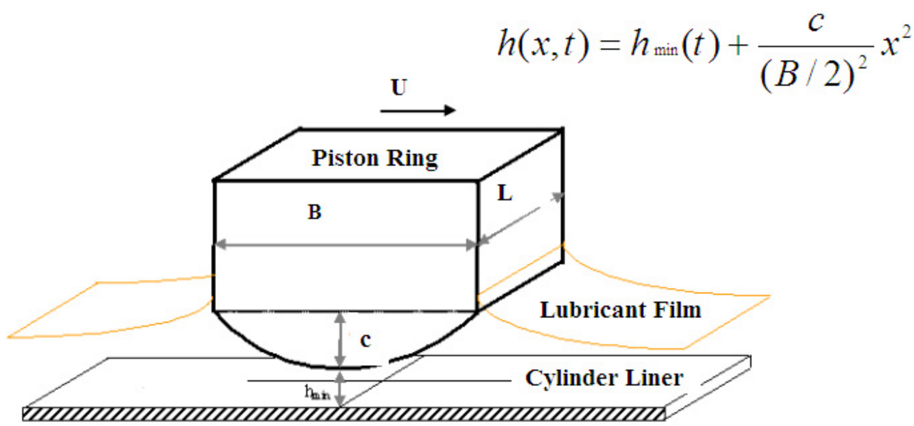


Figure 3.3: Piston ring and cylinder liner conjunction

condition depends on the combustion chamber gas pressure, and the piston ring speed is assumed to be identical with the piston velocity $U$.

Figure 3.4 shows a typical measured engine-motoring gas pressure versus crank angle inside the combustion chamber and serves as boundary pressure. Note that crank angle serves as a spatial and temporal variable.

The velocity boundary is equivalent to the instantaneous piston velocity U given by [60]

$$U = \frac{\omega S}{2}\{\sin\theta + \frac{S}{4L}\frac{\sin 2\theta}{\sqrt{(1-(S/2L)^2(\sin\theta)^2)}}\}. \tag{3.26}$$

Equation (3.25) kinematically relates piston linear velocity $U$ to crankshaft rotational speed $\omega$. S and L represent piston stroke and connecting rod length, and $\theta$ is crank angle. Figure 3.5 shows a corresponding piston velocity plot under 2000 rpm crank shaft speed.

Figure 3.6 shows the minimum film thickness $h_{min}$ for the top compression ring versus crank angle. The lowest minimum film thickness occurs in the vicinity

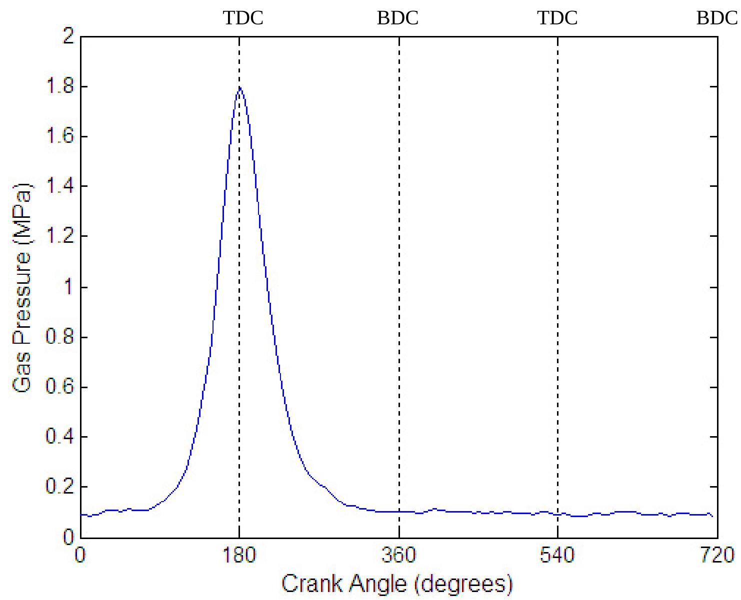


Figure 3.4: Engine combustion chamber gas pressure

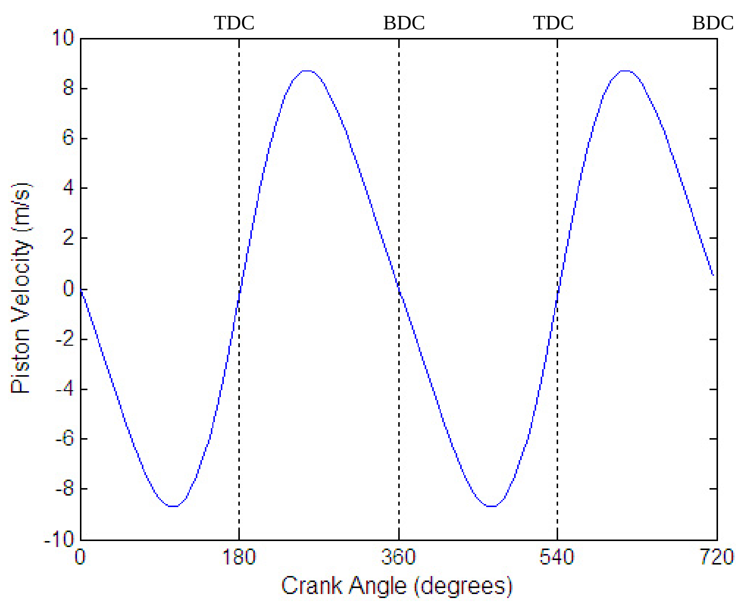


Figure 3.5: Piston velocity with 2000 rpm engine crank shaft speed

| Engine Parameters | Dimension | Unit |
|---|---|---|
| Bore Diameter D | 88.9 m | $mm$ |
| Half Stroke S/2 | 40.0 | $mm$ |
| Rod Length L | 141.9 | $mm$ |
| Composite Roughness $\sigma$ | 0.2,0.4,0.6 | $\mu$ m |
| Absolute Viscosity $\eta$ | 0.00689 | $Pa.s$ |
| Engine Speed N | 1000,2000,4000 | $rpm$ |
| Ring Height B | 0.983,1.475,2.213 | $mm$ |
| Ring Width W | 2.950 | $mm$ |
| Ring Crown Height c | 5,10,15 | $\mu\ m$ |
| Ring offset O | 0.0 | $mm$ |
| Ring Tension T | 11.19,22.38,33.57 | $N$ |

Table 3.1: Engine and ring data for lubrication analysis

of the dead centers which corresponds to crank angles of 0, 180, 360, and 540 degrees. This prediction agrees with the wear pattern observed on the cylinder-liner interface, which show high wear at top and bottom of the piston stroke, as illustrated in Figure 3.7. The highest minimum film thickness occurs at the maximum piston speed regions, where the maximum hydrodynamic action is attained.

A constant friction coefficient 0.05 was assumed to estimate the ring-liner friction force, when the predicted minimum film thickness was less than the ring-liner surface composite roughness, and contact between surface asperities occurred. Figures 3.8 and 3.9 show the corresponding ring-liner friction force and power loss plot, respectively.

The friction force for the partially lubricated area is much higher than the fully-hydrodynamic lubricated area as shown by the large spike about 180 degrees in Figure 3.8. The power loss plot shows spikes near the top dead center of the expansion stroke. The values of these spikes are relatively small due to the slow piston reciprocating speed.

The following section includes predictions by the present hydrodynamic lubri-

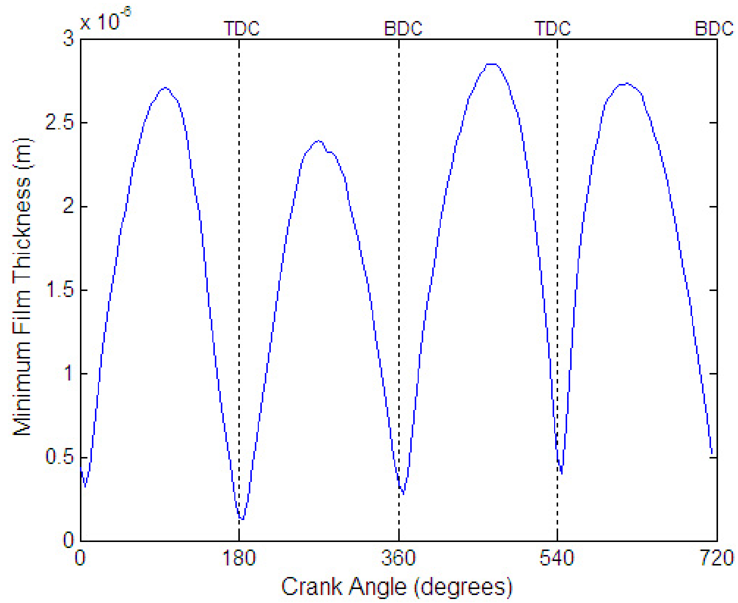


Figure 3.6: Compression ring minimum film thickness by hydrodynamic model

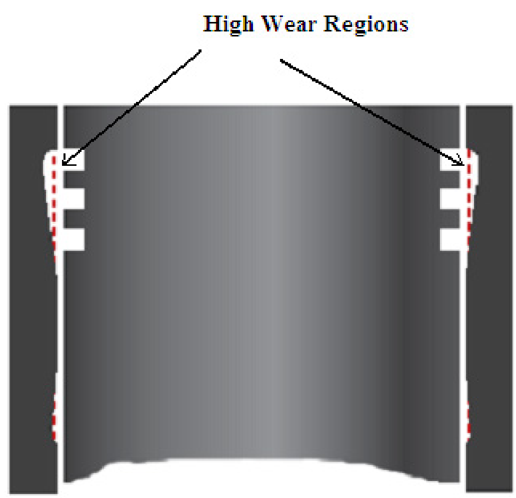


Figure 3.7: Cylinder liner wear pattern

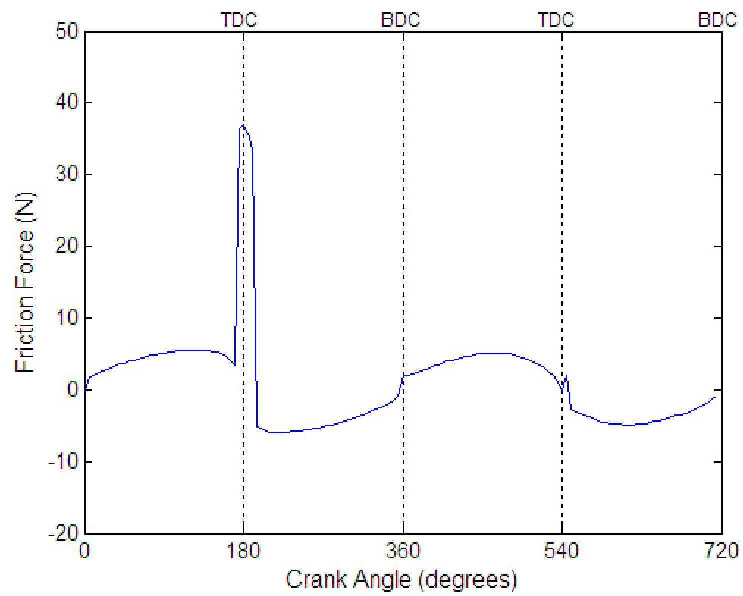


Figure 3.8: Compression ring friction force by hydrodynamic model

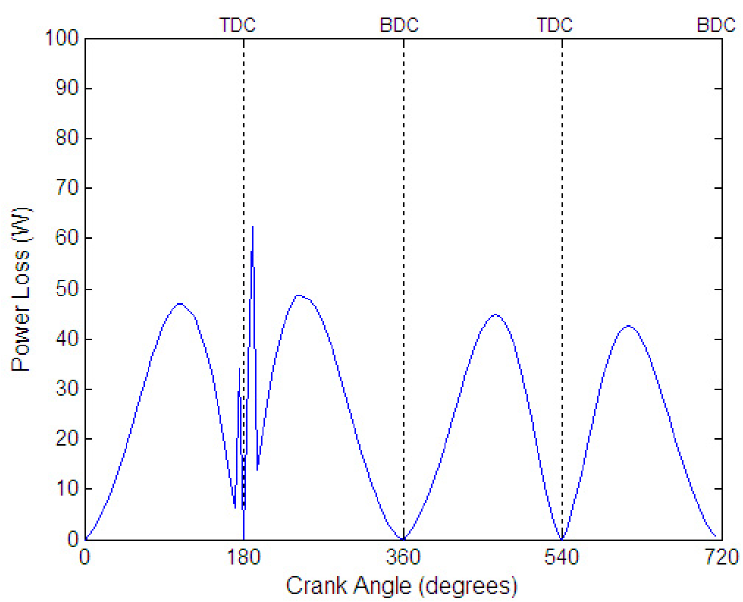


Figure 3.9: Compression ring power loss by hydrodynamic model

cation model. The objective is to demonstrate the model capability and to conduct a complete parameter study to reduce piston ring friction.

### 3.2.1 Effects of Ring and Liner Geometries

The ring-liner surface interactive action is analogous to a slider bearing. Many analytical tools developed explain the ring/liner geometry effect on the piston ring friction [61].

#### Effect of Ring Height

Figures 3.10 and 3.11 plot minimum film thickness and power loss versus crank angle with ring axial height $B$ a curve parameter. Figures 3.10 and 3.11 suggest that a larger ring height has more bearing area for hydrodynamic action and increased viscous shear loss. Reducing compression ring thickness can very effectively reduce ring friction, although the ring requires high strength and thermally-stable ring material [61].

#### Effect of Ring Crown Height

Figures 3.12 and 3.13 plot minimum film thickness and power loss versus crank angle. Here ring crown height c is a curve parameter. Figures 3.12 and 3.13 suggest that high crown ring design provides little benefits. A low crown height of $\mu$ m gives zero boundary lubrication. The ring barrel shape is critical to achieve a low friction ring design.

#### Effect of Ring Tension

A good ring tension design combines appropriate ring free shape, end gap, cylinder bore, and elasticity modulus. Ring tension is vital towards forming a seal. Ring tension controls the initial radial pressure of the ring on the cylinder, and maintains

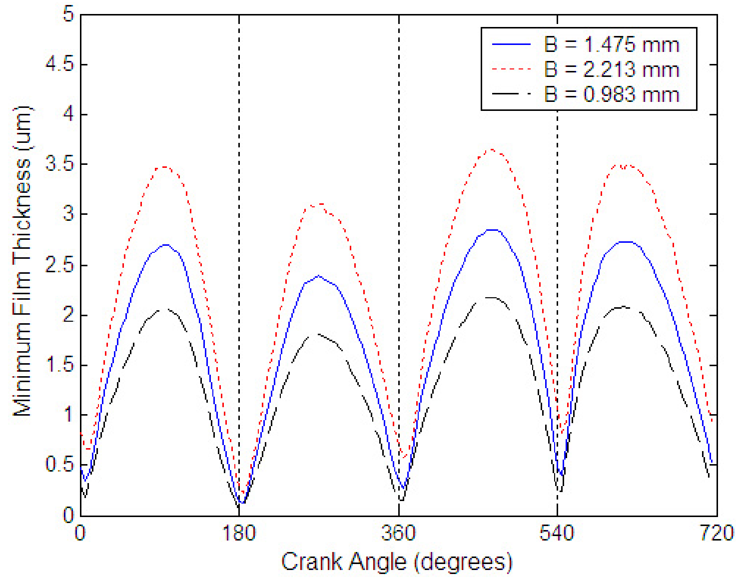


Figure 3.10: Minimum film thickness for different ring heights

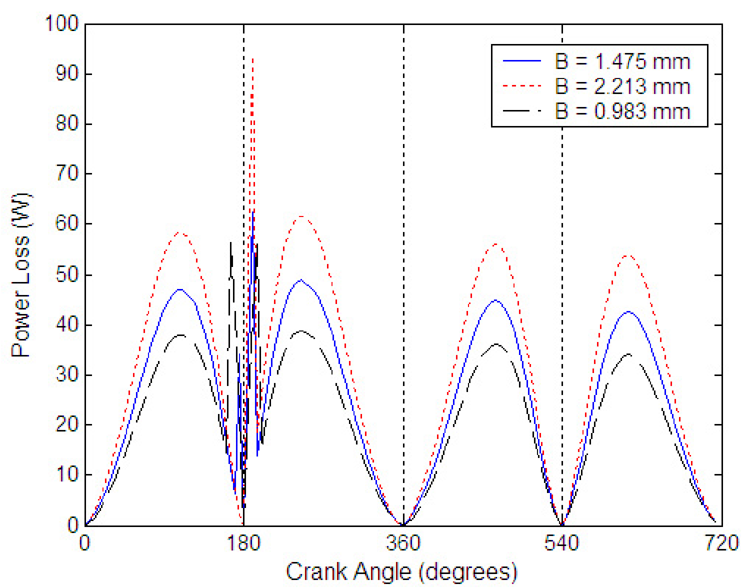


Figure 3.11: Power loss for different ring heights

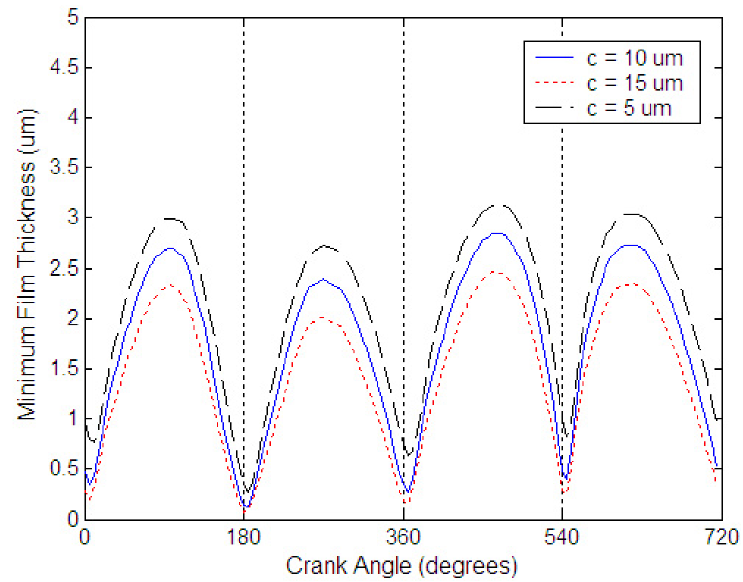


Figure 3.12: Minimum film thickness for different ring crown heights

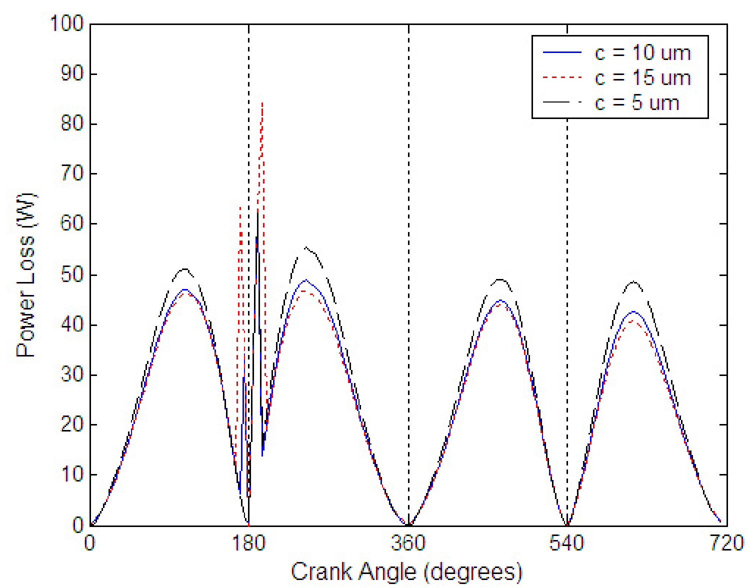


Figure 3.13: Power loss for different ring crown heights

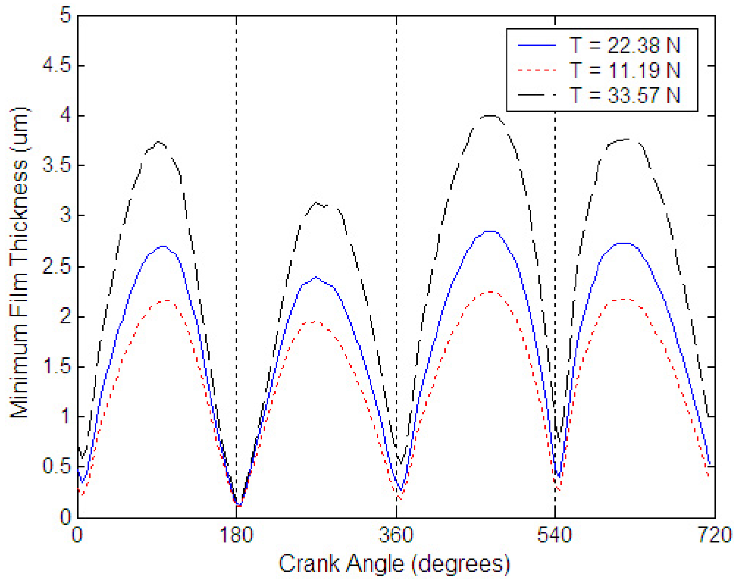


Figure 3.14: Minimum film thickness for different ring tension loads

the radial pressure on the cylinder throughout the life of the ring. For compression rings in small bore internal combustion engines, the ring tension ranges from 5 to 20 pounds [25].

Figures 3.14 and 3.15 plot minimum film thickness and power loss versus crank angle, with ring tension T a curve parameter. Figures 3.14 and 3.15 show that high ring tension can introduce high friction loss during the middle stroke. Smaller tension (pre-load) oil rings can minimize the ring-liner friction.

**Effect of Ring and Liner Surface Roughness**

Surface roughness affects the ring-liner tribology. Accepted manufacturing practices for cylinder liners [25] prescribe a plateau honing of the cylinder liner with a coarse-grained honing stone (made of diamond or ceramic) which produces a rough surface structure. The upper asperities are then removed using a fine-grained ceramic hon-

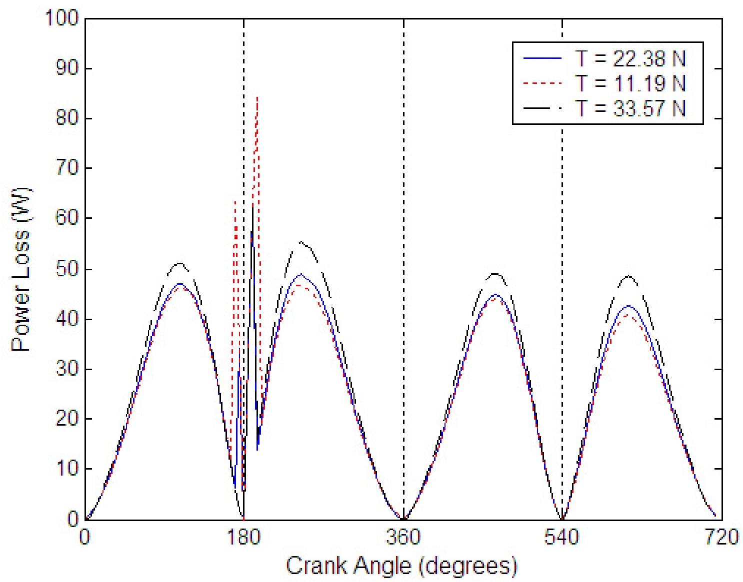


Figure 3.15: Power loss for different ring tension loads

ing stone. The liner surface roughness (with a proper honing process treatment) is about 0.1-0.4 $\mu$ m [25].

Figure 3.16 calculated by the methods documented earlier, plots power loss versus crank angle, with composite surface roughness $\sigma$ a curve parameter. Figure 3.16 suggests that a smooth liner surface has low friction power loss.

### 3.2.2 Effect of Engine Operational Conditions

As the automotive industry continuously pursues high speed and small platform engines, the piston assembly surrounding environment becomes more hostile, and friction losses increase significantly.

Figures 3.17 and 3.18 plot minimum film thickness and power loss verse crank angle. Engine speed is a curve parameter. Figures 3.17 and 3.18 illustrate that high engine speed/load promote hydrodynamic action but increase the viscous friction

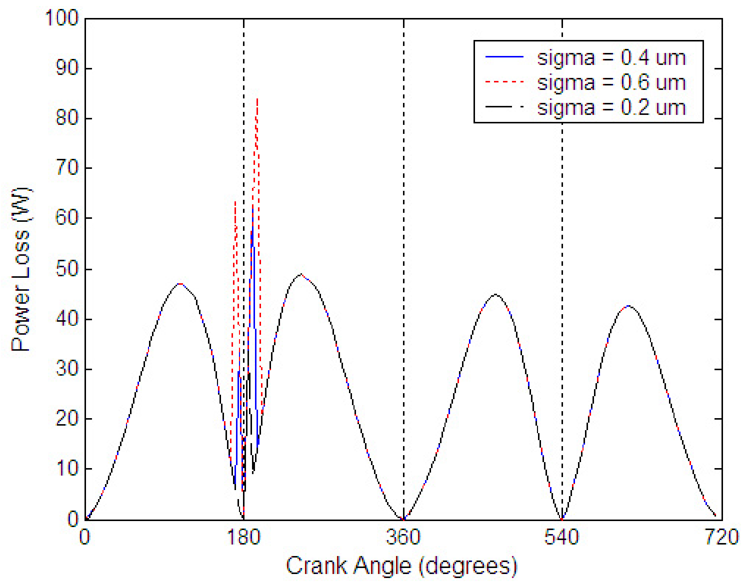


Figure 3.16: Power loss for different composite surface roughnesses

and power loss.

### 3.2.3 Effect of Ring Elasticity

A successful piston ring design must

- Conform to the cylinder bore
- Exert a uniform pressure all around on the cylinder wall
- Withstand stress resulting from installation and engine operation
- Maintain low wear

Figure 3.19 plots minimum film thickness verse crank angle. Here the minimum film thickness evaluated by EHL theory is only slightly larger than from the hydrodynamic model. Although EHL results are more realistic, numerical complications make friction force difficult to predict.

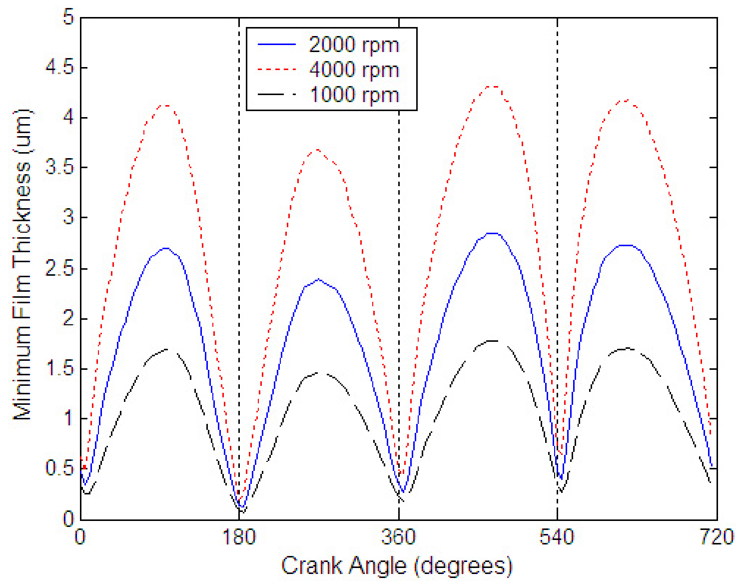


Figure 3.17: Minimum film thickness for different engine speeds

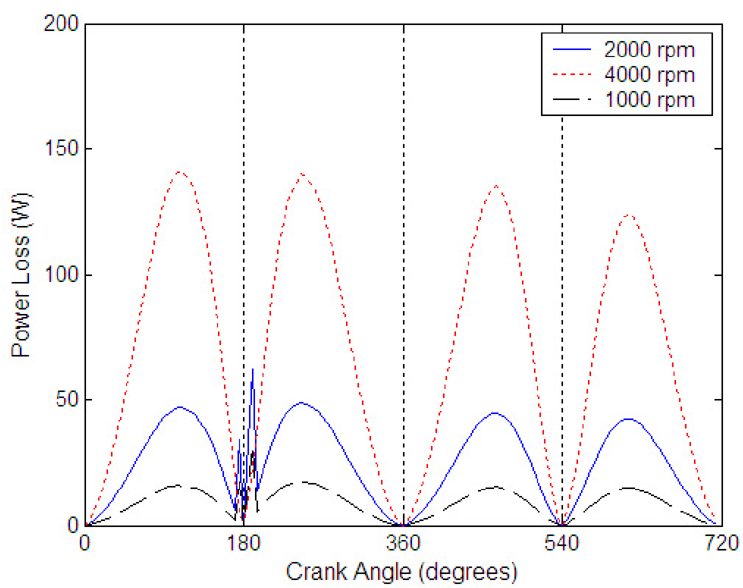


Figure 3.18: Power loss for different engine speeds

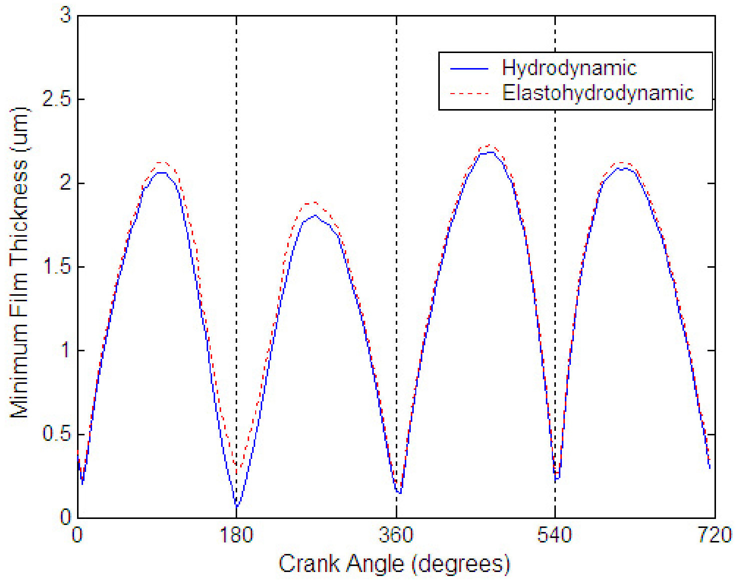


Figure 3.19: Minimum film thickness for different lubrication models

### 3.2.4 Effect of Lubricated Contact

An asperity model incorporating partial/mixed lubrication theory was integrated into the hydrodynamic lubrication analysis after the early 80s. During the piston middle stroke, the piston ring pack functions in the full-film hydrodynamic region. In the vicinity of the piston-travel reversal points (TDC, BDC), the hydrodynamic lubricant film ruptures since the low sliding velocities about the reversal points can't sustain a film. This encourages surface contact with wear on both ring and liner.

Patir and Cheng's average Reynolds equation is widely accepted for the partial/mixed lubrication analysis. Besides the surface peak-to-valley height, the surface roughness orientation, included via flow factors, influences hydrodynamic pressure by promoting or impeding flow of lubricant. The influence of flow factor, surface structure, and other factors are included in the ring-liner mixed lubrication model.

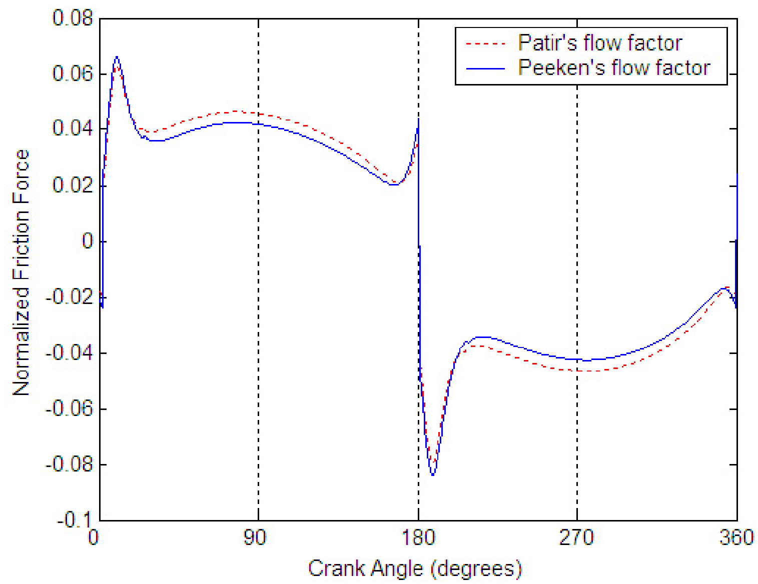


Figure 3.20: Normalized friction force for different flow factors

A test at Purdue University with a reciprocating cylinder liner and a stationary piston ring eliminates many complicating factors, such as ring motion, inter-ring gas pressure, and combustion heat. Data from this test rig can validate the present mixed lubrication model [57] [58].

**Effect of Flow Factor**

Patir and Cheng's flow factor does not involve surface contact and deformation; this omission creates significant errors at very narrow surface gaps [62]. Peeken et al [55] presented numerically-derived flow factors including surface contact effects, and showed that surface contact can occur when two surfaces are sufficiently close.

Figure 3.20 plots normalized friction force $\bar{F_f} = F_f/W$ versus crank angle. Figure 3.20 suggests piston rings with Peeken's flow factor experience more surface interaction in the vicinity of dead centers, since friction forces are larger.

### Effect of Surface Structure

Surface roughness orientation influences flow factors. A surface pattern parameter $\gamma$ describes the directional properties of surface roughness [63]. Let ACF(0.5) be the length at which the autocorrelation function (ACF) of a profile reduces to 50 % of its initial value. Mathematically, ACF is defined as

$$ACF(\Delta X) = \frac{ACV(\Delta X)}{{R_q}^2} \tag{3.27}$$

where $ACV(\Delta X)$ is the autocovariance function of a displacement lag $\Delta X$, and $R_q$ is rms surface roughness. The autocovariance function is written in discrete form for the surface roughness characterization

$$ACV(\Delta X = \frac{kL}{N}) = \frac{1}{N-k} \sum_{n=1}^{N-k} r_n r_{n+k} \tag{3.28}$$

where r is the roughness height, N is the number of digitized points in a profile, n denotes an individual point, and L is the total profile length.

ACF is a measure of how similar the surface texture is at a given distance from the original location. If ACF stays near 1.00 for a given amount of shift $\Delta X$, it is concluded that the texture is similar along the direction X. If ACF falls rapidly to zero along a given direction, then we conclude that the surface is different and thus uncorrelated with the original measurement location.

The surface pattern parameter $\gamma$ is defined as the ratio of autocorrelation functions along orthogonal directions X, Y across the surface:

$$\gamma = \frac{ACF(0.5X)}{ACF(0.5Y)} \tag{3.29}$$

Purely transverse, isotropic, and longitudinal roughness patterns correspond respectively to $\gamma = 0, 1$, and $\infty$. Bushan and Tonder [64] pointed out that an isotropic surface should be represented by

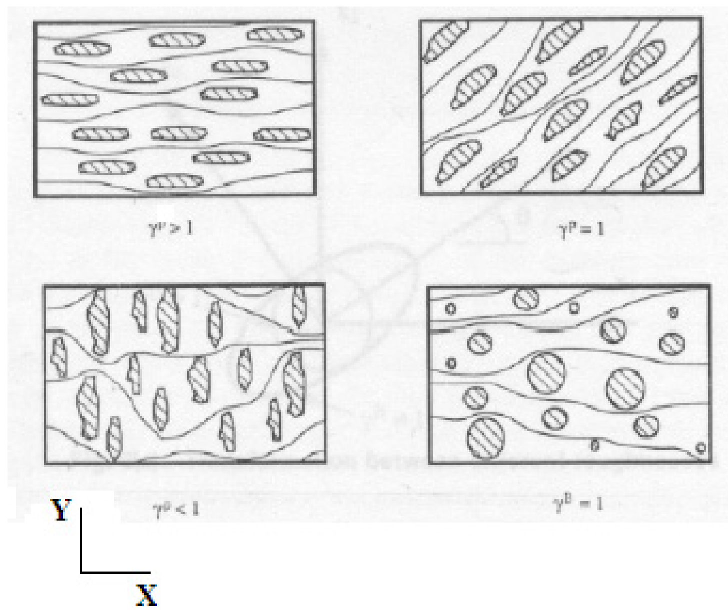


Figure 3.21: Schematic of surface contact with different roughness orientations

$$\gamma = \frac{ACF_{max}}{ACF_{min}} = 1 \tag{3.30}$$

and a surface with unidirectional striations aligned at 45 degrees to the X or Y axis has $\gamma = 1$. In equation (3.289), $ACF_{min}$ and $ACF_{max}$ represent the minimum and maximum autocorrelation function measured along any direction across the surface profile.

Figure 3.21 illustrates different surface roughness patterns [65], and gives respective $\gamma$ values.

The surface pattern parameter $\gamma$ is related to the plateau honing angle $\phi$ of the cylinder liner as

$$\gamma = \tan(90 - \frac{\phi}{2}) \tag{3.31}$$

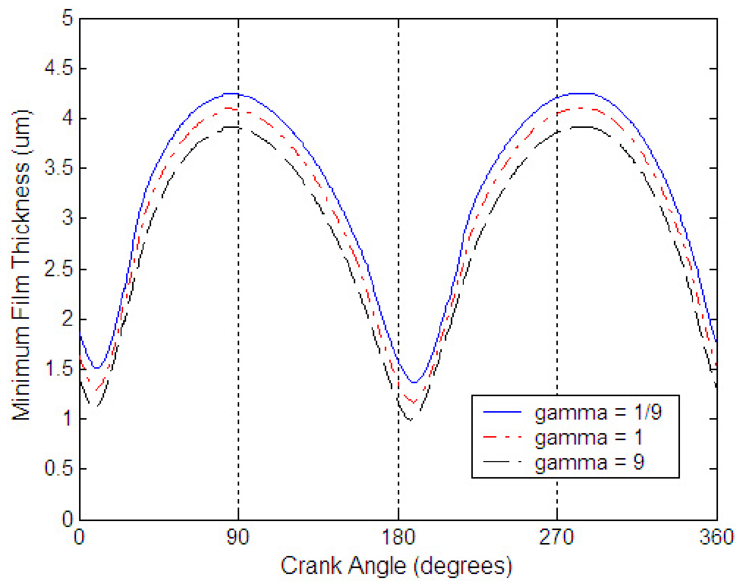


Figure 3.22: Minimum film thickness for different surface patterns

Figures 3.22 and 3.23 plot minimum film thickness and normalized friction force versus crank angle, with $\gamma$ a curve parameter. These figures illustrate the influence of surface roughness orientation on the friction characteristics between a piston ring and a cylinder liner. A smaller $\gamma$ renders a larger minimum film thickness and a smaller friction force. Figure 3.21 suggests that for $\gamma < 1$, asperities will be long and thin, with long axes oriented perpendicular to the flow. These asperity geometries would tend to constrict surface flows, which would generate higher pressures, and thicker lubricant films. This is consistent with the results in Figures 3.22 and 3.23.

Numerical results indicate that large $\gamma$ (or longitudinal roughness orientation) produces weaker hydrodynamic action, similar to Knopf's observation [34]. Increased lubricant outflow as a result of the longitudinal surface structure may be the cause.

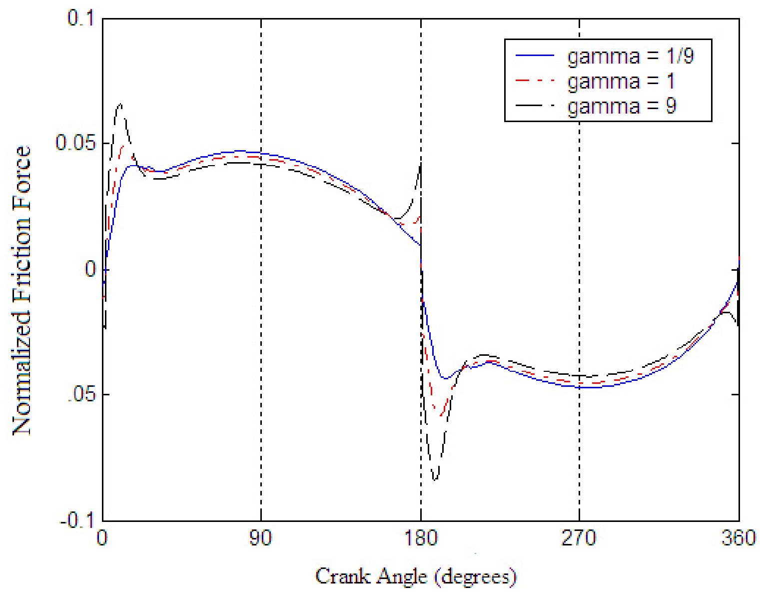


Figure 3.23: Normalized friction force for different surface patterns

### Effect of Load and Speed

Purdue's experiment can validate the new mixed lubrication model under four extreme cases:

- Case 1: Lowest speed 60 rpm and constant load 3 kgf
- Case 2: Highest speed 300 rpm and constant load 3 kgf
- Case 3: Lowest load 2 kgf and constant speed 120 rpm
- Case 4: Highest Load 8 kgf and constant speed 120 rpm

Figures 3.24, 3.25, 3.25, and 3.25 plot model predicted normalized friction force and corresponding measured normalized friction force versus crank angle for Case 1 to 4, respectively.

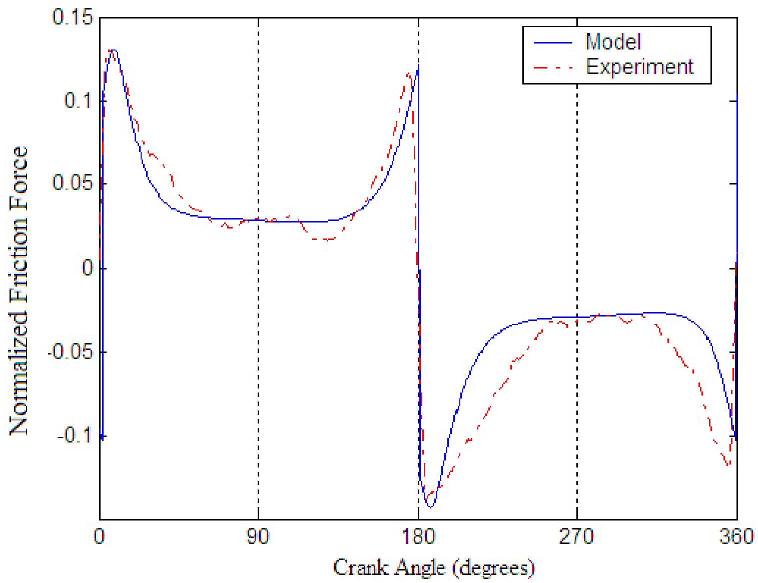


Figure 3.24: Normalized friction force for Case 1

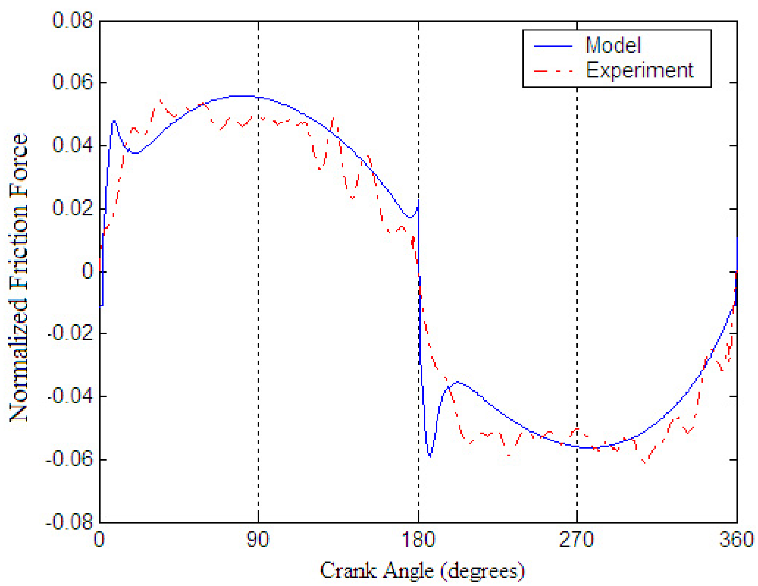


Figure 3.25: Normalized friction force for Case 2

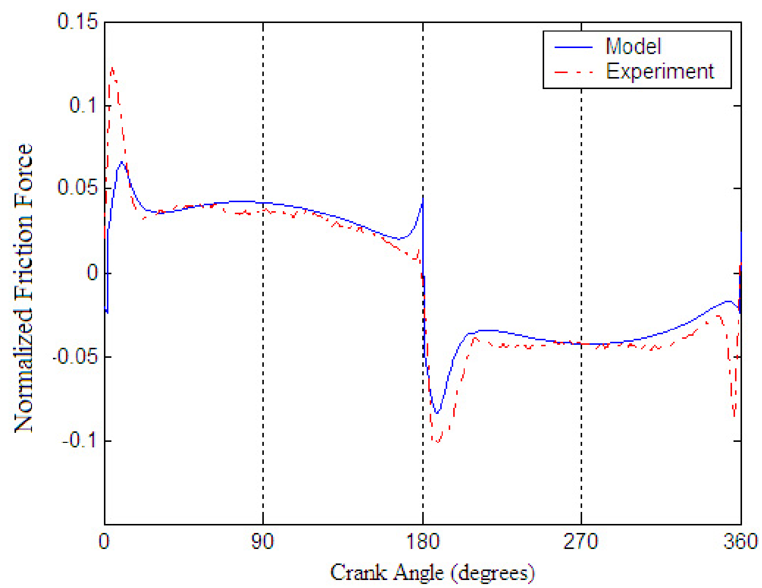


Figure 3.26: Normalized friction force for Case 3

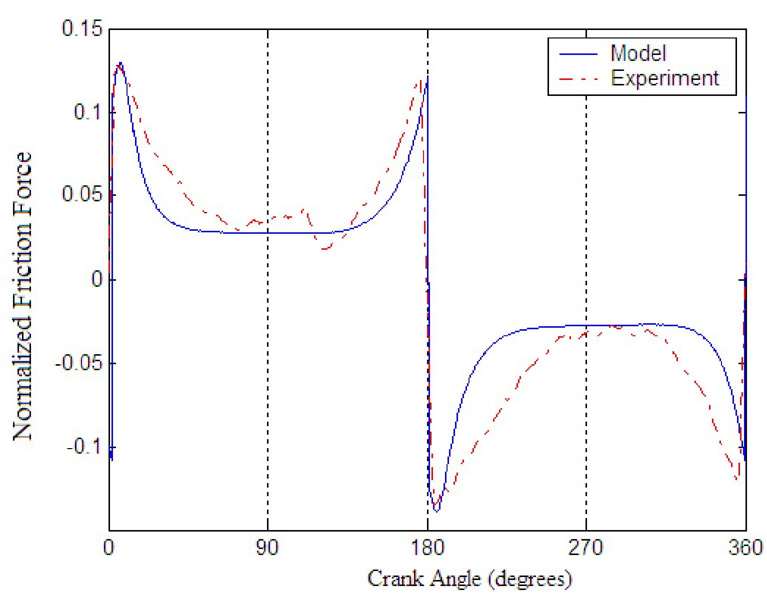


Figure 3.27: Normalized friction force for Case 4

In figures 3.24 to 3.27, the normalized friction force from both model and experiment agree reasonably well during the entire piston stroke. Greenwood's asperity model appears to capture the essential behavior of the ring-liner surface contact. More simulations studied the effects of load/speed variation on the piston ring-cylinder liner friction. Those load/speed selections matched real piston ring performance under under different engine operating conditions.

Figures 3.28 and 3.29 plot minimum film thickness and normalized friction force versus crank angle, with normal load a curve parameter. As expected, film thickness monotonically decreases with increased normal load. Normalized friction force exhibit irregular trends, but near dead centers is largest for larger normal load.

Figures 3.30 and 3.31 plot minimum film thickness and normalized friction force versus crank angle with crank shaft speed a curve parameter. At higher sliding speed, the film becomes thicker (figure 3.30). Friction is highest at dead centers, and maximizes at lowest speeds (figure 3.31).

Collectively, these numerical results suggest the present mixed lubrication model can capture hydrodynamic, mixed, and boundary lubrication regimes during the course of a piston stroke, and mixed and boundary lubrication occur near the dead centers while hydrodynamic action prevails near mid-stroke.

## 3.3 Summary

Three different piston ring lubrication models were introduced in this chapter. Unlike the classical line contact EHL piston ring model, a new soft Elastodhydrodynamic model was developed to study ring-liner lubrication; the minimum film thickness prediction agrees with prior research of others. A new rigorous mixed lubrication model for piston rings based on modern mixed lubrication theory was proposed, and numerically validated against experiments.

A parametric study confirmed that those analytical models can serve as a

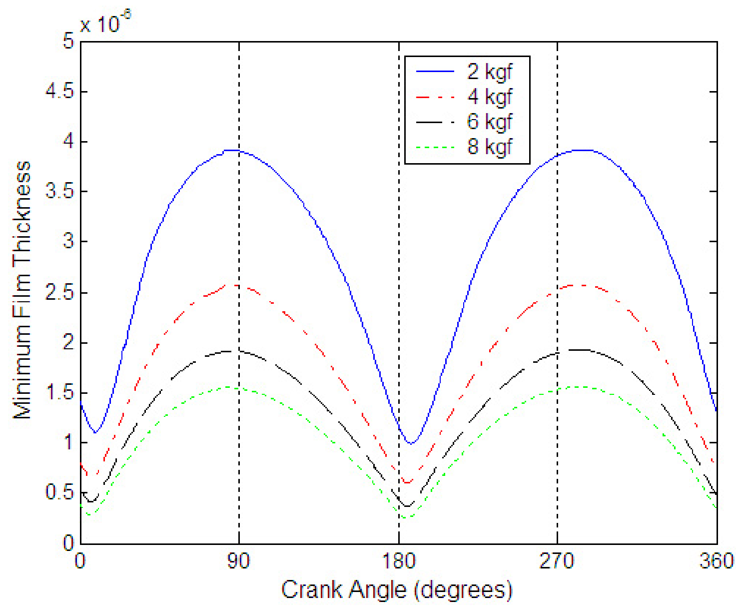


Figure 3.28: Minimum film thickness for different normal loads

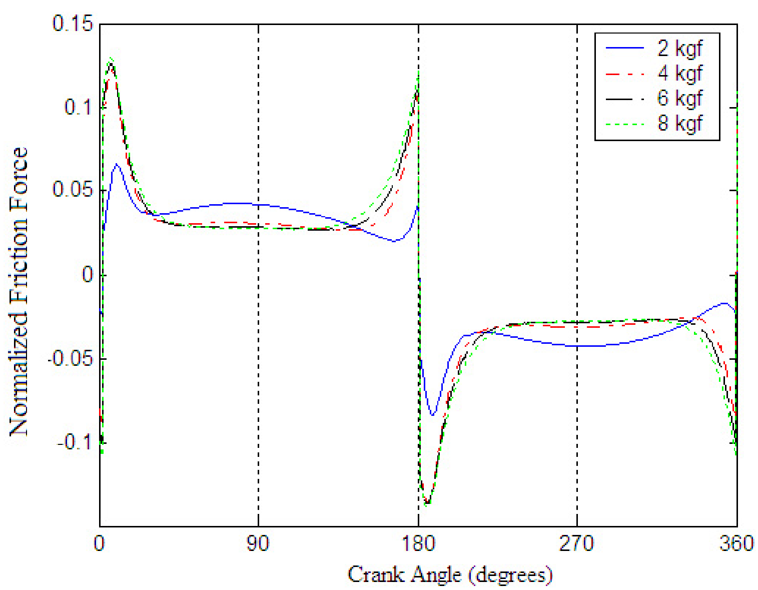


Figure 3.29: Normalized friction force for different normal loads

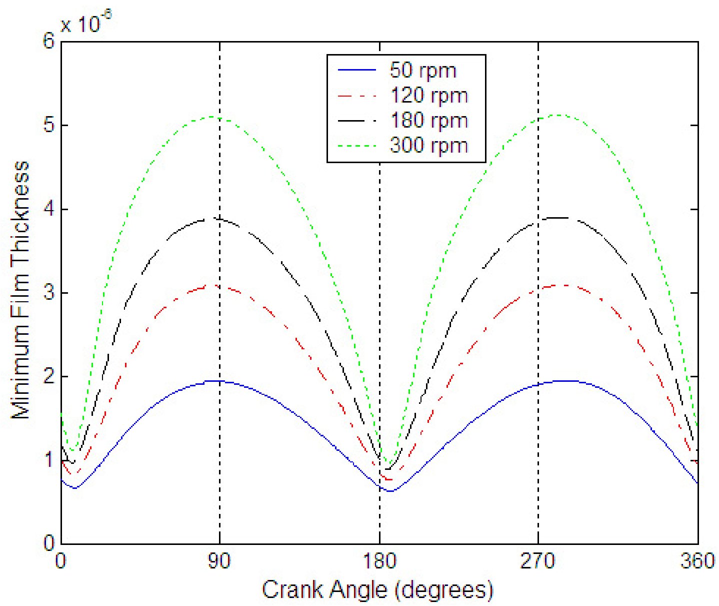


Figure 3.30: Minimum film thickness for different sliding speeds

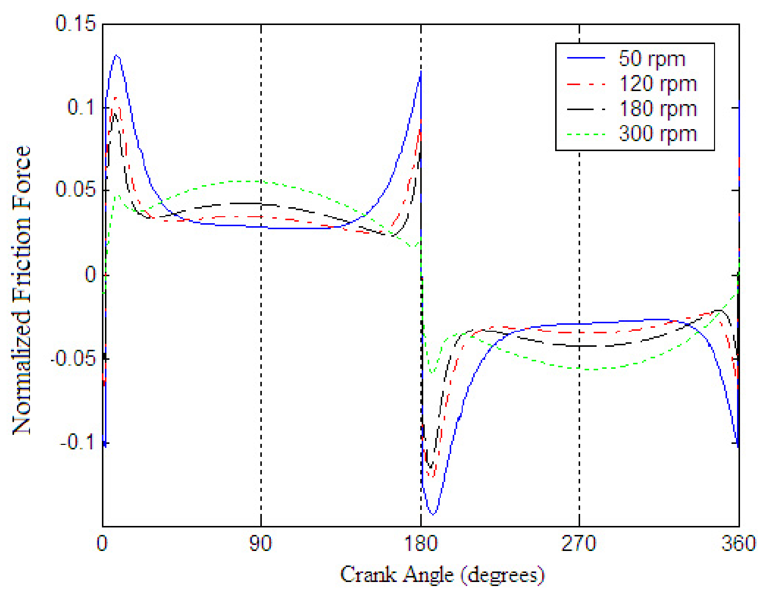


Figure 3.31: Normalized friction force for different sliding speeds

ring design guidance, such as by controlling the ring tension or axial thickness, to minimize the piston ring friction loss. Under certain circumstances, these approaches can have adverse effects, such as increasing oil consumption [66].

# Chapter 4

# Lubrication Analysis of Piston Ring Pack

A piston ring pack forms a dynamic labyrinth seal to prevent hot gases from escaping the combustion chamber. Gas pressures at the leading and trailing edge of each piston ring are constrained by the combustion chamber and the inter-ring crevice gas pressures. These pressures define the pressure boundary of Reynolds equation during a lubrication analysis.

A complete piston ring lubrication analysis requires an inter-ring gas flow model. Most existing lubrication models assume isentropic orifice flow of an ideal gas passing through the piston ring end gaps, with a constant discharge coefficient [13] [14] [44] [39]. In addition to the flow path of piston ring end gaps, gas also flows through the side-clearance between piston ring and flank groove [67] [68] [69] [70] [71]. The gas blow-by and blow-back rates predicted from the orifice model are smaller than measurements of the unburned hydrocarbon (UHC) emissions associated with the top land crevice volume, and the inter-ring crevice volume [69].

The unburned gaseous fuel trapped in the crevice regions constitutes a major source of UHC emissions in the spark ignition engine [67]. Design of a piston ring pack, with better sealing and minimal UHC emissions, usually compromises between gas blow-by and piston ring friction loss. Namazian and Heywood's early ring-motion and gas-flow integrated model examined the flow of unburned fuel into the piston-liner crevice and out of the combustion chamber. Kuo and coworkers extended Namazian's work and incorporated a ring friction model into the crevice-flow analysis; boundary lubrication was also included [68] [29]. One shortcoming of integrated models, including Roberts' work [71], is that the piston ring friction force was computed by an empirical equation before the ring motion analysis module was invoked. Dursunkaya et. al [72] and Tian et. al [73] eliminated those shortcomings using an isothermal compressible flow through the ring side-clearance, similar to Namazian.

In the present study, a temperature gradient along the radial to the piston assembly induces a quasi-Rayleigh narrow-channel gas flow. While the ratio of ring radial width to the side-clearance between piston ring and flank groove is usually around 100, the combustion gas must pass through a long channel to reach the regions behind the rings. Also the mass flow rate can be significantly affected by the surrounding thermal condition. Here a new rigorous mixed lubrication model [58] will estimate the ring-liner friction force.

## 4.1 Inter-ring Gas Flow Model

Figure 4.1 depicts a piston ring pack region in an axi-symmetric combustion chamber. The variation of chamber pressure causes gases to flow into and out of the inter-ring crevice region. A typical piston ring pack assembly of two compression rings (top and middle) and one oil ring (bottom) generates seven regions (labelled 1 to 7) based on the gas pressure variation, see Figure 4.1.

The gas pressure is assumed uniform within each region. In the top-land crevice Region 1, gas flow is assumed to be a fully developed laminar flow. Since

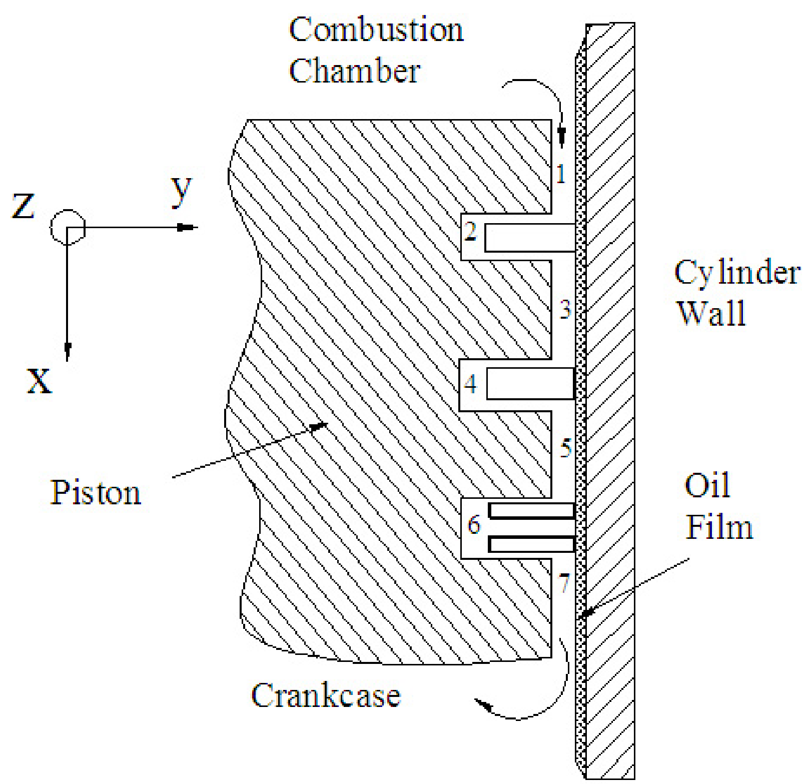


Figure 4.1: Piston Ring Pack Assembly and Crevice Regions

the pressure drop is assumed negligible, the gas pressure is almost equal to the combustion chamber pressure. Region 7 is assumed at ambient pressure. Gas can penetrate the piston ring end gap during the entire engine stroke. Flow through the ring-side clearance depends on the dynamic equilibrium position of the piston ring. During the compression stroke, the top compression ring sits on the groove surface and blocks gas flow from Region 2 to 3. The piston ring friction forces help to position the ring relative to the piston flank groove.

Gas flow through each of the crevice regions must obey fundamental fluid and thermodynamic laws. A gas flow model was established with the following assumptions:

- Each crevice region i has a uniform pressure $p_i$. Pressure $p_1$ for Region 1 is at the chamber combustion pressure, and pressure $p_7$ for Region 7 is at the crankcase pressure;
- Each crevice region has constant volume $V_i$;
- The chemical composition of the gas does not change;
- Flows are laminar through the ring end gap and the ring side-clearance but isentropic and Rayleigh flow, respectively.

Assuming a perfect gas law with gas constant $R$, the continuity equations in crevice regions 2 to 6 are

$$\frac{dp_2}{dt} = \frac{RT_2}{V_2}(\dot{m_{12}} - \dot{m_{23}}) \tag{4.1}$$

$$\frac{dp_4}{dt} = \frac{RT_4}{V_4}(\dot{m_{34}} - \dot{m_{45}}) \tag{4.2}$$

$$\frac{dp_6}{dt} = \frac{RT_6}{V_6}(\dot{m_{56}} - \dot{m_{67}}) \tag{4.3}$$

$$\frac{dp_3}{dt} = \frac{RT_3}{V_3}(\dot{m_{13}} + \dot{m_{23}} - \dot{m_{34}} - \dot{m_{35}}) \tag{4.4}$$

$$\frac{dp_5}{dt} = \frac{RT_5}{V_5}(\dot{m_{35}} + \dot{m_{45}} - \dot{m_{56}} - \dot{m_{57}}) \tag{4.5}$$

$$\tag{4.6}$$

In equations (4.1) to (4.6), $p_i$, $T_i$ and $V_i$ are gas pressure, temperature and volume in the ith crevice regions, and $\dot{m_{ij}}$ is the gas mass flow rate from region i to region j. The pressure rate terms on the left side of equations (4.1) to (4.6) represent compressibility effects. The terms on the right side represent flows into and out of the relevant control volume. For simplicity, temperature $T_i$ and volume $V_i$ are assumed constant for each region. The gas passing through the ring end gap flow such as from the crevice region 1 to 3, 3 to 5, and 5 to 7 can be treated as an orifice flow with the mass flow rate $\dot{m}_{ij}$ due to pressure difference $p_i - p_j$ given by [3]:

$$\dot{m}_{ij} = C_d A_g \left[\frac{2\gamma}{(\gamma-1)RT_i}\right]^{0.5} p_i \left(\frac{p_j}{p_i}\right)^{1/\gamma} \left[1 - \left(\frac{p_j}{p_i}\right)^{(\gamma-1)/\gamma}\right]^{0.5} \tag{4.7}$$

In equation (4.7), $C_d$ is the discharge coefficient, $A_g$ is the effective gap area which depends on the ring radial deformation, and Poisson constant $\gamma$ is set at 1.3. For choked flow, the mass flow rate $\dot{m}_{ij}$ maximizes and

$$\frac{p_j}{p_i} = \left(\frac{2}{\gamma+1}\right)^{\gamma/(\gamma-1)}. \tag{4.8}$$

Equation (4.7) becomes

$$\dot{m}_{ij} = 0.227 C_d A_g \left[\frac{2\gamma}{(\gamma-1)RT_i}\right]^{0.5} p_i. \tag{4.9}$$

Gas flow across the ring side clearance, usually excluded from piston ring lubrication studies [44], was recognized as an isothermal, laminar compressible flow in the UHC emission study [67] [68] [69]. Here a quasi-Rayleigh compressible flow model

$$\dot{m}_{ij} = C_f A_n \left[\frac{p_j}{RT_j}\right]^{0.5} \left[\frac{p_i - p_j}{1 - \frac{p_j T_i}{p_i T_j}}\right]^{0.5} \tag{4.10}$$

will be assumed, due to a substantial temperature gradient driving the gas flow. Details of mass flow rate calculation are given by Appendix C [74]. In equation (4.10) $C_f$ is the frictional loss coefficient for the flow and $A_n$ measures the area normal to the flow. The mass flow rate depends on $A_n$ and the side-clearance h. $A_n$ is related to the ring axial position. Early lubrication studies [39] [13] [3] excluded axial motion of the piston ring. In the present study, piston rings can move within the piston groove flanks, to create a dual gas flow passage such as from the crevice region 1 to 2, 2 to 3, 3 to 4, 4 to 5, 5 to 6, and 6 to 7.

Inter-ring gas pressure was investigated numerically and experimentally [75] [76]. Crevice gas pressure and ring motion were predicted. Some calibration proved necessary, such as the discharge coefficient. The ultimate goal is a more realistic predictive model, with minimal experimental effort.

## 4.2 Piston Ring Axial-Motion Model

Furuhama studied piston ring motion, and influence on piston ring tribology [77]. Four major forces act on the piston ring along the piston reciprocating direction: gas pressure force $F_p$, friction force between piston ring and cylinder liner $F_f$, gravitational force $F_g$, and the supporting force between groove flank and upper/lower ring surface $F_s$. Figure 4.2 depicts a free-body diagram of the piston ring. Here $A_t$ and $A_p$ are areas beneath ring, and without film.

The net gas pressure force $F_p$ is estimated by the difference between the upper $p_U$ and lower $p_L$ ring surface pressures [71]:

$$F_p = (p_L - p_U)A_p + (\delta L\frac{p_B + p_U}{2} - \delta U\frac{p_B + p_L}{2})(A_t - A_p) \tag{4.11}$$

In equation (4.11), $p_U$ and $p_L$ are the gas pressures on the upper and lower ring surfaces, $p_B$ is the gas pressure behind the ring, and $\delta U$ and $\delta L$ are switch functions which become zero when a squeeze film exists between the ring and the groove flank. Normally, area $A_p$ not under the film is only about 15 % of area $A_t$ under the ring.

A resistance load due to a squeeze film between ring and groove flank was first suggested by Furuhama [77]. Depending on the ring motion condition, this load obstructs direct contact between the ring and the groove surface. This load is given

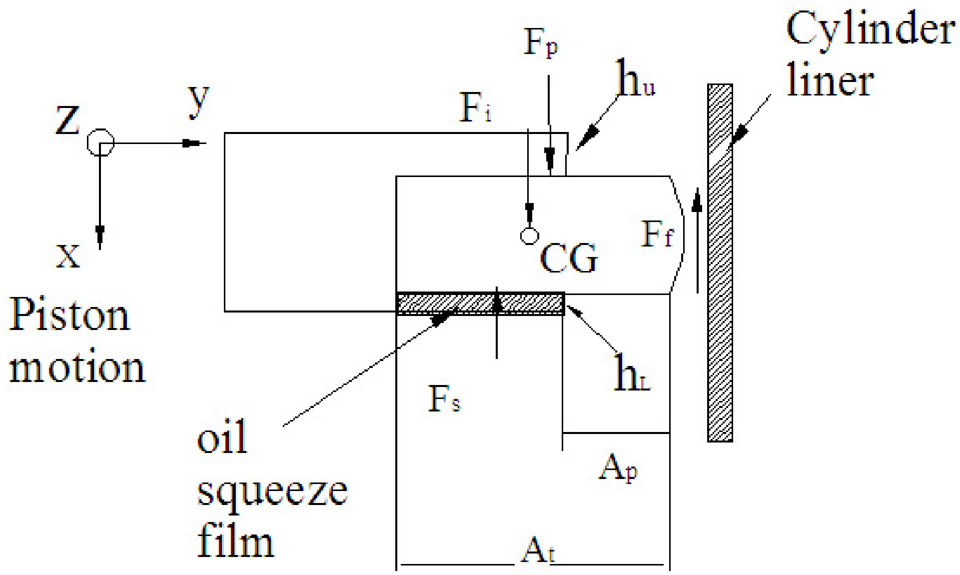


Figure 4.2: Forces acting on a single piston ring

by

$$F_s = -\beta \mu_{oil} L_r \frac{dh}{dt} \left( \frac{W_r}{h} \right)^3 \tag{4.12}$$

Here h is the ring side-clearance (either $h_U$ or $h_L$ ), $L_r$ is the ring length along the circumferential direction, $W_r$ is the ring width in the radial direction, and $\mu_{oil}$ is the oil viscosity. Values used in this work were taken from Kuo and co-workers [68].

Early gas blow-by studies [67] [68] [71] assumed the friction force between the piston ring and the cylinder liner given by

$$F_f = -f \pi D_r T_r (p_B + p_E), \tag{4.13}$$

where $D_r$ is the outside diameter of the ring, $T_r$ is the ring axial thickness, and $p_E$ is the ring tension pressure when the ring is initially installed [5]. The analysis dramatically simplifies when piston ring friction $F_f$ decouples from crevice gas pressure. However, Equation (4.13) gives zero friction force at TDC , since it then only involves hydrodynamic lubrication. Boundary lubrication near TDC generates significant "rubbing" force, even at zero velocity. The piston ring mixed lubrication model of the previous chapter will estimate the friction force.

From Newton's second law, ring motion $x_r = x_r(t)$ along the piston reciprocating direction x is governed by

$$m_r \frac{d^2 x_r}{dt^2} = F_p + F_s + F_f, \tag{4.14}$$

where an inertial reference frame is fixed to the stationary cylinder wall. The gravitational force is omitted since its value is small compared to other load components. Downward motion and force are positive.

With $x_r = x_p + h_r$,

$$m_r \frac{d^2 h_r}{dt^2} = F_p + F_s + F_f + F_i \tag{4.15}$$

where $x_p$ is piston displacement, $F_i = -m_r \frac{d^2 x_p}{dt^2}$ is the inertial force term related to piston motion, and $h_r$ is the piston ring motion in the $x$ direction relative to the piston. The extremes $h_r = 0$ or $h_r = 1$ represent the ring bottom or top sitting on the groove flank. Relative motion between piston ring and groove flank acts like a valve, and provides a pressure boundary.

## 4.3 Results and Discussions

To simplify numerical implementation, crankcase pressure was assumed in the inter-crevice region 5 (see Figure 4.1 ), since the oil ring provides a weaker sealing than compression rings. For gas flow, a piston ring pack was represented by two orifices and two volumes. Continuity equations (4.1), (4.2) and (4.4) describe the gas mixture flow across the piston ring pack. Those equations relating gas pressures $p_2$, $p_3$, $p_4$ can be solved numerically once the piston ring position $h_r$ is determined from the ring-motion equation (4.15) for a certain crank angle. Note that $h_r$ is needed to determine area $A_n$ in equation (4.10).

The solution procedure for equation (4.15) starts with initial guesses for $h_r$ and derivative $\frac{dh_r}{dt}$ (equal to zero, at the beginning of compression stroke). The method solved the gas flow model for gas boundary pressure, then obtained estimates for $F_p$ and $F_f$. Next, $\frac{d^2h_r}{dt^2}$ is computed from equation (4.15). At the next time step about one degree crank angle, $\frac{dh_r}{dt}$ is estimated via Euler's method, and the crevice gas pressure re-calculated.

Table 4.1 sizes piston rings, grooves, and crevice regions. Both compression rings are assumed to have parabolic shapes along their contact sides, and identical ring thicknesses.

| Parameters | Dimension | Unit |
|---|---|---|
| Ring end-gap area | 0.161 | $mm^2$ |
| Ring axial thickness | 1.48 | $mm$ |
| Ring side-clearance | 0.038 | $mm$ |
| Top ring width | 3.55 | $mm$ |
| Second ring width | 3.82 | $mm$ |
| Top ring crown height | 0.012 | $mm$ |
| Second ring crown height | 0.008 | $mm$ |
| Top-land crevice volume | 544 | $mm^3$ |
| Volume of region behind top ring | 472 | $mm^3$ |
| Volume of region between rings | 375 | $mm^3$ |
| Volume of region behind 2nd ring | 361 | $mm^3$ |
| Top ring mass | 9.83 | $g$ |
| Second ring mass | 10.75 | $g$ |

Table 4.1: Piston ring and groove specifications

Figure 4.3 plots gas pressure versus crank angle for different crevice regions. Figure 4.3 shows a typical inter-ring gas pressures $p_1, p_2, p_3$, and $p_4$ in the crevice regions 1, 2, 3, and 4, for engine speed of 2000 rpm. The inter-ring gas pressure $p_3$ is much lower than the combustion chamber pressure $p_1$. The maximum value of $p_3$ occurs at a later crank angle, due to the orifice resistance which lowers the pressure intensity and delays the pressure response.

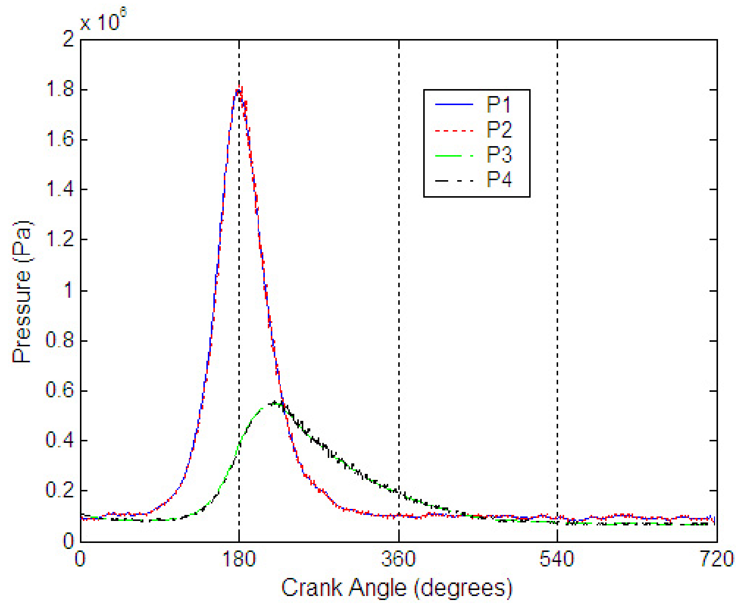


Figure 4.3: Gas pressure inside crevice regions

Figure 4.4 shows friction force $F_f$ on the top and second compression ring at 2000 rpm, calculated via the mixed lubrication model with crevice gas forming the pressure boundary conditions. The top ring has larger friction near TDC of the expansion stroke, compared with the second ring. Figure 4.5 shows a corresponding minimum film thickness profile for a crank angle between 180 and 360 degrees. The second ring has a small film thickness..

Compression ring motions $h_r$ versus crank angle in Figure 4.6 suggests that

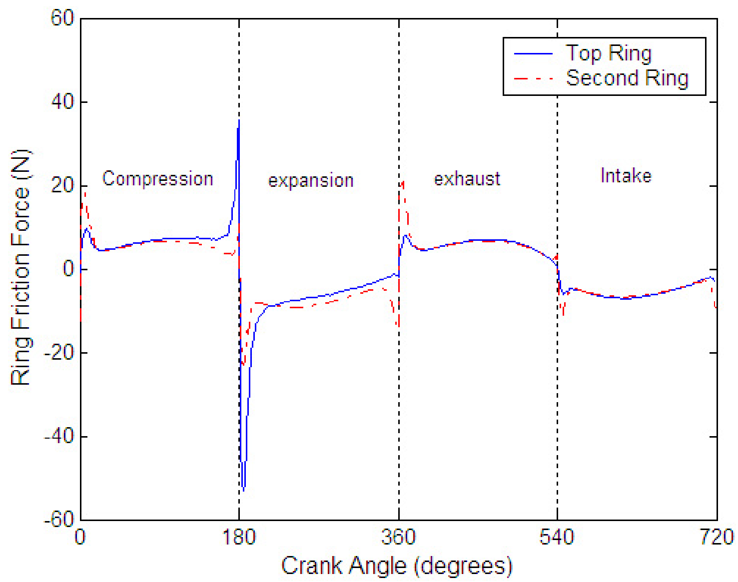


Figure 4.4: Friction force acting on top and second compression ring

the gas load is the dominant force. Recall that $h_r$ describes the vertical motion of the piston ring relative to the piston. Here the spikes in the curves near crank angle 540 degrees suggests large displacements of the ring, *i.e.*, lift off from the groove. The piston ring sits on the bottom of the groove flank, held in place by the high combustion gas pressure applied to the top of the rings during both compression stroke( 0 - 180 degree crank angle) and expansion stroke ( 180 - 360 crank angle). But from the end of the exhaust stroke to the beginning of the intake stroke, the high combustion gas pressures vanish (figure 4.3), and the rings are free to lift off. Thus, both rings could only lift off from the end of the exhaust stroke to the beginning of the intake stroke. This agrees well with experimental observation from Furuhama [77]. The gas blow-by occurs through the piston groove side-clearance when rings life off the groove. The blow-by rate is insignificant since the gas pressure is relatively low during the engine exhaust and intake strokes. A piston ring pack

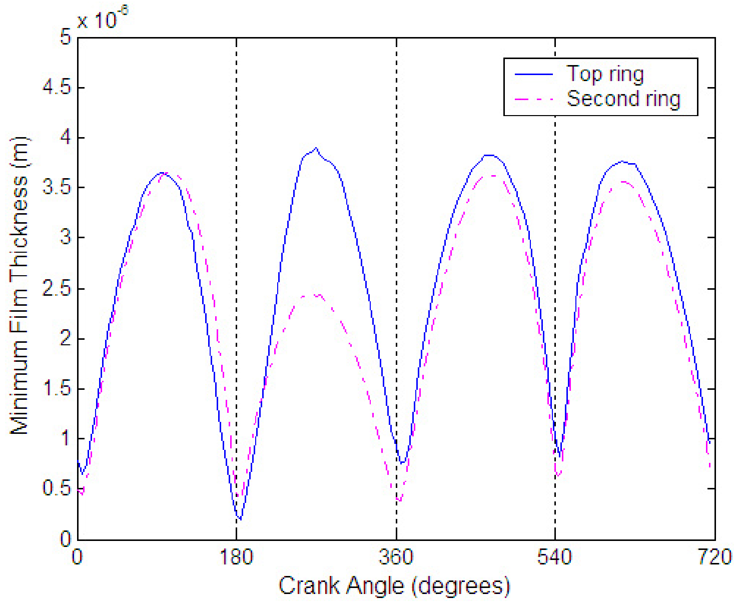


Figure 4.5: Predicted compression ring minimum film thickness

design achieve good gas sealing performance.

## 4.4 Summary

Appropriate pressure boundary conditions for a piston ring pack lubrication analysis were obtained by integration of a gas flow and a ring axial-motion model. A new narrow-channel compressible flow model was proposed and implemented. Piston ring friction force was predicted under engine-motoring condition by a new rigorous mixed lubrication model. Finally, compression ring motions were presented by solving the ring motion equations simultaneously.

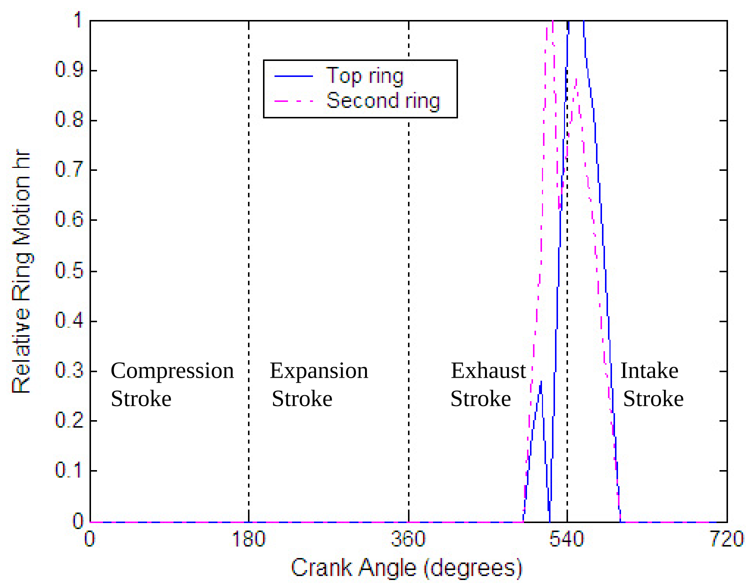


Figure 4.6: Predicted compression ring motion

# Chapter 5

# Lubrication Analysis of Piston Skirt

The piston skirt is another major source of total piston assembly friction loss. Most analytical studies in piston assembly friction have focused on ring lubrication; little has been done on skirt lubrication [27]. The piston oscillates radially (transversely) within the cylinder bore due to time-varying gas, inertial, friction, and connecting-rod forces. Secondary piston motion affects piston-liner lubrication, friction, wear, and ultimately engine performance. This secondary piston motion can generate slap between the piston and cylinder wall, from unbalanced forces and moments.

A piston skirt lubrication analysis aids understanding of piston dynamics. In the early 1980s, Li et al's automotive piston hydrodynamic lubrication model related piston skirt friction to the wrist-pin location. Okubo et al [78] obtained a piston trajectory from forces and moments caused by hydrodynamic lubrication. Later, the surface roughnesses of skirt and liner were included by Zhu and Cheng [35] [36],

Forces and moments from a piston skirt hydrodynamic model will be integrated into a piston motion equation, to form an initial value problem with a non-linear second-order differential equation. A new and fast Newton-Raphson algorithm will solve this problem numerically.

## 5.1 Hydrodynamic Lubrication Model

A piston skirt can have a converging-diverging profile formed from secondary motions, which can cause wedge actions, analogous to a slider bearing. Figure 5.1 depicts side and top views of a piston skirt. Coordinate system XYZ has origin, O', fixed at the cylinder head (top). The Z direction coincides with the cylinder axis. Coordinate system, r $\theta$ z with origin, O, fixed to the top of the piston, moves with the piston.

Piston secondary motions (both lateral and rotational) across the clearance between piston and cylinder wall depends on forces and moments on the piston body/surface, including forces generated by hydrodynamic action between the piston skirt and cylinder liner. A free body diagram of the piston system is shown in Figure 5.2.

The following assumptions were made for the piston skirt lubrication model

- The radial clearance C between piston and liner is small. This implies thin film lubrication;
- All solid parts are rigid and do not deform;
- The lubricant is a Newtonian isoviscous fluid;
- A fully-flood lubrication condition exists;
- The top and bottom skirt eccentricities $e_t$ and $e_b$ are small compared to the piston skirt length L.

For the r $\theta$ z coordinate system shown in Figure 5.1, the relevant Reynolds equation is

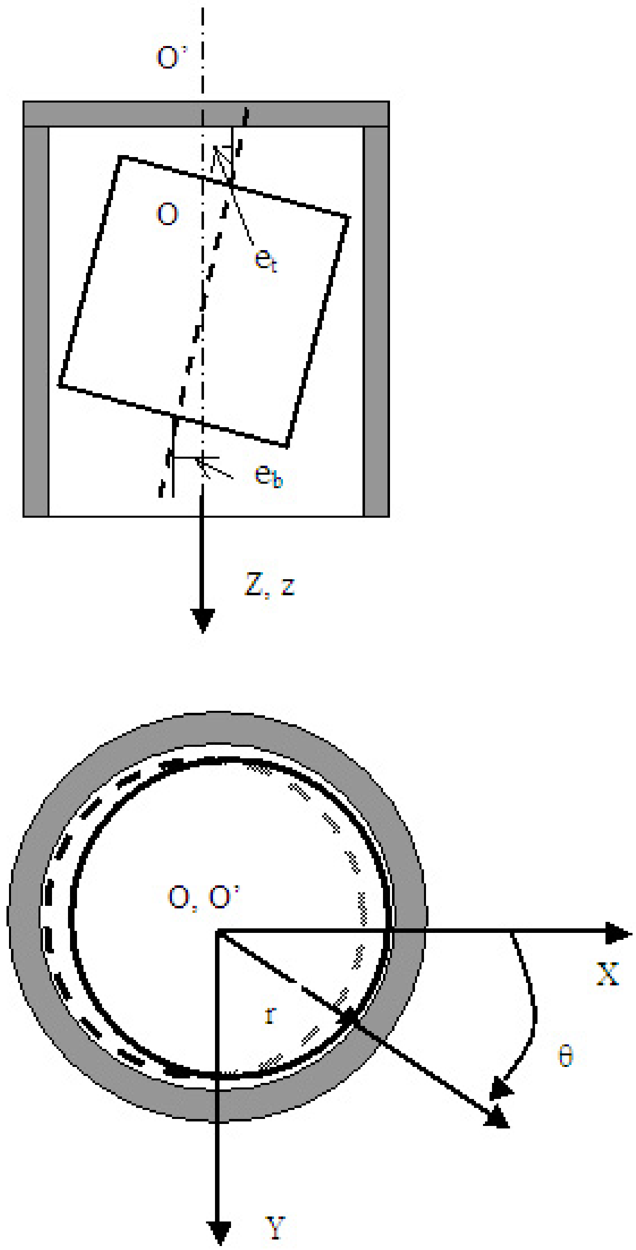


Figure 5.1: Coordinate systems employed in the piston-skirt lubrication analysis

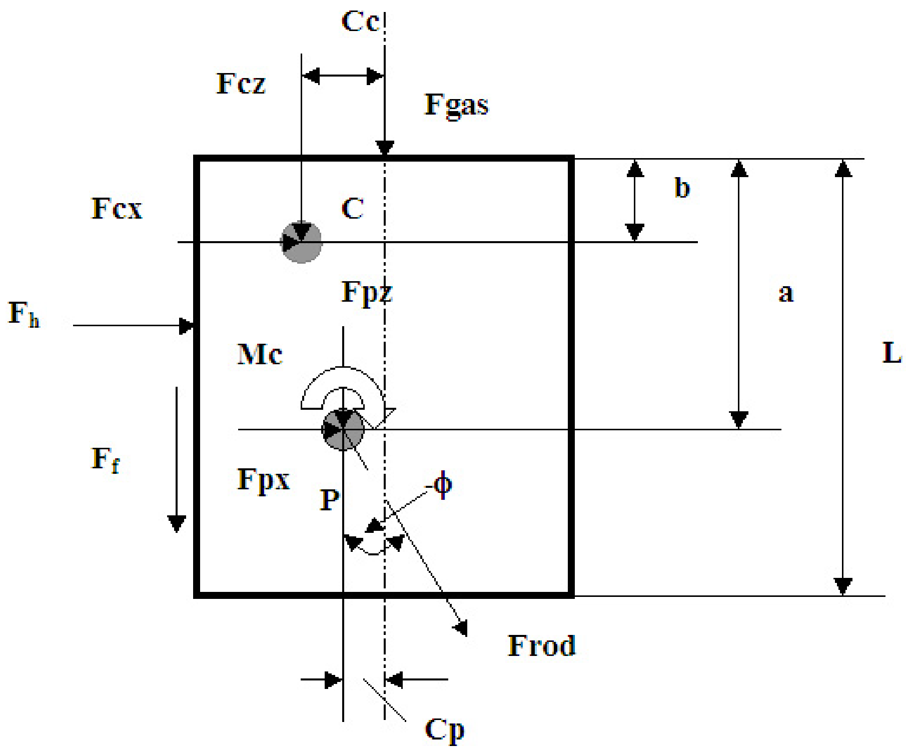


Figure 5.2: Piston free-body diagram

$$\frac{1}{R^2}\frac{\partial}{\partial\theta}(\frac{h^3}{\eta}\frac{\partial p}{\partial\theta}) + \frac{\partial}{\partial z}(\frac{h^3}{\eta}\frac{\partial p}{\partial z}) = -6U\frac{\partial h}{\partial z} + 12\frac{\partial h}{\partial t}. \tag{5.1}$$

where R is the cylinder radius and U is the piston reciprocating speed. The local film thickness is

$$h = C + (e_t + (e_b - e_t)\frac{z}{L})\cos\theta \tag{5.2}$$

depends on eccentricities $e_b$ and $e_t$ of the piston top and bottom (see Figure 5.1), the clearance C between piston and liner, and the length of the piston skirt L.

A homogenous boundary condition on the pressure is employed since both top and bottom skirt locations are at crankcase pressure. The boundary value problem (Equations (5.1) and (5.2)) was solved by the numerical approach described in Chapter 2. 40 x 40 mesh grids were employed to discretize the entire piston skirt region. After solving the hydrodynamic pressure $p = p(\theta, z)$ on the grid points, the force

$$F_h = -\int_0^L \int_0^{2\pi} p(\theta, z)R\cos\theta d\theta dz \tag{5.3}$$

and the moment

$$M_h = -\int_0^L \int_0^{2\pi} p(\theta, z)R\cos\theta(a - z)d\theta dz \tag{5.4}$$

Here $a$ locates the wrist pin relative to the top of the piston see Figure 5.2, along the cylinder axis Z.

The viscous frictional force

$$F_f = -\int_0^L \int_0^{2\pi} (\frac{h}{2}\frac{\partial p}{\partial z} + \eta\frac{U}{h})Rd\theta dz \tag{5.5}$$

and moment from viscous friction

$$M_f = -\int_0^L \int_0^{2\pi} (\frac{h}{2}\frac{\partial p}{\partial z} + \eta\frac{U}{h}) R\cos\theta R d\theta dz. \quad (5.6)$$

A set of typical piston system parameters of an engine is listed in Table 5.1. Unless stated otherwise, these parameters values were used to obtain the upcoming computational results.

| Parameters | Dimension | Unit |
|---|---|---|
| Piston mass | 0.73 | $kg$ |
| Wrist pin mass | 0.15 | kg |
| Piston moment of inertia | 0.00061 | $kg - m^2$ |
| a | 17.3 | $mm$ |
| b | 0.025 | $mm$ |
| L | 55.9 | $mm$ |
| $C_p$ | 0.152 | $mm$ |
| $C_c$ | 0.0 | $mm$ |
| Nominal clearance C | 0.015 | $mm$ |
| Bore diameter | 88.9 | $mm$ |
| Half stroke | 40 | $mm$ |
| Connecting rod length | 141.9 | $mm$ |
| Engine speed | 2000 | $rpm$ |

Table 5.1: Piston system specifications

Assume that $e_t = 0.000005$, $e_b = -0.000005$, $\dot{e_t} = 0.001$, and $\dot{e_b} = 0.003$ for a certain piston position. Figure 5.3 plots film thickness h, see equation (5.2) versus coordinates $\theta$, z. Figure 5.3 shows a typical film thickness profile between liner and skirt for this piston position . Figure 5.4 plots hydrodynamic pressure versus coordinates $\theta$ and shows a corresponding hydrodynamic pressure distribution for the same specified piston position. The same numerical approach described in Chapter 2 was employed to solve this problem with an irregular bearing area. The predicted pressure maximizes near the minimum film thickness region and becomes negative under the geometrically divergent region between the skirt and liner.

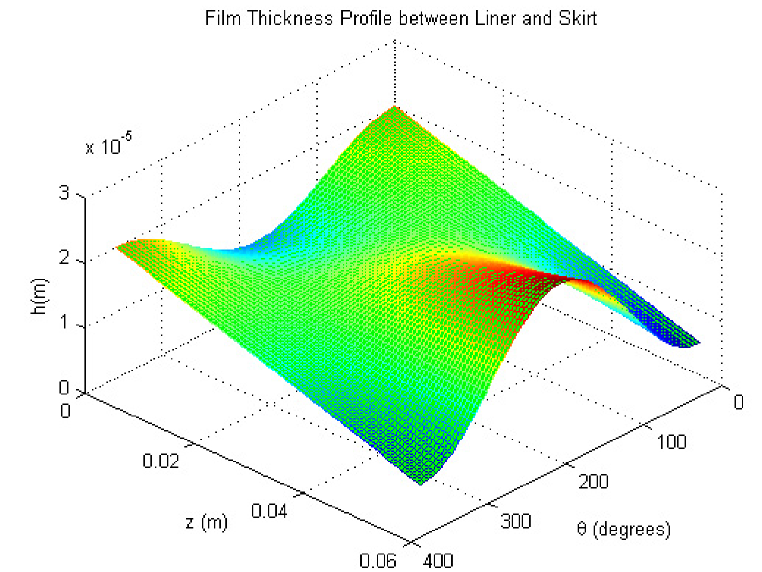


Figure 5.3: Piston skirt and cylinder liner film thickness

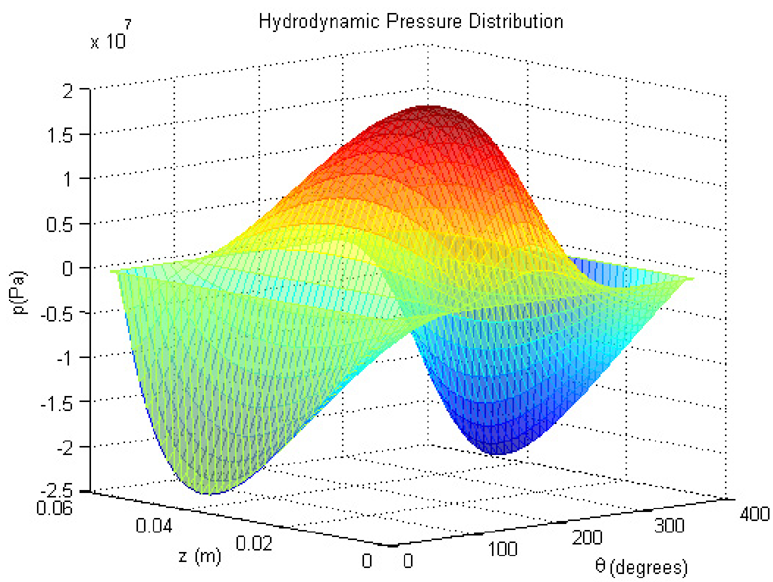


Figure 5.4: Hydrodynamic pressure between piston skirt and cylinder liner

## 5.2 Piston Dynamics

Piston position, velocity, and acceleration along the cylinder axis vary with crank angle, via the kinematics of the slider-crank mechanism. Loads included in the piston dynamics analysis are:

- $F_{gas}$, the combustion gas load acting on the piston head
- $F_h$, the hydrodynamic pressure load, see equation (5.3)
- $F_f$, the viscous friction force, see equation (5.5)
- $F_{cx}$ and $F_{px}$, the inertial forces for piston and wrist pin along the x-axis
- $F_{cz}$ and $F_{pz}$, the inertial forces for piston and wrist pin along the z-axis
- $F_{rod}$, the connecting rod force acting on the pin location

Dynamic equilibrium of the piston motion implied by Figure 5.2 yields

$$F_h + F_{cx} + F_{px} - F_{rod} \sin \phi = 0 \tag{5.7}$$

for forces along the x direction,

$$F_{gas} + F_{cz} + F_{pz} + F_{rod} \cos \phi + F_f = 0 \tag{5.8}$$

for forces along the z direction, and

$$M_h - M_f + M_c + F_{gas} C_p + F_{cx}(a - b) - F_{cy} C_c = 0. \tag{5.9}$$

for moments about the point P, see Figure 5.2.

In equation (5.9), $M_h$ and $M_f$ are given by equations (5.4) and (5.6)

Inertial loads are computed based on the accelerations of piston and wrist pin.

$$F_{cx} = -m_{piston}[\ddot{e}_t + \frac{b}{L}(\ddot{e}_b - \ddot{e}_t)] \quad (5.10)$$

$$F_{px} = -m_{pin}[\ddot{e}_t + \frac{a}{L}(\ddot{e}_b - \ddot{e}_t)] \quad (5.11)$$

$$F_{cy} = -m_{piston}\ddot{z} \quad (5.12)$$

$$F_{py} = -m_{pin}\ddot{z} \quad (5.13)$$

$$M_c = -I_{piston}\frac{\ddot{e}_t - \ddot{e}_b}{L} \quad (5.14)$$

For a normal piston design, $\ddot{e}_b - \ddot{e}_t$ is the same order of $\ddot{e}_t$ and $\ddot{e}_b$, $a$ and $L$ is also in the same order magnitude. The inertial force due to the piston rotational motion should be included in piston dynamics analysis. Note that $a$ and $b$ form moment arm lengths for the rotational acceleration $(\ddot{e}_t - \ddot{e}_b)/L$. This rotating motion contributes to the translational acceleration $\ddot{e}_t$ at points C and P in Figure 5.2

The gas force

$$F_{gas} = \pi R^2 p_{gas} \quad (5.15)$$

Combining Equations (5.7) and (5.8) eliminates the connecting rod load $F_{rod}$, giving

$$-F_{cx} - F_{px} = F_h + \tan\phi F_s - \tan\phi F_f, \quad (5.16)$$

where

$$F_s = F_{gas} + F_{cy} + F_{py}. \quad (5.17)$$

Equation (5.9) rearranged gives

$$-M_c - F_{cx}(a-b) = M_h + M_s - M_f \tag{5.18}$$

where

$$M_s = F_{gas}C_p - F_{cy}C_c \tag{5.19}$$

here $C_p$ and $C_c$ are lateral positions of wrist pin and piston.

$$F_{cx}(a-b) = -m_{piston}[\ddot{e}_t + \frac{b}{L}(\ddot{e}_b - \ddot{e}_t)(a-b)] \tag{5.20}$$

Finally, by substituting all inertial and gas forces as expressed by Equations (5.10) to (5.14), Equations (5.16) and (5.18) can be written into a matrix form

$$A\vec{e} = \vec{F} \tag{5.21}$$

Here

$$A = \begin{bmatrix} (1-\frac{b}{L})m_{piston} + (1-\frac{a}{L})m_{pin} & \frac{b}{L}m_{piston} + \frac{a}{L}m_{pin} \\ \frac{I_{piston}}{L} + (1-\frac{b}{L})(a-b)m_{piston} & -\frac{I_{piston}}{L} + \frac{b}{L}(a-b)m_{piston} \end{bmatrix} \tag{5.22}$$

$$\vec{e} = \begin{bmatrix} \ddot{e}_t \\ \ddot{e}_b \end{bmatrix} \tag{5.23}$$

$$\vec{F} = \begin{bmatrix} F_h + F_s - \tan\phi F_f \\ M_h + M_s - M_f \end{bmatrix} \tag{5.24}$$

In equations (5.22) to (5.24), $F_s$ and $M_s$ are from equations (5.16) and (5.18). $m_{piston}$ and $I_{piston}$ are piston mass and moment of inertia, and $m_{pin}$ is the wrist pin mass.

## 5.3 Numerical Method

Motion equation (5.21) consists of two non-linear second-order differential equations in $e_t$ and $e_b$. An implicit solution method was adopted. Because the piston trajectory should be periodic, the convergent solution should be independent of the initial guess. For simplicity, at the initial time t, $e_t(t) = e_b(t) = \dot{e}_t(t) = \dot{e}_b(t) = 0$. The goal is to determine $\dot{e}_t(t + \delta t)$ and $\dot{e}_b(t + \delta t)$ such that after time step $t + \delta t$,

$$e_t(t + \delta t) = e_t(t) + \dot{e}_t(t + \delta t)\delta t \tag{5.25}$$

$$e_b(t + \delta t) = e_b(t) + \dot{e}_b(t + \delta t)\delta t \tag{5.26}$$

$$\ddot{e}_t(t + \delta t) = \frac{\dot{e}_t(t + \delta t) - \dot{e}_t(t)}{\delta t} \tag{5.27}$$

$$\ddot{e}_b(t + \delta t) = \frac{\dot{e}_b(t + \delta t) - \dot{e}_b(t)}{\delta t} \tag{5.28}$$

satisfy equation (5.21).

Define a vector

$$\vec{f} = A\vec{e}(t + \delta t) - \vec{F}(t + \delta t). \tag{5.29}$$

based on equation (5.21). Here matrix A only depends on the piston and wrist pin parameters, $\vec{F}$ is a function of $(e_t(t + \delta t), e_b(t + \delta t), \dot{e}_t(t + \delta), \dot{e}_b(t + \delta))$, and $\vec{e}$ is a function of $(\ddot{e}_b(t + \delta t), \ddot{e}_b(t + \delta t))$.

Equation (5.21) is satisfied if $\vec{f} = 0$. If not, a new pair of $\dot{e}_t(t+\delta t)$, $\dot{e}_b(t+\delta t)$

is needed by a Newton-Raphson iterative scheme, which is similar to that described by Li [23]. Detail of numerical scheme is attached in Appendix D. The value of $\delta t$ is five degrees crank angle. A fast algorithm which excludes the successive update of Jacobian matrix is proved efficient and stable.

## 5.4 Results and Discussions

Figure 5.5 plots gas pressure inside an engine combustion chamber versus crank angle. This data was measured [74]. To ensure numerical stability of the pressure-driven piston dynamic calculations, the pressure peak that appeared at crank angle 180 degrees in Figure 3.4 and 4.3 was purposely shifted to the crank angle of zero degrees in Figure 5.5, where it became an initial condition. This arrangement is only for the simplification of numerical solution. From practical experience, piston skirt has low secondary motion at the highest gas pressure location and is close to zero initial condition during numerical implementation.

Piston secondary motion is described by two eccentricity ratios $E_t$ and $E_b$. Here $E_t = \frac{e_t}{C}$, $E_b = \frac{e_b}{C}$.

### 5.4.1 Effect of Wrist-Pin Location

Figure 5.6 plots the piston skirt secondary motion versus crank angle for small (0.152 mm) and large (1.0 mm) pin offsets $C_p$, and low wrist pin location $a$ (= 17.3 mm), see Figure 5.2. The positive directions of $e_t$ and $e_b$ are defined in Figure 5.1. The wrist-pin location is important for controlling piston motion in the cylinder bore. For small wrist pin offset $C_p$ (with respect to the center at the middle of the skirt), the upper skirt experiences large oscillations which could generate undesirable noise. Comparing the amplitudes of the upper skirt curves of Figure 5.6 suggests that the oscillation of the upper skirt can be reduced by an appropriate pin offset.

Figures 5.7 plots the corresponding viscous friction force versus crank angle

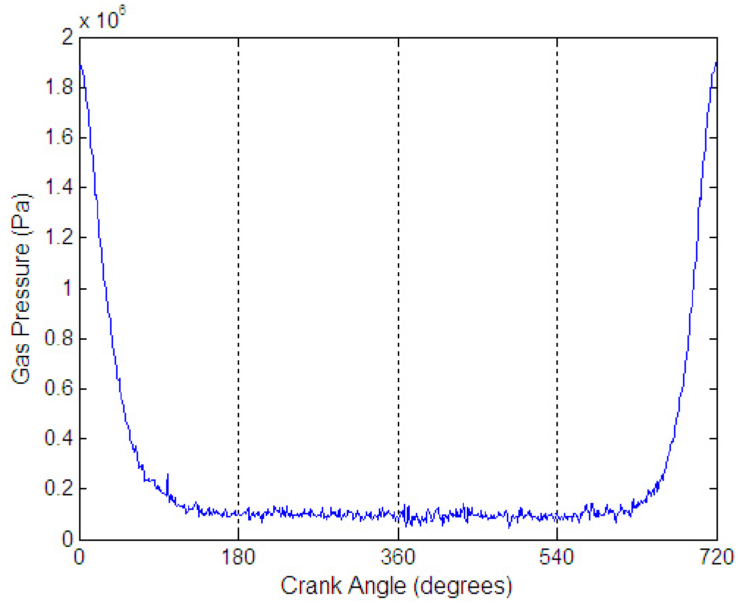


Figure 5.5: Engine combustion chamber gas pressure

for different wrist pin locations. The plot shows small friction force near dead centers, which suggests that the piston skirt doesn't experience boundary lubrication under normal operating conditions.

Appropriate wrist pin offset can also minimize the piston skirt friction force as shown in Figures 5.6 and 5.7. In general, offsetting the wrist pin into a desirable location is an effective way to control the skirt-liner friction loss. It also show the piston secondary motion is reduced significantly by a low pin location along the cylinder axis.

### 5.4.2 Effect of Skirt-Bore Clearance

The influence of the skirt-bore clearance $C$ on piston motion was also investigated. Figures 5.8 and 5.9 plot piston skirt secondary motion (in terms of eccentricity ratio) and friction force versus crank angle. Small skirt-bore clearance results shown in

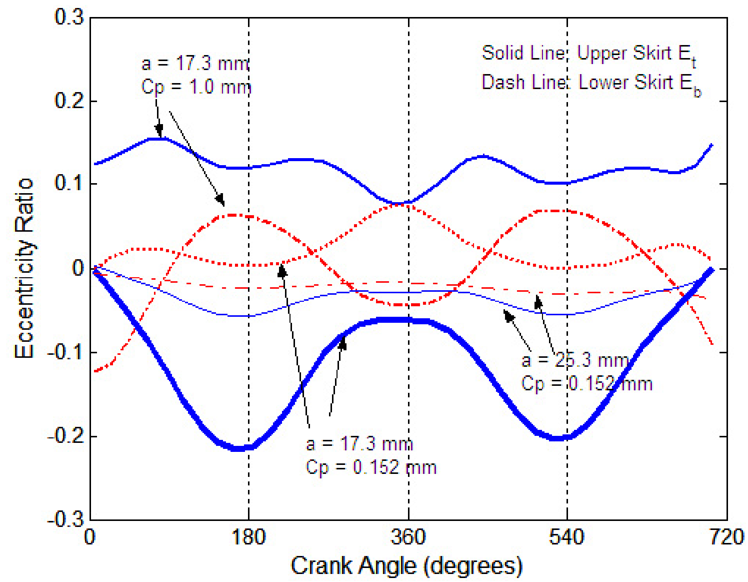


Figure 5.6: Piston trajectory for different pin locations

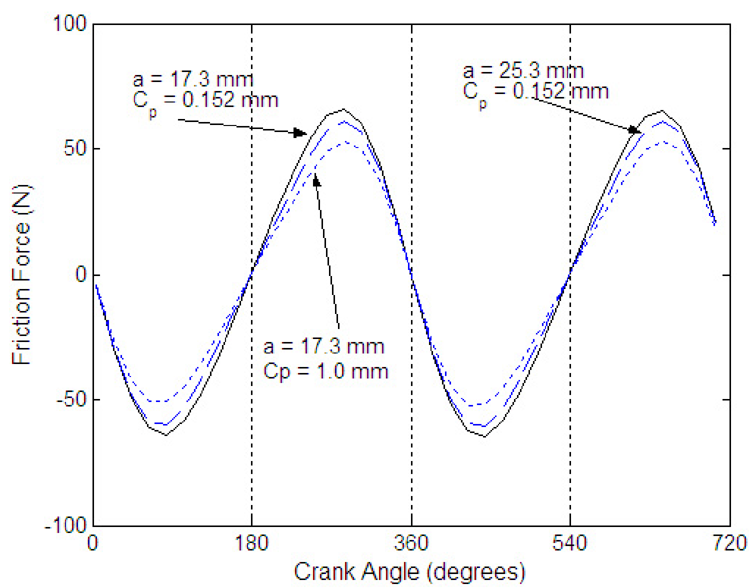


Figure 5.7: Viscous friction force for different pin locations

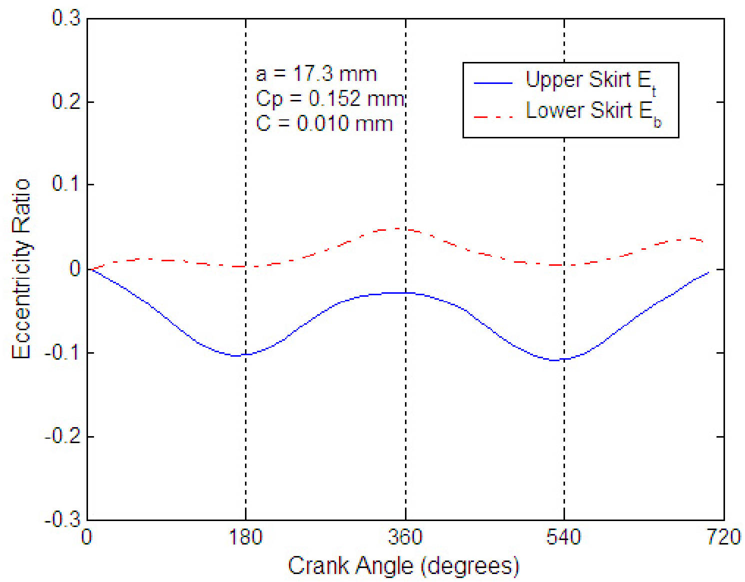


Figure 5.8: Piston trajectory for small skirt-bore clearance

Figures 5.8 and 5.9 compared to results in Figures 5.6 and 5.7 indicate that a small skirt-bore clearance design will constrain the piston secondary motion and result in a larger friction loss.

### 5.4.3 Effect of Engine Speed

Figures 5.10 and 5.11 show piston secondary motion and friction force at higher engine speed (3000 rpm). Compared to results in Figures 5.6 and 5.7, the secondary motion has decreased, likely due to stronger hydrodynamic action in the lubrication film induced by higher speed. However, the friction force has increased, probably due to a higher shearing rate in the lubricant thin film associated with higher speed.

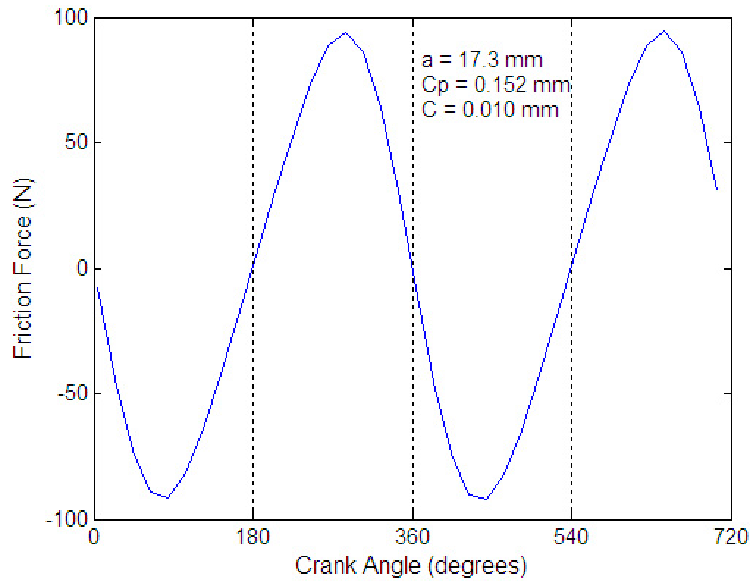


Figure 5.9: Viscous friction force for small skirt-bore clearance

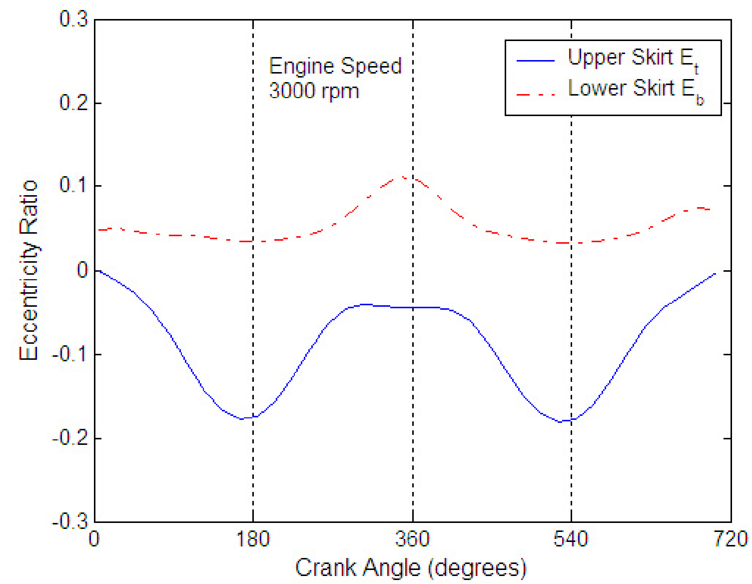


Figure 5.10: Piston trajectory at 3000 rpm engine speed

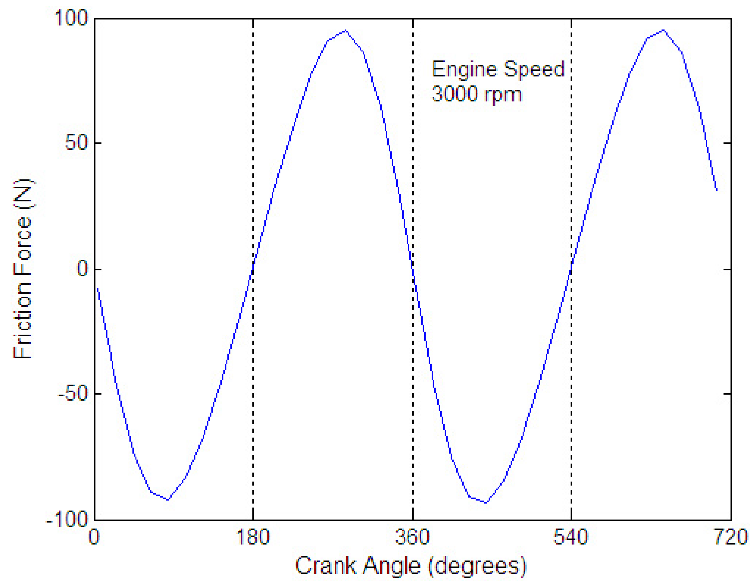


Figure 5.11: Viscous friction force at 3000 rpm engine speed

### 5.4.4 Effect of Piston and Wrist Pin Mass

Figures 5.12 and 5.13 show piston motion and friction force for a smaller piston mass ( 0.5 $kg$ about two-thirds of the original Table 5.1 value). Figures 5.14 and 5.15 plot piston motion and friction force for the wrist pin mass of 0.3 $kg$, double that in Table 5.1. These plots suggest that piston and wrist pin mass contribute little to friction loss, as long as the pin offset is small.

## 5.5 Summary

Under normal engine operating conditions, a hydrodynamic model sufficiently describes the piston skirt lubrication. In general, the friction between skirt and liner is caused by viscous shearing loss in the lubricant film. Abrasive wear rarely occurs during reciprocating motion of pistons. However, skirt friction still comprises half

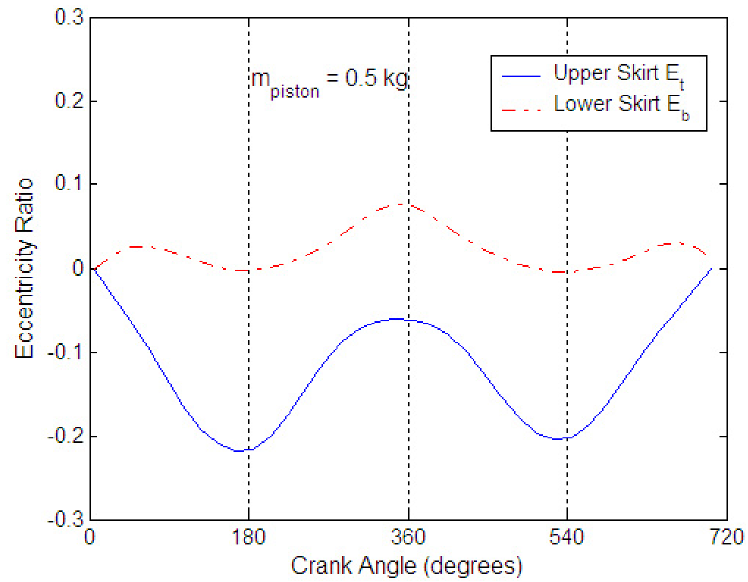


Figure 5.12: Piston trajectory with light piston

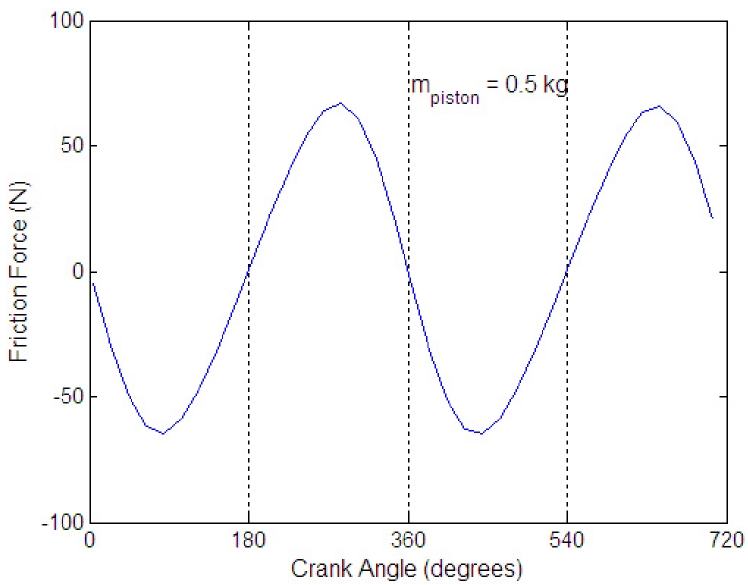


Figure 5.13: Viscous friction force with light piston

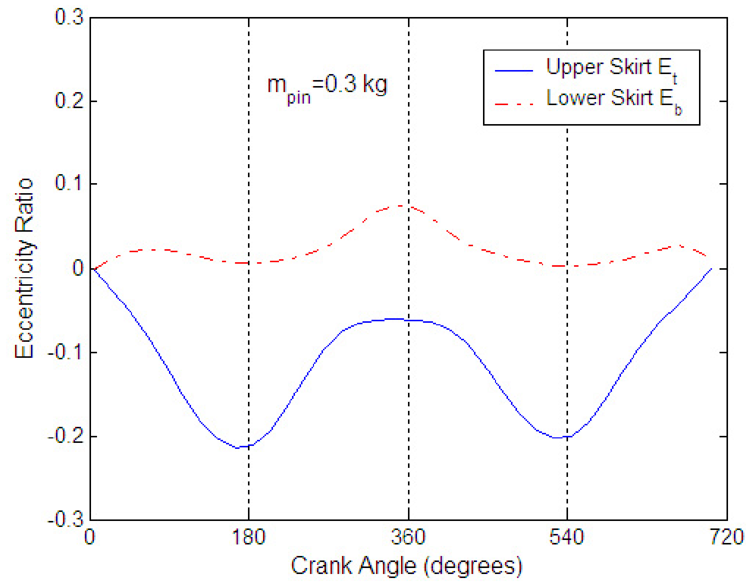


Figure 5.14: Piston trajectory with heavy wrist pin

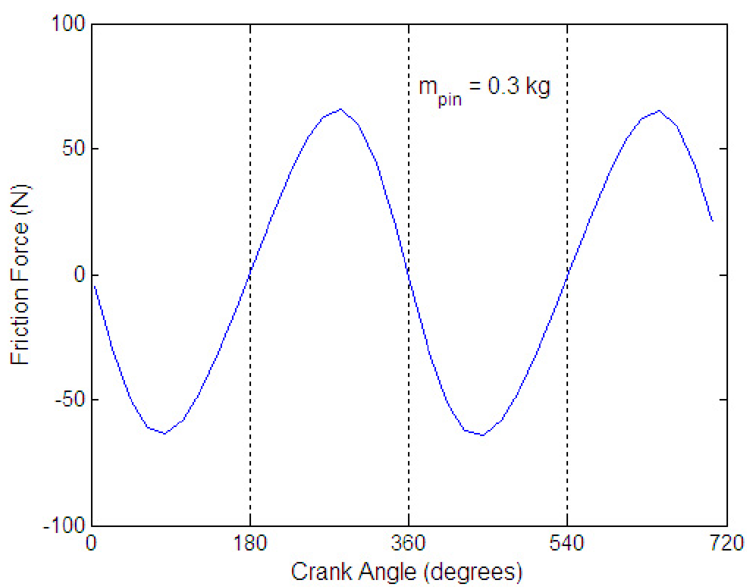


Figure 5.15: Viscous friction force with heavy wrist pin

the total piston assembly mechanical loss, due to large bearing area. The numerical approach to the piston skirt lubrication problem was more complicated than the piston ring lubrication model. A fast Newton-Raphason was implemented to solve the non-linear piston motion equations. The influence of piston, skirt, and wrist pin design on the piston secondary motion and the skirt friction were investigated. Results suggest that the wrist pin position offset can reduce the piston friction and slap. Skirt-bore friction increased significantly with a small clearance design.

# Chapter 6

# Lubrication Analysis of Piston Ring in Rotating Liner Engine

## 6.1 Survey of Sleeve-Valve Engine

Sleeve-valve engines were first introduced in automobiles in the early 20th century to reduce engine noise caused by the poppet-valve mechanism. A sleeve-valve engine has no proper valves. The sleeve inside the cylinder rotates and opens or closes small inlet or exhaust ports in the cylinder. Burt-McCollum's single-sleeve valve was most successful. However, the designers of poppet-valve engines silenced their valve mechanism and the sleeve-valve design lost advantage. In the 1920's, English engine designer, Harry Ricardo, sought sleeve-value engines in military airplanes for higher compression ratios and more power. Comparative tests on single sleeve-valve and poppet-valve engines with similar bore, strokes, compression ratio of 4.8:1, and optimum valve and ignition-timing, indicated [79]:

- The poppet-valve engine could cause detonation, not present with sleeve-valve engines.

- Mechanical efficiency of the sleeve-valve engine was better
- The sleeve, internally and externally well lubricated, maintained lubrication films on standard piston rings, even when the engine shut down abruptly.

The most puzzling result, high mechanical efficiency as indicated by the motoring tests and confirmed by the performance tests, suggested that sleeve motion reduced piston assembly friction. With a conventional liner, a piston assembly experiences high friction loss at the end of the stroke, both TDC and BDC; here relative motion between the piston and cylinder/liner cease, which causes hydrodynamic lubrication to vanish. A sleeve mechanism with a continuous motion maintains a hydrodynamic film throughout the entire cycle of the sleeve-valve engine. Sleeve wear was barely one tenth that of a stationary liner.

Sleeve-valve engines after World War II, exhibited good performance and significant overhaul interval [80]. Tests revealed overall mechanical losses usually less than poppet-valve engines, likely due to smaller friction between the sleeve and piston assembly. For conventional liner internal combustion engines, sharply localized liner wear appears where the piston-ring rests at TDC. This wear is absent in sleeve-valve engines. Many high-speed sleeve-valve internal combustion engines in service for many years had over 60,000 hours of running time, with very little wear.

The rotating liner concept was introduced into a reciprocating internal combustion engine design, to reduce piston assembly friction loss and cylinder liner wear [81]. To complement this effect, a hydrodynamic lubrication model was formulated to describe the low friction mechanism of RLE design. The piston ring mixed lubrication model will be extended to include liner motion. Numerical simulation will suggest liner rotation can minimize piston ring friction force and eliminate the liner wear.

## 6.2 Hydrodynamic Lubrication Model of RLE Piston Ring

Classical hydrodynamic lubrication theory described in Chapters 2 and 3 demonstrated that the minimum film thickness between ring and liner is less than the composite surface roughness. Under these conditions, ring-liner surface contact is inevitable. A rotating liner mechanism provides a circumferential velocity to generate additional hydrodynamic separation force, maintaining a convergent-wedge effect even if axial velocity vanishes. The rotating liner creates a journal bearing action which renders hydrodynamic supporting force in addition to parallel sliding.

The hydrodynamic lubrication pressure is governed by a 2D Reynolds equation

$$\frac{\partial}{\partial x}(\frac{h^3}{\eta}\frac{\partial p}{\partial x}) + \frac{\partial}{\partial z}(\frac{h^3}{\eta}\frac{\partial p}{\partial z}) = 6U\frac{\partial h}{\partial x} + 6W\frac{\partial h}{\partial z} + 12\frac{\partial h}{\partial t}, \tag{6.1}$$

here U is piston reciprocating speed in the axial direction x and W is liner rotating velocity along the circumferential direction z. Film thickness h, presented later, is a sinusoidal function for a parallel sliding mechanism, and a linear function for a journal bearing mechanisms.

### 6.2.1 Parallel Sliding Mechanism

When perfectly parallel surfaces slide in the presence of a lubricant film, classical hydrodynamic lubrication asserts no load carrying ability. Parallel sliding mechanisms with application to mechanical face seals was reviewed by Lebeck [82] [83].

Fogg suggested a thermal or density wedge to explain parallel thrust bearing experimental observations [84]. Lubricant passing through the bearing, heats due to viscous friction. As the lubricant density decreases, flow continuity requires an increased lubricant pressure. This effect, along with boundary pressure can support load in the lubricant film. Osterle et al solved the mathematical model of the thermal wedge; here Reynolds and energy equations were solved simultaneously [85]. Results suggested a support load generated, even without a wedge effect. However, Cameron [86] and Dowson [87] later showed that the variation of lubricant properties could not fully explain the steady-state performance of parallel-surface bearings.

A viscosity wedge proposed by Cameron [88] proved an impractical model of a real bearing system. Ettles and Cameron summarized earlier researcher's work and experimentally investigated the pressure generation of parallel-surface bearings. A lubrication theory was developed for the infinitely wide bearing, by including the thermal distortion of the bearing surface [89].

Other concepts to explain the parallel bearing load generation, include Lewicki's leading edge ram pressure [90], squeeze film, and deviation from parallel geometry [83]. Here deviations from parallelism can arise from thermal distortions, elastic deformations, or imprecise lapping processes. Both surface macro-roughness (waviness) or micro-roughness can generate hydrodynamic load support [83].

RLE piston ring lubrication will be modelled by a parallel sliding mechanism with a geometrical deviation from parallelism. The geometrical derivation can arise from bore distortion, ring elasticity, and ring-liner relative motion. The geometrical deviation will be included in the model as a sinusoidal surface waviness between the surfaces of the ring and liner, extending along the circumferential direction. Figure 6.1 illustrates the geometry interface between ring and liner.

The local film thickness function h is

$$h(x,z,t) = h_{min}(t) + \frac{c}{(B/2)^2}x^2 + \frac{\sin(200z)}{10^6}. \tag{6.2}$$

Where c is the ring crown height and B is the ring axial height. The numbers 200 and $10^6$ represent wavelength and amplitude of surface waviness, in $\mu$ m.

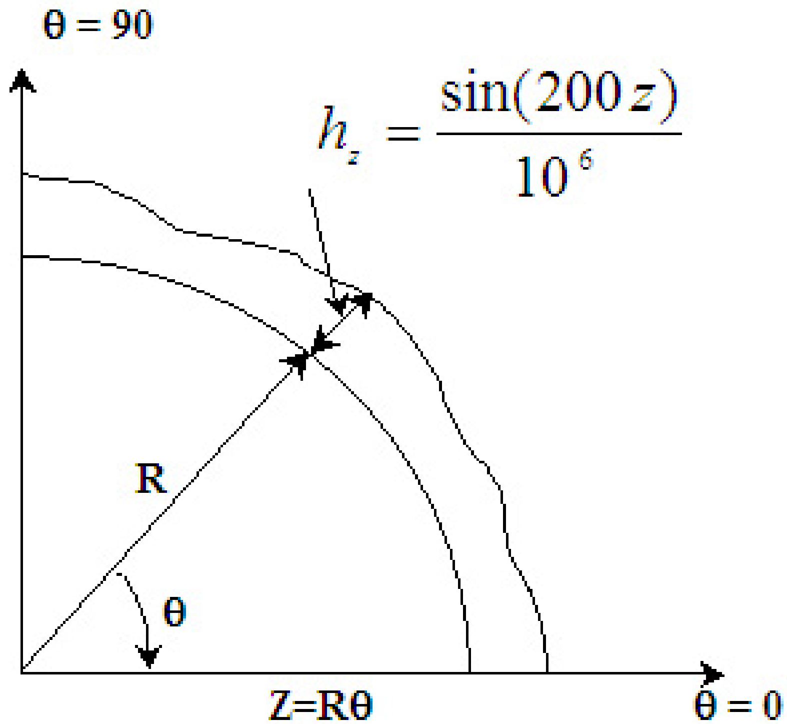


Figure 6.1: Ring-liner interface conjunction of RLE

### 6.2.2 Journal Bearing Mechanism

Lebeck concluded that friction of parallel sliding and journal bearings are similar. Both show an increased fluid pressure load with increased speed [83].

The journal bearing model can explain the RLE low friction loss. However, for the journal bearing, the radial force equilibrium condition is questionable due to the ring end gap and the ring tension. During engine start/stop, hydrodynamic pressure is slowly established, and ring-liner surface contact is unavoidable. In account for these effects, a mixed lubrication model will be introduced in the next section.

## 6.3 Mixed Lubrication Model of RLE Piston Ring

If hydrodynamic pressure is inadequate, mixed lubrication with surface contact occurs. Mixed lubrication, governed by a combination of boundary and fluid film effects, has an average film thickness less than 1 $\mu$m [47]. Since the late 1960s, unifying models of mixed lubrication have included Patir and Cheng's macro-scale stochastic approach [28] [51], Oh's complementarity model [91], and Heshmat's morphological method [92]. Mixed lubrication was recently reviewed by Cheng [93] and Spikes [94]. Numerical algorithms usually decompose the load-bearing surface into three distinct subregions: solid-to-solid contact, hydrodynamic lubrication, and cavitation. The hydrodynamic pressure is governed by a 2D average Reynolds equation

$$\frac{\partial}{\partial x}(\phi_x \frac{h^3}{\eta}\frac{\partial \overline{p}}{\partial x}) + \frac{\partial}{\partial z}(\phi_z \frac{h^3}{\eta}\frac{\partial \overline{p}}{\partial z}) = 6U\frac{\partial \overline{h_T}}{\partial x} + 6U\sigma\frac{\partial \phi_s}{\partial x} + 6W\frac{\partial \overline{h_T}}{\partial z} + 6W\sigma\frac{\partial \phi_s}{\partial z} + 12\frac{\partial \overline{h_T}}{\partial t}. \tag{6.3}$$

Here U is piston reciprocating speed and W is liner rotating velocity. The above equation is an extension of equation (3.12) by adding more wedge terms. All parameters are same as equation (3.12).

Different surface asperity contact models analyze solid-to-solid contact. Usually friction force is proportional to the contact load by a constant friction coefficient. A higher-degree of freedom bearing surface can reduce friction force [95] [96]. Twisting makes easier removal of a nail from wood. A portable floor buffing machine can be pulled back and forth while it is working. These phenomena can be explained by a side-slip friction model [97] which will be applied to RLE piston ring lubrication. The side-slip model attempts to emulate the lower speed behavior of the Stribeck diagram. The side-slip aside from the principal motion creates additional velocity. This addition movement increases the overall velocity which combines the principal and side-slip motions. In mixed lubrication regime, the friction coefficient decreases as the relative motion velocity increases.

By incorporating a side-slip friction model, the friction coefficient under a lubricated contact $\mu_f$ is given by

$$\mu_f = \frac{U}{\sqrt{(R\omega)^2 + U^2}}\mu_0 \tag{6.4}$$

where $\mu_0$ is the boundary friction coefficient, $U$ is the piston reciprocating speed, $\omega$ is the liner rotating speed, and R is bore radius. In the vicinity of dead centers, the piston speed $U$ is low compared to the liner rotation velocity $R\omega$. The above equation can be written as

$$\mu_f = \frac{U}{R\omega}\mu_0 \tag{6.5}$$

## 6.4 Results and Discussions

Numerical approach is similar to the ring-liner mixed lubrication model for conventional liner engines in Chapter 3. One noticeable difference was that Equation (3.13) is solved under test-rig condition while Equation (6.3) is under engine-motoring condition. The pressure boundary condition for the RLE model is complex.

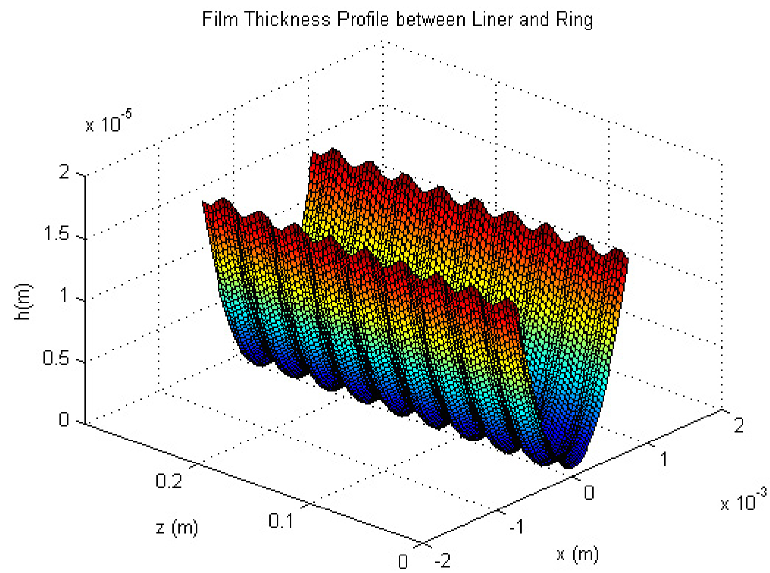


Figure 6.2: Piston ring and cylinder liner film thickness

Assume that the liner rotating speed is 200 rpm and yields about 1 m/s liner velocity W in Equations (6.1) and (6.3). Here a numerical approach similar to the generalized Reynolds equation in Chapter 2 is employed.

Figure 6.2 plots film thickness versus position within the bearing area and shows a sinusoidal waviness profile between liner and skirt. Figure 6.2 is based on equation (6.1). Figure 6.3 plots hydrodynamic pressure versus position within the bearing area. The sinusoidal profile acts like a series of step bearings and a significant hydrodynamic load is generated by the wedge mechanism.

Figures 6.4, 6.5, and 6.6 plot the minimum film thickness, friction force, and power loss versus crank angle for the rotating line engine design, respectively.

Numerical results suggest additional hydrodynamic restoring force generated from a surface waviness wedge is enough to separate the ring and liner. Both friction force and power loss reduced compared to a conventional engine design, as shown

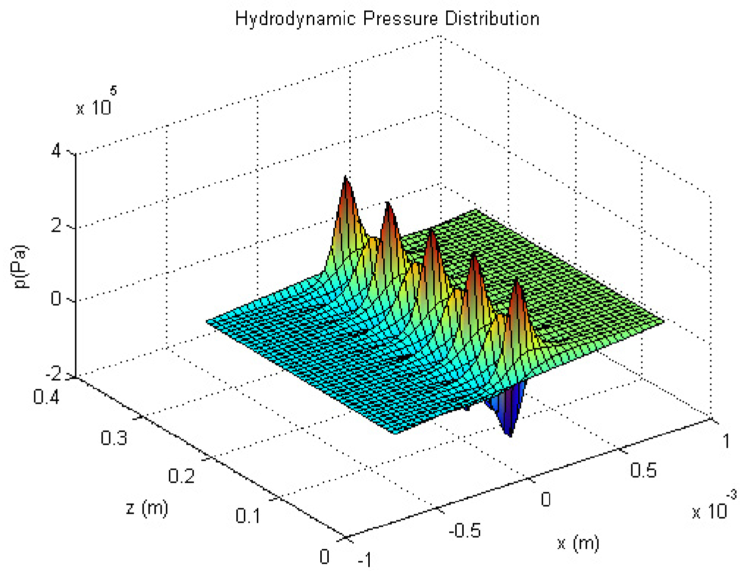


Figure 6.3: Hydrodynamic pressure between piston ring and cylinder liner

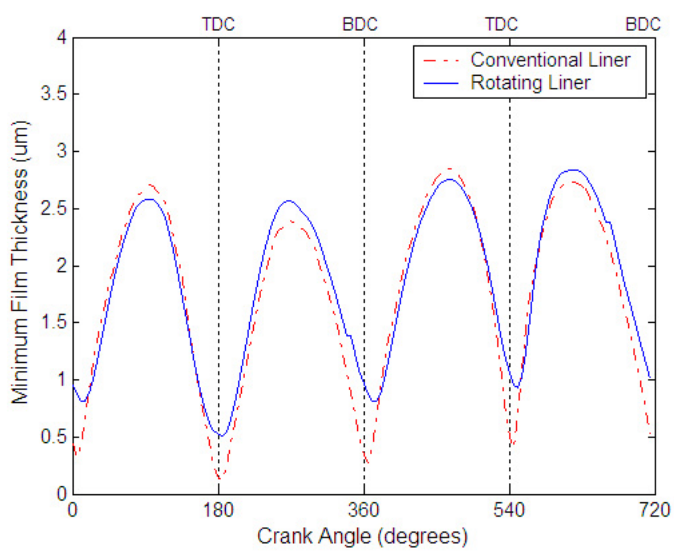


Figure 6.4: Compression ring minimum film thickness for RLE

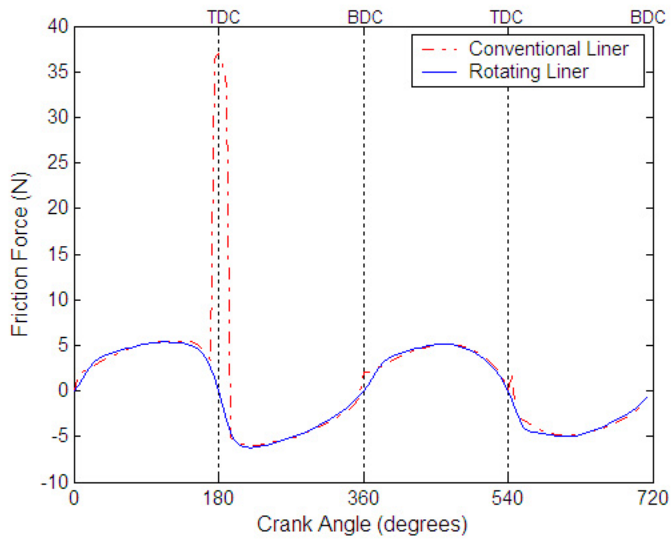


Figure 6.5: Compression ring friction force for RLE

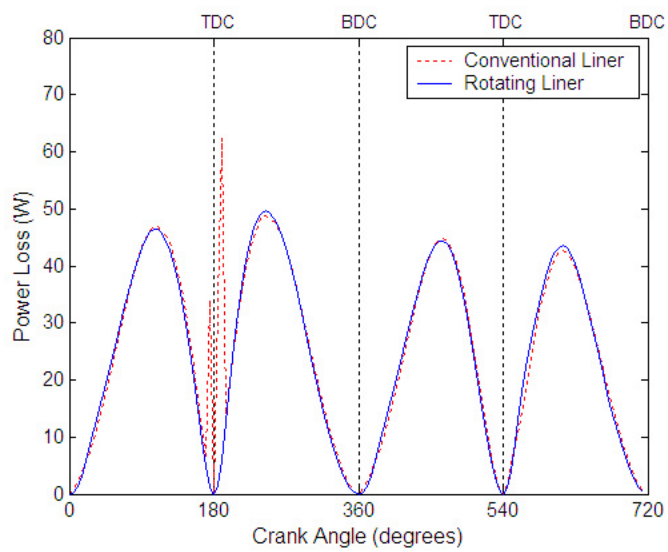


Figure 6.6: Compression ring power loss for RLE

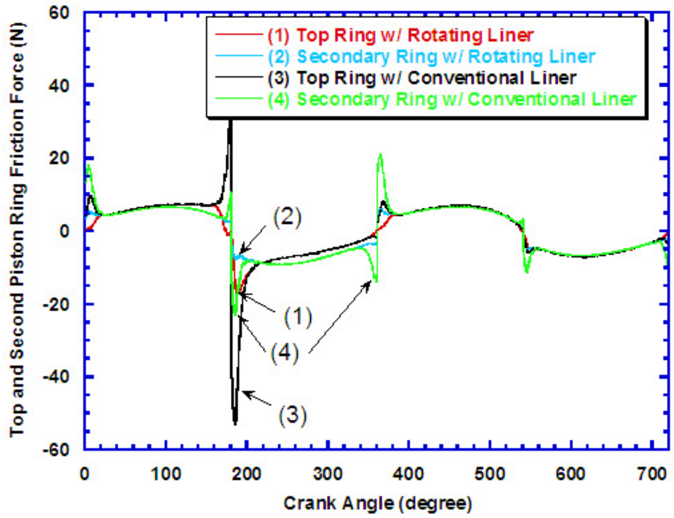


Figure 6.7: Piston ring friction force for conventional and RLE

in Figures 3.8 and 3.9.

Figures 6.7 and 6.8 plot compression ring friction force versus crank angle. Both top and secondary piston ring friction forces under both conventional and rotating liner design were predicted with a mixed ring lubrication model. Friction forces for the top ring are shown in Figure 6.8 under different liner rotating speeds. All curves are similar, piston ring friction force was reduced significantly as engine speed went higher.

Numerical results in Figure (6.7) suggests that ring friction reduced near TDC with increased liner rotation speed. Potentially, the RLE design could diminish piston assembly friction and liner wear. However, total engine friction power loss reduction may not be appreciable since the piston speed is low near TDC [98].

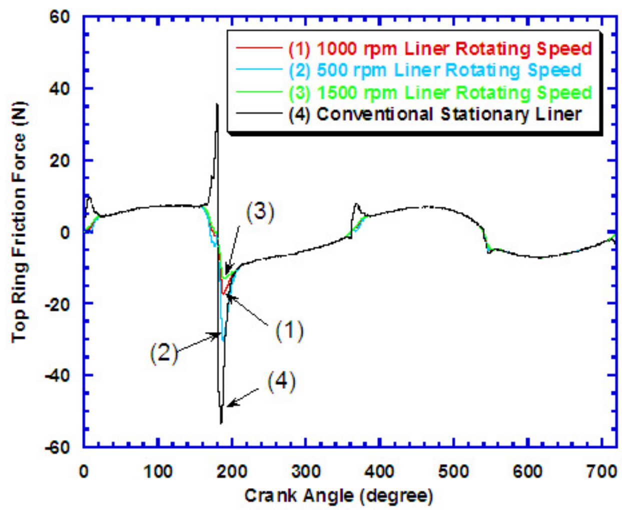


Figure 6.8: Compression ring friction force for RLE under different liner speed

## 6.5 Summary

Both hydrodynamic and mixed lubrication models were developed to investigate the low-friction merit of piston ring lubrication for Rotating Liner Engine (RLE) designs. The RLE mechanism was first analyzed as a parallel slider thrust bearing. A sinusoidal surface waviness was employed to describe the ring-liner gap along the circumferential direction. Numerical results indicated the minimum film thickness could exceed the composite surface roughness threshold, and avoid metal-to-metal contact. Friction force plot also showed that viscous friction is dominant force to dissipate the friction power. A journal bearing mechanism was also adopted to model the RLE ring lubrication. Finally, a side-slip friction sub-model was incorporated into a rigorous piston ring mixed lubrication model. Low-friction ring mechanism in RLE design was confirmed by numerical results compared to conventional liner engine design. High friction force spikes near dead centers were suppressed.

# Chapter 7

# Modelling of Cylinder Liner Wear

Engine life is limited by excessive ring-liner wear. Under normal engine conditions, corrosive, abrasive, and adhesive wear attack the ring-bore interface. Corrosion, dominant when an engine is very cold or very hot, can be controlled by thermostats and by addition of corrosion inhibitors to engine oil. Pervasive abrasive wear at both ring and liner generated by hard particles trapped in the oil film has received the most attention [37] [38] . Adhesive wear from strong adhesive bonding between interaction asperities (micro-welding) occurs when the oil film between the ring and bore is less than the composite surface roughness.

A ring-bore system model of reasonable accuracy is needed [99]. However, few models predict the ring-liner wear. Although cylinder bores are more expensive to be replaced than piston rings, more ring wear models [100] [101] exist due to simpler experimental validation. Surface coatings can increase the wear resistance of rings. The crowned chrome plated top ring, with quick seating and high wear resistance has gained wide acceptance. In small-bore high speed engines, ring temperature is beyond the limit of chrome plating. An alternative solution is to apply metallic powders deposited on the ring surface by plasma arc spraying [102] [25].

In general, ring-liner wear is complex and influenced by

- Metallurgy of contacting materials
- Surface condition (roughness, honing pattern, etc.)
- Engine operation condition (load, speed, temperature, etc)
- Lubricant formulation

Most wear equations are empirical and are not valid beyond the experimental conditions. For the ring-liner sliding system, wear rate will be assessed by Archard's equation:

$$v = \frac{kLS}{H} \tag{7.1}$$

where $k$ is a non-dimensional wear coefficient, $L$ the normal load, and $S$ the sliding distance. In equation (7.1), $H$ is the hardness of the liner, since rings are generally harder and thus more wear resistant than the liner. This equation applies to adhesive and abrasive wear. Abrasive wear is about two to three orders of magnitude larger than adhesive wear. Typical $k$ values for abrasion value vary from $10^{-6}$ to $10^{-1}$. Equation (7.1) is also valid for three-body abrasive wear; here $k$ is about one order of magnitude lower, because many of abrasive particles tend to roll, rather than slide. For similar reason, the coefficient of friction during three-body abrasion is also less than that for two-body abrasion [103].

The wear coefficient depends on material properties such as surface hardness and roughness. Starting from the ring-liner lubrication analysis, a simplified three-body abrasive wear model will be developed, to address the wear progression of the cylinder liner at steady-state. Wear rates for both conventional and RLE liners will be evaluated.

## 7.1 Cylinder Liner Wear Model

Archards's wear law implies a dimensional wear constant $K = k/H$ as introduced in Equation (7.1). Here wear volume $v = \delta A$, where $\delta$ is the wear depth and $A$ is the area about the wear scar, taken to be equal to the apparent contact area. Equation (7.1) can be rewritten

$$\delta = KS\frac{L}{A} \tag{7.2}$$

With average contact pressure $p = L/A$, which describes the pressure between contacting surfaces, Equation (7.2) becomes

$$\delta = KSp \tag{7.3}$$

The sliding distance $S$ can be estimated by considering that during one stroke a segment of bore slides by the ring, a distance equal to one ring height. Therefore, for one engine cycle, the sliding distance at a given time t (in minutes) is

$$S = 4B\frac{N}{2}t. \tag{7.4}$$

Here B is the ring height, and $N$ is the engine speed (rpm).

The cylinder bore wear depth $\delta$ can be further written as

$$\delta = 2KBNtp, \tag{7.5}$$

where the liner wear constant $K$ is $10^{-17}$ for the boundary lubrication regime. In the hydrodynamic lubrication regime, the wear constant is zero. In the mixed lubrication regime, the wear constant is a linear interpolation function of minimum film thickness [37].

$$K = \frac{K_b}{2}(3 - \frac{h_{min}}{\sigma}) \tag{7.6}$$

where $\sigma$ is the ring-liner composite surface roughness, $K_b$ is the liner wear constant for the boundary lubrication regime. Equation (7.6) is valid for $\sigma < h_{min} < 3\sigma$. For the hydrodynamic lubrication regime ( $h_{min} > 3\sigma$ ), the wear constant is zero.

## 7.2 Results and Discussions

The cylinder bore wear estimation is straightforward and based on Equation (7.5). The wear constant selection is same as [37]. The cylinder bore wear depth is a linear function of time, engine speed, and combustion chamber pressure. Generally, the minimum film thickness between ring and liner reflects their lubrication regimes and determines the liner wear constant $K_b$.

The wear depth of a cylinder liner subjected to top compression ring was estimated via Equation (7.5). Two different cases are studied here: conventional liner design and rotating liner design. Liner wear constant $K_b$ selections are based on the ring-liner lubrication regimes with their minimum film thickness plots shown in Figure (3.6) and Figure (6.4), respectively. In the hydrodynamic lubrication regime, the wear constant is zero. In the boundary lubrication regimes, the wear constant is $K_b$. $p$ depends on the pressure acting on the back of ring and is equivalent to combustion chamber gas pressure. The ring height $B$ is 1.475 $\mu m$.

Figure 7.1 plots the liner wear depth versus crank angle after 100 hours operation. The liner wear depth was computed after 100 hours operation under 2000 rpm engine speed, with conventional and rotating liner designs.

Figures 7.2 and 7.3 plot the liner wear depth versus crank angle for steady-state operation. It show the progression of liner wear depth as a function of time with conventional and rotating liner designs.

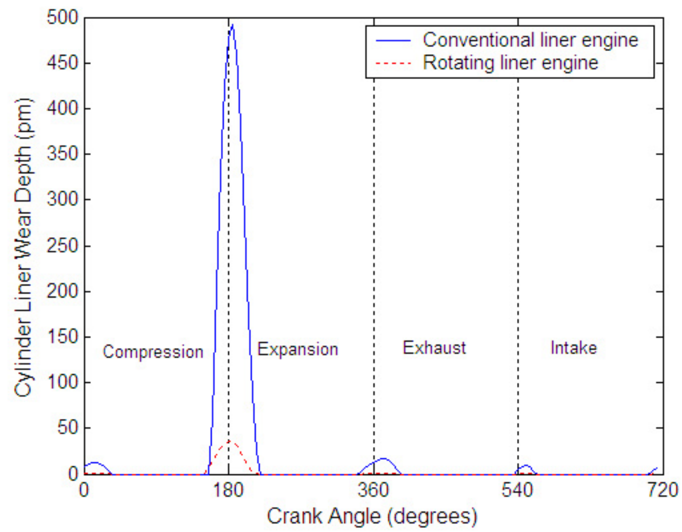


Figure 7.1: Cylinder liner wear depth for conventional/rotating liner engines after 100 hrs operation

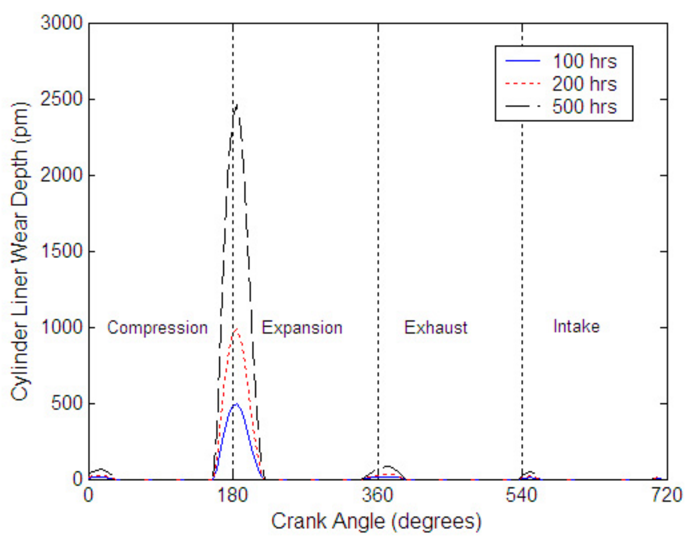


Figure 7.2: Cylinder liner wear depth progression for conventional liner engines

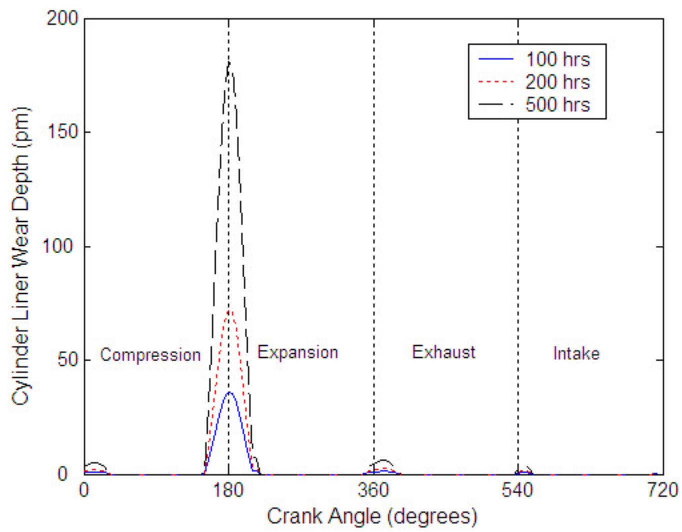


Figure 7.3: Cylinder liner wear depth progression for rotating liner engines

For a conventional liner design, the liner wear occurs in the vicinity of both TDC and BDC. For a RLE liner design, the liner wear, one order lower than the conventional design, mainly occurs at the end of the compression stroke and the beginning of the expansion stroke.

In an internal combustion engine, contact between the piston ring and liner initially cause a rapidly increased wear due to run-in. Wear then attains a steady state. Rotating liner engines appear to have much lower wear, since the minimum film thickness near the dead center areas is higher than the surface composite roughness. Boundary lubrication is ultimately avoided. Experiments are needed to estimate the wear constant $K_b$ under different engine operating conditions.

## 7.3 Summary

Based on Archard's wear law, a simple three-body wear model was developed to describe cylinder liner wear progression, subjected to load applied by the top compression ring. Liner wear depths were evaluated for both conventional and rotational liner designs. The cylinder bore wear region correlated with the low minimum film thickness area. Maximum wear occurs at TDC where the combustion chamber gas pressure peaked. The liner wear depth is also a linear function of time. Cylinder liner wear in rotating liner engines is about one order lower than that of conventional liner engines.

# Chapter 8

# Conclusions and Future Directions

## 8.1 Conclusions

This dissertation developed a piston assembly lubrication model. A complete software infrastructure was built based upon the computational model of piston assembly lubrication. The code is listed in Appendix A. Contributions of this dissertation include

1) Peeken's flow factor was applied to an Average Reynolds equation. Numerical predictions of friction force approached more realistic values under near contact condition. A soft elastohydrodynamic lubrication model of for a piston ring was solved, including the elastic surface deformation of ring and liner from the hydrodynamic pressure.

2) A new gas flow model was developed with a temperature gradient along the radial of the piston assembly. The complete ring pack friction prediction incorporated the present gas flow model. Estimates of axial motion of two compression rings agree well with experiment.

3) A fast Newton-Raphson algorithm was implemented into the piston skirt lubrication model. The entire piston trajectory was predicted under engine motoring condition, with improved computational efficiency.

4) The lubrication mechanism for the rotating liner engines was investigated. Both parallel sliding and side-slip mechanisms were employed to explain the low friction phenomenon of the RLE design. Numerical simulations showed that the asperity contact was possibly eliminated by liner rotation. A simplified three-body cylinder liner wear model confirmed the liner wear depth and progression for both conventional and rotating liner engine designs.

5) The programs including piston ring, piston ring pack, piston skirt lubrication analysis were developed. It serves as an analytical tool to optimize the piston assembly design.

## 8.2 Future Directions

This dissertation suggests further research:

First, Greenwood' asperity contact model was employed in the piston mixed lubrication model. Greenwood model was validated for static contact problems [104] [105], however, restrictions such as Gaussian distribution of asperity heights and elastic deformation of asperities do not match the ring-liner surface characteristics very well. Also, the dynamic/kinetic contact problem, such as the ring-liner sparse asperity contact, is need further study.

The side-slip friction model is a bold assumption and should be confirmed by a bench test. In practice, the relationship between friction, wear and motion of mating surfaces has been observed experimentally.

Finally, the skirt motion influence on piston ring lubrication need more study. Ring tilt resulting from piston secondary motion changes the local film thickness. A multi-dimensional ring-liner lubrication model is needed to address this issue.

# Appendix A

# Nomenclature

## A.1 Chapter 2

| | |
|---|---|
| $\rho$ | fluid density |
| $u_i$ | fluid velocity |
| $x_i$ | axis |
| $f_i$ | external mass force density |
| $\sigma_{ij}$ | stress tensor |
| $\eta$ | absolute viscosity |
| $p$ | hydrostatic pressure |
| $\delta_{ij}$ | Kroenecker delta |
| $h$ | film thickness |
| $U_i, V_i, W_i$ | boundary velocity |
| $\Lambda_n$ | eigenvalue of the Sturm Louville problem |
| $\phi_n$ | eigenfunction of the Sturm Louville problem |
| $e$ | eccentricity |
| $c$ | nominal clearance between bearing and shaft |
| $\theta$ | film position |

| | |
|---|---|
| $L$ | journal exial length |
| $D$ | bearing diameter |
| $R$ | radius of bearing |
| $\omega$ | shaft rotating speed |
| $\epsilon$ | ratio of eccentricity |

## A.2 Chapter 3

| | |
|---|---|
| $U_i$ | reciprocating speed of piston |
| $W_i$ | linear rotating speed |
| $h$ | film thickness |
| $p$ | hydrodynamic pressure |
| $x$ | piston motion direction |
| $z$ | circumferential direction |
| $p_T$ | trailing edge pressure |
| $p_{in}$ | inlet pressure |
| $p_L$ | leading edge pressure |
| $f$ | friction force |
| $\eta_0$ | atmospheric viscosity |
| $\alpha$ | pressure viscosity coefficient |
| $\eta$ | viscosity coefficient |
| $\rho_0$ | atmospheric density |
| $z_p$ | pressure viscosity index |
| $p_{gas}$ | gas pressure |
| $E$ | Young's modulus |
| $h_T$ | local film thickness |
| $\Delta$ | combined roughness of ring and liner |
| $\Delta_1$ | ring surface roughness amplitude |

| | |
|---|---|
| $\Delta_2$ | liner surface roughness amplitude |
| $\overline{h_T}$ | average gap |
| $\phi_c$ | contact factor |
| $P_a$ | average contact pressure |
| $\beta$ | curvature of asperity of radius |
| $\sigma$ | composite surface roughness |
| $\nu_i$ | Poisson's ratio |
| $F_h$ | hydrodynamic component of friction force |
| $\phi_{f_i}$ | shear flow factor |
| $F_a$ | asperity component of friction force |
| $W_a$ | total asperity contact load |
| $\mu_f$ | friction coefficient |
| $F_f$ | total friction force |
| $\bar{F_f}$ | normalized friction force |
| $\omega$ | rotational speed |
| $S$ | piston stroke |
| $L$ | connecting rod length |
| $\theta$ | crank angle |
| $h_{min}$ | minimum film thickness |
| $\gamma$ | surface pattern parameter |

## A.3 Chapter 4

| | |
|---|---|
| $p_i$ | pressure |
| $V_i$ | volume |
| $T_i$ | temperature |
| $m_{ij}$ | gas mass flow rate from region $i$ to region $j$ |

| | |
|---|---|
| $C_d$ | discharge coefficient |
| $A_g$ | effective gap area |
| $\gamma$ | Poisson constant |
| $C_f$ | frictional loss coefficient |
| $A_n$ | area normal to the flow |
| $F_p$ | gas pressure force |
| $F_f$ | friction force between piston ring and cylinder liner |
| $F_g$ | gravitational force |
| $F_s$ | supporting force between groove flank and upper/lower ring surface |
| $p_U$ | gas pressure on the upper ring surface |
| $p_L$ | gas pressure on the lower ring surface |
| $p_B$ | gas pressure behind the ring |
| $\delta U, \delta L$ | switch function |
| $h$ | ring side-clearance |
| $L_r$ | ring length along the circumferential direction |
| $W_r$ | ring width in the radial direction |
| $\mu_{oil}$ | oil viscosity |
| $D_r$ | outside diameter of ring |
| $T_r$ | ring axial thickness |
| $p_E$ | ring tension pressure |
| $x_r$ | ring motion along the piston reciprocating direction $x$ |
| $x_p$ | piston displacement |
| $F_i$ | inertial force term |
| $h_r$ | piston ring relative motion |

## A.4 Chapter 5

| | |
|---|---|
| $R$ | cylinder radius |

| | |
|---|---|
| $U$ | piston reciprocating speed |
| $e_b$ | eccentricity of piston bottom |
| $e_t$ | eccentricity of piston top |
| $C$ | clearance between piston and liner |
| $L$ | length of piston skirt |
| $p$ | hydrodynamic pressure |
| $F_{gas}$ | combustion gas load acting on piston head |
| $F_h$ | hydrodynamic pressure load |
| $F_f$ | viscous friction force |
| $F_{c_i}$ | internal force for piston along the $i$-axis |
| $F_{p_i}$ | internal force for wrist pin along the $i$-axis |
| $F_{rod}$ | connecting rod force acting on the pin location |
| $M_f$ | moment from viscous friction |
| $M_h$ | moment |
| $m_{piston}$ | piston mass |
| $I_{piston}$ | piston moment of inertial |
| $m_{pin}$ | wrist pin mass |

## A.5 Chapter 6

| | |
|---|---|
| $h$ | film thickness |
| $c$ | ring crown height |
| $B$ | ring axial height |
| $\mu_f$ | lubricated contact friction coefficient |
| $\mu_0$ | boundary friction coefficient |
| $U$ | piston reciprocating speed |
| $\omega$ | liner rotating speed |
| $R$ | bore radius |

## A.6 Chapter 7

| | |
|---|---|
| $v$ | wear rate, wear volume |
| $k$ | non-dimensional wear coefficient |
| $L$ | normal load |
| $S$ | sliding distance |
| $H$ | hardness of liner |
| $\delta$ | wear depth |
| $p$ | contact pressure |
| $A$ | area worn of apparent contact |
| $B$ | ring axial thickness |
| $N$ | engine speed |
| $K_b$ | liner wear constant |
| $h_{min}$ | minimum film thickness |
| $\sigma$ | ring-liner composite surface roughness |

# Appendix B

# Computer Code for Generalized Reynolds Equation

```
clear all
close all

% define bearing geometry

B=1;    % bearing length
L=1;    % bearing width

m=80;  % grid num
n=80;  % grid num

xx=0:B/m:B;
zz=-L/2:L/n:L/2;

del_x=B/m;
del_z=L/n;

% initial pressure value for inner points

for i=2:m
   for j=2:n
      p(i,j)=0.0;
   end
end

% initial bc pressure

% vertical

for j=1:n+1
   p(1,j)=0;
   p(m+1,j)=0;
end

% horizontal
```

```
for i=1:m+1
   p(i,1)=0.0;
   p(i,n+1)=0.0;
end

% define x,z of h(x,z)

for i=2:m
   for j=2:n
      x_b(i,j)= (i-1.5)*del_x;
      x_f(i,j)= (i-0.5)*del_x;
      x(i,j) = (i-1)*del_x;

      z_b(i,j)= (j-1.5)*del_z;
      z_f(i,j)= (j-0.5)*del_z;
      z(i,j) = (j-1)*del_z;
   end
end

% calculate del(i,j),a0(i,j),a1(i,j),a2(i,j),a3(i,j),a4(i,j)

u=1;
v=0.005;
mu=1;  % lubricant viscosity

% function hxz depends on bearing types

for i=2:m
   for j=2:n
      del_1(i,j)=((hxz(x_f(i,j),z(i,j)))^3 + (hxz(x_b(i,j),z(i,j)))^3)/(del_x^2);
      del_2(i,j)=((hxz(x(i,j),z_f(i,j)))^3 + (hxz(x(i,j),z_b(i,j)))^3)/(del_z^2);
      del(i,j)=del_1(i,j) + del_2(i,j);
      a0(i,j)=mu*(-6*u*(hxz(x_f(i,j),z(i,j))-hxz(x_b(i,j),z(i,j)))/del_x + 12*v)/del(i,j);
      a1(i,j)=(hxz(x_f(i,j),z(i,j)))^3/(del_x^2)/del(i,j);
      a2(i,j)=(hxz(x_b(i,j),z(i,j)))^3/(del_x^2)/del(i,j);
```

```
      a3(i,j)=(hxz(x(i,j),z_f(i,j)))^3/(del_z^2)/del(i,j);
      a4(i,j)=(hxz(x(i,j),z_b(i,j)))^3/(del_z^2)/del(i,j);
    end
end

mytol=4e-5;
q=zeros(m+1,n+1);

% Gauss-Seidel Iteration

for k=1:5000
   q = p;
   for i=2:m
      for j=2:n
        p(i,j)=a0(i,j)+a1(i,j)*p(i+1,j)+a2(i,j)*p(i-1,j)+a3(i,j)*p(i,j+1)+a4(i,j)*p(i,j-1);
      end
   end
   p = p+mytol/1e8;
   err = sum(sum(abs(q-p)))/sum(sum(abs(p)));
   p = p-mytol/1e8;

   if(err < mytol)
      k
      surf(xx,zz,p');
      xlabel('x - bearing length direction')
      ylabel('z - bearing width direction')
      zlabel('Hydrodynamic Pressure(Pa)')
      title('Numerical Solution, L/B = 1.0')
      break;
   end;

end

max(max(p));
min(min(p));
```

```
% total load

f_load=0;
for j=2:n
  for i=2:m
       f_load=f_load+p(i,j)*del_x*del_z;
  end
 end

% output plots

 figure;
 plot(zz',p(m/2+1,:))
 xlabel('z - bearing width direction ')
 ylabel('Hydrodynamic Pressure (Pa)')

 hold on

 plot(zz', p(m/8+1,:))

 hold on

 plot(zz', p(m/4+1,:))

 hold on

 plot(zz', p(3*m/8+1,:))

 figure;

 plot(xx',p(:,n/2+1))
 xlabel('x - bearing length direction ')
 ylabel('Hydrodynamic Pressure (Pa)')
```

```
 hold on
 plot(xx',p(:,n/8+1))

 hold on
 plot(xx',p(:,n/4+1))

 hold on
 plot(xx',p(:,3*n/8+1))

function hxz=hxz(x,z);

h1=1.2e-3;
h0=1e-3;
BB=1;
hxz=h0+(h1-h0)*(1-x/BB);  % incline pad bearing
```

# Appendix C

# Corrective Flow Factors

## C.1 Patir and Cheng's Flow Factor

Pressure flow factor developed by Patir and Cheng [28] [51] can be written in the following empirical form.

$$\phi_x = \begin{cases} 1 - Ce^{-rH_\sigma} & \gamma \leq 1 \\ 1 + Ce^{-r} & \gamma > 1 \end{cases} \tag{C.1}$$

where $H_\sigma = h/\sigma$ is a non-dimensional film thickness, $\gamma$ is a surface pattern parameter. The constants $C$ and $r$ are given in Table C.1 for various surface roughness orientations.

Shear flow factor $\phi_s$ term represents the additional flow transport due to sliding in a rough bearing. The fluid in the valleys of the moving rough surface increase the fluid transport between the surfaces. If surfaces have identical roughness configuration, there will be no additional flow transport. The shear flow factor has been obtained by numerical flow simulations by Patir and Cheng [51]. The shear

| $\gamma$ | $C$ | $r$ | Range |
|---|---|---|---|
| 1/9 | 1.480 | 0.42 | $H_\sigma > 1$ |
| 1/6 | 1.380 | 0.42 | $H_\sigma > 1$ |
| 1/3 | 1.180 | 0.42 | $H_\sigma > .75$ |
| 1 | 0.900 | 0.56 | $H_\sigma > .5$ |
| 3 | 0.225 | 1.50 | $H_\sigma > .5$ |
| 6 | 0.520 | 1.50 | $H_\sigma > .5$ |
| 9 | 0.870 | 1.50 | $H_\sigma > .5$ |

Table C.1: Coefficients for pressure flow factor

| $\gamma$ | $A_1$ | $\alpha_1$ | $\alpha_2$ | $\alpha_3$ | $A_2$ |
|---|---|---|---|---|---|
| 1/9 | 2.046 | 1.12 | 0.78 | 0.03 | 1.856 |
| 1/6 | 1.962 | 1.08 | 0.77 | 0.03 | 1.754 |
| 1/3 | 1.858 | 1.01 | 0.76 | 0.03 | 1.561 |
| 1 | 1.899 | 0.98 | 0.92 | 0.05 | 1.126 |
| 3 | 1.560 | 0.85 | 1.13 | 0.08 | 0.556 |
| 6 | 1.290 | 0.62 | 1.09 | 0.08 | 0.388 |
| 9 | 1.011 | 0.54 | 1.07 | 0.08 | 0.295 |

Table C.2: Coefficients for shear flow factor

flow factor for a single rough surface is presented in the following empirical form

$$\Phi_s = \begin{cases} A_1 H_\sigma e^{-\alpha_2 H_\sigma + \alpha_3 {H_\sigma}^2} & H_\sigma \le 5 \\ A_2 e^{-0.25 H_\sigma} & H_\sigma > 5 \end{cases} \tag{C.2}$$

where $H_\sigma = h/\sigma$. The coefficients are shown in Table C.2.

For a combined effect of two mating surfaces, the shear flow factor $\phi_s$ is written as

$$\phi_s = (\frac{\sigma_1}{\sigma})^2 \Phi_s(\frac{h}{\sigma}, \gamma_1) - (\frac{\sigma_2}{\sigma})^2 \Phi_s(\frac{h}{\sigma}, \gamma_2) \tag{C.3}$$

where $\sigma_1$ and $\sigma_2$ are standard derivation of surface roughness, $\gamma_1$ and $\gamma_2$ repesent the surface roughness pattern.

The $\phi_f$ parameter represents the sliding velocity component of the shear stress. This parameter is defined as:

$$\phi_f = hE\left(\frac{1}{h_T}\right) \tag{C.4}$$

where $E$ is expectation (averaging) operator. Newton's law gives infinite shear stress as the film thickness approaches to zero. In order to eliminate this difficulty a small film thickness $\varepsilon$ is defined and boundary friction is assumed when the film thickness is below this level. Using this assumption $\phi_f$ can be written as:

$$\phi_f = h\int_{-h+\varepsilon}^{\infty} \frac{f(\delta)}{(h+\delta)} d\delta \tag{C.5}$$

In calculations, $\varepsilon$ was arbitrarily set equal to $\sigma/100$. A polynomial density function which closely approximates the Gaussian function is used:

$$\begin{bmatrix} \frac{35}{96\sigma}\left[1-\left(\frac{\delta}{3\delta}\right)\right] & |\delta| \leq 3\sigma \\ 0 & |\delta| > 3\sigma \end{bmatrix} \tag{C.6}$$

Similarly, another set of shear stress factors $\phi_{fp}$ and $phi_{fs}$ are defined such that the mean hydrodynamic shear stress is given in terms of mean quantities.

Shear stress factor $\phi_{fp}$ can be written in the following empirical form

$$\phi_{fp} = 1 - De^{-sH} \tag{C.7}$$

The constants $D$ and $s$ are given in Table C.3 for various surface roughness orientations.

Another shear stress factor $\phi_{fs}$ can be written in the following empirical form

$$\phi_{fs} = A_3 {H_\sigma}^{\alpha_4} e^{-\alpha_5 H_\sigma + \alpha_6 {H_\sigma}^2} \tag{C.8}$$

| $\gamma$ | $D$ | $s$ | Range |
|---|---|---|---|
| 1/9 | 1.51 | 0.52 | $H_\sigma > 1$ |
| 1/6 | 1.51 | 0.54 | $H_\sigma > 1$ |
| 1/3 | 1.47 | 0.58 | $H_\sigma > 1$ |
| 1 | 1.40 | 0.66 | $H_\sigma > .75$ |
| 3 | 0.98 | 0.79 | $H_\sigma > .5$ |
| 6 | 0.97 | 0.91 | $H_\sigma > .5$ |
| 9 | 0.73 | 0.91 | $H_\sigma > .5$ |

Table C.3: Coefficients for shear flow factor

| $\gamma$ | $A_3$ | $\alpha_4$ | $\alpha_5$ | $\alpha_6$ |
|---|---|---|---|---|
| 1/9 | 14.1 | 2.45 | 2.30 | 0.10 |
| 1/6 | 13.4 | 2.42 | 2.30 | 0.10 |
| 1/3 | 12.3 | 2.32 | 2.30 | 0.10 |
| 1 | 11.1 | 2.31 | 2.38 | 0.11 |
| 3 | 9.80 | 2.25 | 2.80 | 0.18 |
| 6 | 10.1 | 2.25 | 2.97 | 0.18 |
| 9 | 8.70 | 2.15 | 2.97 | 0.18 |

Table C.4: Coefficients for shear stress factor

The coefficients are shown in Table C.4 for different surface roughness orientations.

## C.2 Peeken and Knoll's Flow Factor

Peeken and Knoll's flow factor includes contact effects under low $h/\sigma$ region. The shear flow factor and shear stress factor show early contact when $h/\sigma$ is less than 3. Assume that the difference between Patir and Cheng's flow factors are small compared to Peeken and Knoll's factor for the region of $h/\sigma > 3$. For $0 < h/\sigma < 3$, a linear relationship describes the flow factor. The shear flow factor starts from zero at $h/\sigma = 0$ and gradually increases to Patir and Cheng's value.

# Appendix D

# Gas Flow Models

## D.1 Orifice Flow Model

The gas passing through the ring gap is treated the orifice flow as shown in Figure D.1.

From gas energy equation,

$$\frac{P_1}{\rho_1} + \frac{v_1^2}{2} + U_1 = \frac{P_2}{\rho_2} + \frac{v_2^2}{2} + U_2 \tag{D.1}$$

and by the definition of enthalpy

$$h = \frac{P}{\rho} + U = c_p T. \tag{D.2}$$

Notice that $v_1 = 0$, the downstream velocity $v_2$ is calculated by

$$v_2 = [2c_p(T_2 - T_1)]^{0.5}. \tag{D.3}$$

The gas constant $c_p = \frac{\gamma}{\gamma - 1} R$, and $v_2$ can be written as

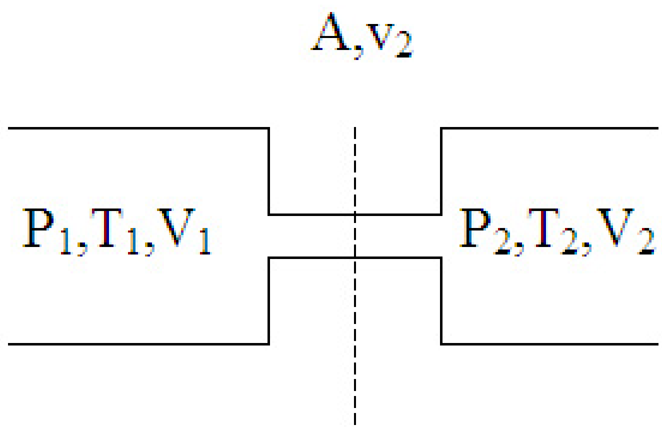


Figure D.1: Schematic of gas flow through Orifice

$$v_2 = [\frac{2\gamma}{\gamma - 1} R T_1 (1 - \frac{T_2}{T_1})]^{0.5} \tag{D.4}$$

Assume that the flow is isentropic, $\frac{P}{\rho^\gamma}$ is constant

$$P_2 = \frac{T_2}{T_1} P_1 (\frac{P_2}{P_1})^{\frac{1}{\gamma}} \tag{D.5}$$

and $v_2$ is written in terms of pressure and temperature

$$v_2 = [\frac{2\gamma}{\gamma - 1} R T_1 (1 - (\frac{P_2}{P_1})^{\frac{\gamma-1}{\gamma}})]^{0.5} \tag{D.6}$$

Finally, the mass flow rate $\frac{dm}{dt} = c_d \rho_2 A v_2$, here $c_d$ is the discharge coefficient, $\rho_2$ is gas density and can be written as $\rho_2 = \frac{P_2}{RT_2}$, A is the ring end-gap area, $v_2$ is expressed in equation (D.6).

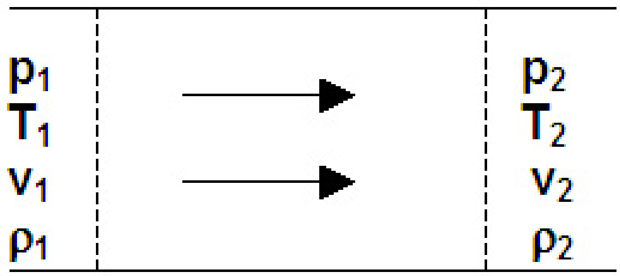


Figure D.2: Schematic of gas flow through a narrow channel

## D.2 Rayleigh Flow Model

Flow through the side clearance between ring and grove is treated as a constant-area quasi-Rayleigh compressible flow. Gas passes through a control volume as shown in Figure D.2.

Mass flow rate $\frac{dm}{dt} = A\rho\nu$ is equal for upstream and downstream. The continuity equation can be written as

$$\rho_1\nu_1 = \rho_2\nu_2 \tag{D.7}$$

From ideal gas law, $\rho = \frac{p}{RT}$ and flow velocities has the following relationship

$$\nu_1 = \frac{p_2}{p_1}\frac{T_1}{T_2}\nu_2 \tag{D.8}$$

From momentum equation of compressible flow,

$$p_1 - p_2 = \rho_2{\nu_2}^2 - \rho_1{\nu_1}^2 = \frac{p_2}{RT_2}{\nu_2}^2 - \frac{p_1}{RT_1}{\nu_1}^2 \tag{D.9}$$

Substitute equation D.8 into equation D.9 to eliminate $\nu_1$

$$\nu_2 = \left[ \frac{p_1 - p_2}{\frac{p_2}{RT_2}\left(1 - \frac{p_2 T_1}{p_1 T_2}\right)} \right]^{1/2} \tag{D.10}$$

and mass flow rate is then written as

$$\frac{dm}{dt} = A_n \left[ \frac{p_1 - p_2}{\frac{p_2}{RT_2}\left(1 - \frac{p_2 T_1}{p_1 T_2}\right)} \right]^{1/2}. \tag{D.11}$$

# Bibliography


[1] Economou, P., Dowson, D., , and Baker, A., 1979. "Piston ring lubrication - part i. the historical development of piston ring technology". *Energy Conservation Through Fluid Film Lubrication Technology: Frontier in Research and Design,ASME Winter Annual Meeting* , pp. 1–22.

[2] Dowson, D., Economou, P., Ruddy, B., Strachan, P., and Baker, A., 1979. "Piston ring lubrication - part ii. theoretical analysis of a single ring and a complete ring pack". *Energy Conservation Through Fluid Film Lubrication Technology: Frontier in Research and Design,ASME Winter Annual Meeting* , pp. 23–52.

[3] Taylor, C., 1993. *Engine Tribology.* Elsevier Science Publishers, B.V.J.

[4] Hersey, M., 1966. *Theory and Research in Lubrication.* John Wiley & Sons, Inc.

[5] Jeng, Y., 1992. "Theoretical analysis of piston-ring lubrication part i-fully flooded lubrication". *STLE, Trib. Trans.,* **35(4)** , pp. 696–706.

[6] Priest, M., Dowson, D., and Taylor, C., 1999. "Predictive wear modelling of lubricated piston ring in a diesel engine". *Wear,* **231** , pp. 89–101.

[7] Castleman, R., 1936. "A hydrodynamic theory of piston ring lubrication". *Physics,* **7** , pp. 364–367.

[8] Eilon, S., and Sauders, M., 1957. "A study of piston ring lubrication". *Pro. Inst. Mech. Engrs.,* **171(11)** , pp. 427–443.

[9] Furuhama, S., 1959. "A dynamic theory of piston ring lubrication, 1st report - calculation". *Bull. of JSME,* **2** , pp. 423–428.

[10] Furuhama, S., 1960. "A dynamic theory of piston ring lubrication, 2nd report - experiment". *Bull. of JSME,* **3** , pp. 291–297.

[11] Furuhama, S., and Sumi, T., 1961. "A dynamic theory of piston ring lubrication, 3rd report - measurement of oil film thickness". *Bull. of JSME,* **4** , pp. 744–752.

[12] Lloyd, T., 1968. "The hydrodynamic lubrication of piston ring". *Pro. Inst. Mech. Engrs.,* **183(3B)** , pp. 28–34.

[13] Ting, L., and Mayer, J., 1974. "Piston ring lubrication amd cylinder core wear analysis,part 1-theory". *ASME J. Lubr. Technol.,* **96** , pp. 305–314.

[14] Ting, L., and Mayer, J., 1974. "Piston ring lubrication amd cylinder core wear analysis,part 1-theory verification". *ASME J. Lubr. Technol.,* **96** , pp. 258–266.

[15] Hamilton, G., and Moore, S., 1964. "Comparison between measured and calculated thickness of the oil film lubricating piston rings". *Proc. Inst. Mech. Engrs.,* **188** , pp. 262–268.

[16] Brown, S., and Hamilton, G., 1977. "The partially lubricated piston ring". *Journ. Mech. Engrg. Sci.,* **19(2)** , pp. 81–89.

[17] Moore, S., and Hamilton, G., 1978. "The starved lubrication of piston rings in a diesel engine". *Journ. Mech. Engrg. Sci.,* **20(6)** , pp. 345–352.

[18] Ruddy, B., Dowson, D., Economou, P., and Baker, A., 1978. "Piston ring lubrication - part iii. the influence of ring dynamics and ring twist". *Energy Conservation Through Fluid Film Lubrication Technology: Frontier in Research and Design,ASME Winter Annual Meeting* , pp. 191–215.

[19] Miltsios, G., Patterson, D., and Papanastsiou, T., 1989. "Solution of the lubrication problem and calculation of the friction force on the piston rings". *ASME J. Tribol.,* **111** , pp. 635–641.

[20] Wu, G., and Chen, Z., 1992. "The numerical study of piston ring elastohydrodynamic lubrication by the multigrid method". *STLE. Trib. Trans.,* **35(1)** , pp. 135–141.

[21] Jeng, Y., 1992. "Theoretical analysis of piston-ring lubrication part ii-starved lubrication and its application to a complete ring pack". *STLE, Trib. Trans.,* **35(4)** , pp. 707–714.

[22] Ma, M., Smith, E., and Sherrington, I., 1995. "A three-dimensional analysis of piston ring lubrication. part 1: Modelling". *Proc. Instn Mech Engrgs,* **211(J)** , pp. 1–14.

[23] Li, D., Rohde, S., and Ezzat, H., 1983. "An automotive piston lubriation model". *ASLE, Transactions.,* **26(2)** , pp. 151–160.

[24] Dowson, D., Ruddy, B., and Economou, P., 1983. "The elastohydrodynamic lubrication of piston rings". *Proc. R. Soc. Lond.,* **A 386** , pp. 409–430.

[25] Engineering, Ring, R. S. P., and Department, S., 1975. *Engineer's Handbook of Piston Rings, Seal Rings, Mechanical Shaft Seals.* Koppers Company, Inc., Koppers Company, Inc. Metal Product Division, Baltimore, Maryland 21203.

[26] Hwu, C., and Weng, C., 1991. "Elastohydrodynamic lubrication of piston rings". *Wear,* **151** , pp. 203–215.

[27] Oh, K., Li, C., and Goenka, P., 1987. "Elastohydrodynamic lubrication of piston skirts". *ASME J. of Tribology,* **109** , pp. 356–362.

[28] Patir, N., and Cheng, H., 1978. "An average flow model for determining effects of three-dimensional roughness on partial hydrodynamic lubrication". *Trans. ASME J. Vib. Acoust.,* **100** , pp. 12–17.

[29] Rohde, S., 1980. "A mixed friction model for dynamically loaded contacts with application to piston ring lubrication". *Surface Roughness Effects in Hydrodynamic and Mixed Lubrication,ASME,New York* , pp. 19–51.

[30] Hu, Y., Cheng, H., Arai, T., Kobayahsi, Y., and Aoyama, S., 1994. "Numerical simulation of piston ring in mixed lubrication-a non-axisymmetrical analysis". *ASME, J. Tribol.,* **116** , pp. 470–478.

[31] Greenwood, J., and Tripp, J., 1971. "The contact of two nominally flat rough surfaces". *Pro. Inst. Mech. Engrs.,* **185** , pp. 625–633.

[32] Michail, S., and Barber, G., 1995. "The effects of roughness on piston ring lubrication - part i: Model development". *Triboloy Transactions,* **38** , pp. 19–26.

[33] Michail, S., and Barber, G., 1995. "The effects of roughness on piston ring lubrication - part ii: The relationship between cylinder wall surface topograph and oil film thickness". *Triboloy Transactions,* **38** , pp. 173–177.

[34] Knopf, M., Eiglmeier, C., and Merker, G., 1998. "Calculation of unsteady hydrodynamic lubrication and surface contact at the piston-ring/cylinder-liner interface". *SAE Paper 981402* .

[35] Zhu, D., Cheng, H., Arai, T., and Hamai, K., 1992. "A numerical analysis for piston skirts in mixed lubrication - part i: Basic modeling". *ASME, J. Tribol.,* **114** , pp. 553–562.

[36] Zhu, D., Hu, Y., Cheng, H., Arai, T., and Hamai, K., 1993. "A numerical analysis for piston skirts in mixed lubrication - part ii: Deformation considerations". *ASME, J. Tribol.,* **115** , pp. 125–133.

[37] Gangopadhyay, A., 2000. "Development of a piston ring-cylinder bore wear model". *SAE Paper 2000-01-1788* .

[38] Tung, S., and Huang, Y., 2004. "Modeling of abrasive wear in a piston ring and engine cylinder bore system". *STLE, Trib. Trans.,* **47** , pp. 17–22.

[39] Akalin, O., and Newaz, G., 2001. "Piston ring-cylinder bore friction modeling in mixed lubrication regime: Part i - analytical results". *ASME J. of Tribology,* **123** , pp. 211–218.

[40] Frene, J., and Nicolas, D., 1997. *Hydrodynamic Lubrication Bearings and Thrust Bearings*. Elsevier.

[41] Bowden, F., and Tabor, D., 1967. *Friction and Lubrication*. Methuen & Co, Ltd.

[42] Cameron, A., 1976. *Basic Lubrication Theory*. John Wiley & Sons, Inc.

[43] Venner, C., and Lubrecht, A., 2000. *Multilevel Methods in Lubrication*. Elsevier Science B.V., P.O.Box 211, 1000 AE Amsterdam, The Netherlands.

[44] Dowson, D., 1979. *History of Tribology*. Longman Group Limited, London.

[45] Yang, Q., and T. G. Keith, J., 1995. "An elastohydrodynamic caviatation algorithm for piston ring lubrication". *STLE Tribology Transactions,* **38** , pp. 97–107.

[46] Yang, Q., and T. G. Keith, J., 1996. "Two-dimensional piston ring lubrication - part ii: Elastic ring consideration". *STLE Tribology Transactions,* **39** , pp. 870–880.

[47] Hamrock, B., Schmid, S., and Jacobson, B., 2004. *Fundamentals of Fluid Film Lubrication*. Marcel Dekker, Inc, New York.

[48] Tzeng, S., and Saibel, E., 1967. "Surface roughness effect on slider bearing lubrication". *ASLE Trans.,* **10** , p. 334.

[49] Christensen, H., and Tonder, K., 1971. "The hydrodynamic lubrication rough bearing surfaces on finite width". *Journal of Lubrication Technology, Trans. ASME Series F,* **93** , p. 324.

[50] Christensen, H., and Tonder, K., 1973. "The hydrodynamic lubrication rough journal bearings". *Journal of Lubrication Technology, Trans. ASME Series F,* **95** , p. 166.

[51] Patir, N., and Cheng, H., 1979. "Application of average flow model to lubrication between rough sliding surfaces". *Trans. ASME J. Vib. Acoust.,* **101** , pp. 220–230.

[52] Majumdar, B., and Hamrock, B., 1981. "Effect of surface roughness on hydrodynamic bearings". *NASA Technical Memorandum,* **81711** , pp. 1–22.

[53] Tripp, J., 1983. "Surface roughness effects in hydrodynamic lubrication: The flow factor method". *ASME J. Lubrication Technology,* **105** , pp. 458–465.

[54] Tonder, K., 1986. "The lubrication of unidirectional striated roughness: Consequences for some general roughness theories". *ASME J. Tribology,* **108** , pp. 167–170.

[55] Peeken, H., and Knoll, G., 1997. "On the numerical determination of flow factors". *ASME J. Tribology,* **119** , pp. 259–264.

[56] Hu, Y., Cheng, H., Kobayashi, Y., and Aoyama, S., 1994. "Numerical sim-

ulation of piston ring in mixed lubrication - a non-axisymmetrical analysis". *ASME J. Tribology,* **116** , pp. 470–478.

[57] Steenwyk, B., N.W.Bolander, and Sadeghi, F., 2004. "Purdue piston ring reciprocating liner summary". *Technical Report* .

[58] Xu, H., Bryant, M., Matthews, R., Kiehne, T., Steenwyk, B., N.W.Bolander, and Sadeghi, F., 2004. "Friction prediction for piston ring-cyliner liner lubrication". *Proceedings of ASME ICE Fall Technique Conference* .

[59] Wu, C., and Zhang, L., 1989. "An average reynolds equation for partial film lubrication with contact factor". *ASME J. of Tribology,* **111** , pp. 188–191.

[60] Matthews, R. D., 2004. *Internal Combustion Engines and Automotive Engineering.* Harper-Collis.

[61] Richardson, D., 2000. "Review of power cylinder friction for diesel engines". *Journal of Engineering for Gas Turbines and Power,* **122** , pp. 506–519.

[62] Jiang, X., Hua, D., Cheng, H., Ai, X., and Lee, S., 1999. "A mixed elastohydrodynamic lubrication model with asperity contact". *ASME J. of Tribology,* **121** , pp. 481–491.

[63] Peklenik, J., 1967. "New developments in surface characterization and measurement by means of random process analysis". *Proc. Insts. Mech. Engr.,* **182,Part 3K** , pp. 108–126.

[64] Bhushan, B., and Tonder, K., 1989. "Roughness-induced shear and squeeze-film effects in magnetic recording". *ASME J. of Tribology,* **111** , pp. 220–227.

[65] Lo, S., 1992. "On the effects of roughness orientation - a mapping and double scale analysis of flow factors". *ASME J. of Tribology,* **114** , pp. 747–754.

[66] Tateishi, Y., 1994. "Tribological issues in reducing piston ring friction losses". *Tribology International* , pp. 17–23.

[67] Namazian, M., and Heywood, J., 1982. "Flow in the piston-cylinder-ring crevices of a spark-ignition engine: Effect on hydrocarbon emissions, efficiency and power". *SAE Paper 820088* .

[68] Kuo, T., Sellnau, M., Theobald, M., and Jones, J., 1989. "Calculation of flow in the piston-cylinder-ring crevices of a homogeneous-charge engine and comparison with experiment". *SAE Paper 890838* .

[69] Kim, C., Bae, C., and Choi, S., 2000. "Importance of inter-ring crevice volume as a source of unburned hydrocarbon emission - numerical considerations". *Proc. Instn. Mech. Engrs.,* **214** , pp. 395–403.

[70] Keribar, R., Dursunkaya, Z., and Flemming, M., 1991. "An integrated model of ring pack performance". *ASME J. of Engineering for Gas Turbines and Power,* **113** , pp. 382–389.

[71] Roberts, C., and Matthews, R., 1996. "Development and applicaton of an improved ring pack model for hydrocarbon emission studies". *SAE Paper 961966* .

[72] Dursunkaya, Z., Keribar, R., and Richardson, D., 1992. "Experimental and numerical investigation of inter-ring gas pressure and blowby in a diesel engine". *SAE Paper 930792* .

[73] Tian, T., Noordzij, L., Wong, V., and Heywood, J., 1996. "Modeling piston-ring dynamics, blowby, and ring-twist effects". *Proceedings of ASME ICE Fall Technique Conference,* **2** , pp. 67–80.

[74] Xu, H., Kim, M., Dardalis, D., Bryant, M., Matthews, R., and Kiehne, T.,

2005. "Numerical and experimental investigation of piston ring friction". *Proceedings of ASME ICE Spring Technique Conference* .

[75] Furuhama, S., and Hiruma, M., 1972. "Axial movement of piston ring in the groove". *ASLE Transaction,* **15** , pp. 278–287.

[76] Richardson, D., 1996. "Comparison of measured and theoretical inter-gas pressure on a diesel engine". *SAE Paper 961909* .

[77] Furuhama, S., Hiruma, M., and Tsuzita, M., 1979. "Piston ring motion and it influence on engine tribology". *SAE Paper 790860* .

[78] Okabo, M., Kanda, H., and Yonegawa, T., 1989. "Analysis and reduction of piston slap noise in disel engines". *SAE Paper 890127* .

[79] Ricardo, H., 1944. *The High-speed Internal-combustion Engine.* Interscience Publishers, New York.

[80] Setright, L., 1975. *Some Unusal Engines.* Mechanical Engineering Publications for the Institution of Mechanical Engineers, London.

[81] Kim, M., Dardalis, D., Matthews, R., and Kiehne, T., 2005. "Engine friction reduction through liner rotation". *Technical Report* .

[82] Lebeck, A., 1987. "Parallel sliding load support in the mixed friction regimes, part 1 - the experimental data". *ASME J. of Tribology,* **109** , pp. 189–195.

[83] Lebeck, A., 1987. "Parallel sliding load support in the mixed friction regimes, part 2 - evaluation of the mechanism". *ASME J. of Tribology,* **109** , pp. 196–205.

[84] Fogg, A., 1946. "Fluid film lubrication of parallel thrust surfacces". *Pro. Inst. Mech. Engrs.,* **155** , pp. 49–53.

[85] Osterle, F., Charnes, A., and Saibel, E., 1953. "On the solution of the reynolds equation for slider-bearing lubrication - vi". *Transactions of ASME* , pp. 1133–1136.

[86] Cameron, A., and Wood, W., 1958. "Parallel surface thrust bearing". *ASLE Transactions,* **1** , pp. 254–258.

[87] Dowson, D., and Hudson, J., 1963. "Thermo-hydrodynamic analysis of the infinite slider-bearing: Par ii". *Proc. Inst. Mech. Engrs.* , pp. 45–51.

[88] Cameron, A., 1958. "The viscosity wedge". *ASLE Transactions,* **1** , pp. 248–253.

[89] Ettles, C., and Cameron, A., 1966. "The action of the parallel surface thrust bearing". *Pro. Inst. Mech. Engrs.,* **180** , pp. 61–75.

[90] Lewichi, W., 1955. "Theory of hydrodynamic lubrication in parallel sliding". *The Engineering,* **200** , pp. 939–941.

[91] Oh, K., 1986. "The formulation of the mixed lubrication problem as a generalized nonlinear complementarity problem". *ASME J. of Tribology,* **108** , pp. 598–604.

[92] Heshmat, H., Pinkus, O., and Godet, M., 1989. "On a common tribological mehcanism between interacting surfaces". *ASME, Tribology Transactions,* **32(1)** , pp. 32–41.

[93] Cheng, H., 2002. "Analytical modeling of mixed lubrication performance". *Boundary and Mixed Lubrication: Science and Application* , pp. 19–33.

[94] Spikes, H., and Olver, A., 2002. "Mixed lubrication - experiment and theory". *Boundary and Mixed Lubrication: Science and Application* , pp. 95–113.

[95] Hess, D., and Soom, A., 1993. "The effects of relative angular motions on friction at rough planar contacts". *ASME J. of Tribology,* **115** , pp. 96–101.

[96] Hess, D., and Soom, A., 1992. "Normal and angular motions at rough planar contacts during sliding with friction". *ASME J. of Tribology,* **114** , pp. 567–578.

[97] Beek, A. V., 2004. *Machine lifetime performance and reliablity.* www.tribology-abc.com, TU Delft.

[98] Xu, H., , Bryant, M., Matthews, R., Kim, M., and Kiehne, T., 2005. "Theoretical analysis of piston ring frictional loss in an innovative rotating liner internal combustion engine". *World Tribology Congress III* .

[99] Becker, E., and Ludema, K., 1999. "A qualitative empirical model of cylinder bore wear". *Wear,* **225-229** , pp. 387–404.

[100] Nautiyal, P., Singhai, S., and Sharma, J., 1983. "Friction and wear process in piston rings". *Tribology International* , pp. 43–49.

[101] Priest, M., Dowson, D., and Taylor, C., 1999. "Predictive wear modelling of lubricated piston rings in a diesel". *Wear,* **231** , pp. 89–101.

[102] Sunden, H., and Schaub, R., 1979. "Piston rings for slow and medium speed diesel engines". *Tribology International* , pp. 3–14.

[103] Bhushan, B., 1999. *Principles and Applications of Tribology.* John Wiley and Sons, Inc.

[104] Handzel-Powierza, Z., Klimczak, T., and Polijaniuk, A., 1992. "On the experimental verification of the greenwood-williamson mode lfor the contact of rough surfaces". *Wear,* **154** , pp. 115–124.

[105] McCool, J., 1986. "Comparison of models for the contact of rough surfaces". *Wear,* **107** , pp. 37–60.

# Vita

Huijie Xu was born in Ningbo, China, on August 23, 1969, the second son of three children of Yongfa Xu and Shanshan Hu. He received the Bachelor's degree in power machinery engineering with the highest honor from Shanghai Jiao Tong University in 1991, and the Master's degree in engineering mechanics from The University of Texas in 2002. He has been a Ph.D. candidate in the department of mechanical engineering at The University of Texas since 2004. He is a member of Tau Beta Pi, and a student member of ASME, SAE, STLE, SIAM, and ASEE.

Permanent Address: 203E2 Simingshang Road, Beilun,
Ningbo, Zhejiang, P.R. China, 315800

This dissertation was typeset with LaTeX $2_\varepsilon$[1] by the author.

[1] LaTeX $2_\varepsilon$ is an extension of LaTeX. LaTeX is a collection of macros for TeX. TeX is a trademark of the American Mathematical Society. The macros used in formatting this dissertation were written by Dinesh Das, Department of Computer Sciences, The University of Texas at Austin, and extended by Bert Kay, James A. Bednar, and Ayman El-Khashab.